CORAL REEF ECOSYSTEM HEALTH IN RESPONSE TO CLIMATE CHANGE AND ENVIRONMENTAL STRESSORS

A Dissertation

by

ANDREA KIMIKO KEALOHA

Submitted to the Office of Graduate and Professional Studies of
Texas A&M University
in partial fulfillment of the requirements for the degree of

DOCTOR OF PHILOSOPHY

Chair of Committee,	Kathryn Shamberger
Committee Members,	Steven DiMarco
	Brendan Roark
	Niall Slowey
	Shari Yvon-Lewis
Head of Department,	Shari Yvon-Lewis

May 2019

Major Subject: Oceanography

ABSTRACT

Anthropogenic stressors such as ocean acidification, ocean warming and hypoxia threaten the health and persistence of coral reefs worldwide. In the following studies, we focused on two coral reefs: the Flower Garden Banks (FGB) in the Gulf of Mexico (GoM) and Kāneʻohe Bay barrier reef in Hawaiʻi. We characterized the natural spatiotemporal variability of the carbonate system within these reefs and their surrounding source water environments. We also investigated the relationship between various environmental parameters and reef-scale calcification in order to understand how climate-driven changes in these parameters will affect future coral reef health.

We first characterized surface water carbon dioxide (CO_2) variability in the GoM over multiple time scales (e.g., seasonal and decadal) in order to understand the source water characteristics to the FGB. Following a localized mortality event at the East Bank (EB) in the FGB, we collected biogeochemical data to uncover the mechanisms leading to the die-off. We measured low sea surface salinity and total alkalinity over the EB, which is indicative of river-derived water. At depth, high density, salinity, nutrients and microbial taxa associated with deep waters were coincident with low temperature and Ω_{ar}, indicating a deeper source water at the EB. Cross-slope density gradients were consistent with an upwelling circulation pattern. We hypothesize that the combination of these features led to the formation of hypoxia and mortality of benthic coral reef organisms on the EB.

In Kāneʻohe Bay, we calculated net ecosystem calcification (NEC; calcification-

dissolution) and oceanic POC uptake to test for a connection between these two parameters. While several studies have hypothesized that oceanic POC may be an important nutrient source providing energy for coral reef calcification, this is the first study to test the hypothesis in the natural environment. We observed a significant, positive correlation between NEC and oceanic POC uptake. These results reveal a potential role of oceanic POC in fueling NEC and suggests that offshore productivity could be a critical component to the resistance or susceptibility of coral reefs to climate change, and should be considered when predicting future coral reef health.

DEDICATION

This work is dedicated to the people of the Native Hawaiian culture, whose persistence and health is intimately connected to the health of our oceans. My steadfast quest for knowledge is drawn from my boundless love for you, and my dream is that one day, the oceans will thrive again, and so will we.

ACKNOWLEDGEMENTS

I would first like to thank my committee chair, Dr. Katie Shamberger, whose mentorship and guidance has transformed me from an unsure graduate student into a confident scientist. My committee members, Dr. Brendan Roark, Dr. Shari Yvon-Lewis, Dr. Steve DiMarco and Dr. Niall Slowey, have offered their tremendous knowledge and encouragement throughout the course of my Ph.D. and these research projects. I am incredibly grateful to have had such a supportive committee. I would also like to thank the entire Oceanography department staff, faculty and students (particularly Natalie Zielinski, Noura Randle, Cody Webb and Michael Evans) for making my time at Texas A&M a wonderful experience. I thank the many programs and scholarships that provided funding and support for my Ph.D., including the NOAA Nancy Foster Scholarship, Texas Sea Grant, Kamehameha Schools, NSF STEM, Lechner Scholarship, Louis and Elizabeth Scherck Scholarship, Michel T. Halbouty/AAPG Foundation Endowed Fellowship, and the Texas Alliances for Graduate Education and the Professoriate (AGEP). Finally, I would like to thank my mother, father, brother, and extended family for fostering my love for the ocean, providing the foundation for my oceanographic knowledge, and supporting me throughout my academic journey.

CONTRIBUTORS AND FUNDING SOURCES

This work was supervised by a dissertation committee consisting of Dr. Katie Shamberger, Dr. Shari Yvon-Lewis, Dr. Steve DiMarco and Dr. Niall Slowey of the Department of Oceanography and Dr. Brendan Roark of the Department of Geography. The analysis and interpretation of data in Chapter II was conducted by myself and supported through the efforts of Kathryn E. F. Shamberger, Steven F. DiMarco, Kristen M. Thyng, Robert D. Hetland, and Niall C. Slowey of Texas A&M University, as well as Derek P. Manzello and Ian C. Enochs of NOAA's Atlantic Oceanographic and Meteorological Laboratory. Data collection, analysis and interpretation for Chapter III were conducted by the combined efforts of myself, Shawn M. Doyle, Kathryn E.F. Shamberger, Jason B. Sylvan, Robert D. Hetland, and Steven F. DiMarco, all of Texas A&M University, and this manuscript is currently in review in *Coral Reefs*. Data collection, analysis and interpretation of Chapter IV was led by myself and Kathryn E. F. Shamberger, with valuable input and support from others. The physical oceanography data in Chapter IV was analyzed, in part, by Emma Reid and Kristen Davis of the University of California at Irvine as well as Steven Lentz of Woods Hole Oceanographic Institute. Particulate organic matter and isotope analyses were performed in the Stable Isotope Facility at Texas A&M University by Christopher Maupin, under the advisement of Brendan Roark. Other important contributors to this work include Michael Rappe and Shimi Rii of the Hawai‘i Institute of Marine Biology, and Rusty Brainard and Tom Oliver of NOAA's Coral Reef Ecosystem Program.

TABLE OF CONTENTS

Page

LIST OF FIGURES

Page

LIST OF TABLES

Page

CHAPTER I

INTRODUCTION

Coral reefs are one of the most biologically productive and diverse ecosystems on the planet, and contain about one-third of the world's marine fish, despite covering only ~0.1% of the ocean floor (Spalding and Grenfell 1997). They provide a myriad of goods and services that support economic and human health including food, tourism revenue, coastal protection, cultural sustenance and medical treatments (Moberg and Folke 1999). However, the health and persistence of coral reefs is severely threatened by global stressors such as ocean warming, ocean acidification and hypoxia. Concern for their long-term sustainability and resilience in response to these threats has resulted in a growing body of research that seeks to understand the environmental factors that support or inhibit coral reef growth.

Tropical coral reefs are constrained by a narrow range of latitudinal limits that encompass environmental conditions (e.g., temperature, light, calcium carbonate ($CaCO_3$) saturation state (Ω)) conducive to coral reef growth. In general, most reef-building corals live within the temperature and aragonite saturation state (Ω_{ar}) ranges of ~18-30°C and 3.4-3.8, respectively (Kleypas et al. 1999). However, biological processes (i.e., photosynthesis, respiration, calcification and dissolution) can drive Ω_{ar} beyond this range over hourly, diel, seasonal, and interannual time scales (e.g., Shamberger et al. 2011; Albright et al. 2013; Shaw et al. 2015). Superimposed on the natural variability is the long-term trend of rising ocean temperatures and decreasing surface water Ω_{ar}

resulting from climate change (Levitus et al. 2000; Caldeira and Wickett 2003). Understanding ecosystem response to both natural and anthropogenic-driven trends in ocean chemistry is critical to evaluating the persistence of coral reefs over time.

Rising atmospheric carbon dioxide (CO_2) concentrations linked to fossil fuel burning causes ocean warming and a subsequent increase in the frequency of mass coral bleaching events (Hughes et al. 2017). Bleaching is triggered by environmental stress (e.g., high temperatures, pollution or low salinity), which causes corals to expel their symbiotic algae (i.e., zooxanthellae). Since these algae can provide corals with up to 100% of their daily metabolic needs, the absence of zooxanthellae during bleaching events leads to a loss of their primary food source and increased susceptibility to mortality (Brown 1997 and references therein). Some studies have shown that stressed corals can upregulate heterotrophic feeding in the absence of zooxanthellae, but this response is limited to select coral species (Grottoli et al. 2006).

The surface ocean is responsible for absorbing approximately 25% of the anthropogenic CO_2 released into the atmosphere (Le Quéré et al. 2018), which causes an increase in the hydrogen ion concentration ($[H^+]$) (i.e., decrease in pH and increase in acidity) and bicarbonate ion concentration ($[HCO_3^-]$) according to the reaction:

$$CO_2 + H_2O \leftrightarrow H^+ + HCO_3^-$$

The excess H^+ combines with carbonate ions (CO_3^{2-}) to form more HCO_3^-, which ultimately leads to a decline in the concentration of CO_3^{2-}. This process is referred to as ocean acidification (Caldeira and Wickett 2003; Doney et al. 2009) and has been

documented at several open ocean time-series stations including in the North Pacific, Atlantic and Caribbean Sea (Bates et al. 2014).

Corals and other important coral reef calcifiers (e.g., mollusks and crustose coralline algae) that create the three-dimensional structure of a coral reef secrete aragonitic shells made out of calcium ions (Ca^{2+}) and CO_3^{2-}. Hence, a decline in the concentration of CO_3^{2-} ($[CO_3^{2-}]$) as a result of ocean acidification means that calcifiers will have a more difficult time forming their shells and skeletons (Langdon et al. 2000; Doney et al. 2009). The saturation state of aragonite is expressed as:

$$\Omega_{ar} = \frac{[Ca^{2+}] \times [CO_3^{2-}]}{K_{sp}}$$

where $[Ca^{2+}]$ is the concentration of Ca^{2+} in seawater and K_{sp} is the solubility product at *in situ* temperature, salinity and pressure. Saturation state is useful for determining the thermodynamic response with respect to the formation or dissolution of calcium carbonate ($CaCO_3$). If $\Omega_{ar} > 1$ then precipitation is favored and if $\Omega_{ar} < 1$ then dissolution is favored. Currently, the ocean is supersaturated with respect to aragonite but undersaturation is expected to occur in high-latitude oceans as early as the year 2020, and will expand into the North Pacific by the year 2100 (Feely et al. 2009).

Eutrophication, which is driven by nutrient loading linked to agricultural and urban anthropogenic activities, has led to an increase in the occurrence, persistence and extent of hypoxia (defined as <2 ml L^{-1} of dissolved oxygen) in coastal regions (Diaz and Rosenberg 2008). Responses of organisms to stress from hypoxia varies based on the length and frequency of exposure to low oxygen, but includes forced migration,

reduced growth, physiological stress and mortality (Breitburg 2002; Rabalais et al. 2002). One of the most well-studied hypoxic areas is in the northern Gulf of Mexico (Rabalais et al. 2002; Bianchi et al. 2010). Here, a combination of high nutrient loads and freshwater discharge, and summer warming and stratification, leads to the formation of seasonal hypoxia that is present from late spring through summer.

Hypoxia as a global threat to coral reefs is an emerging concern. However, coral reef hypoxia has not been well-documented, possibly because hypoxia is often studied in temperate rather than tropical regions, coral reef monitoring studies rarely include the measurement of oxygen, hypoxic events may be short-lived, and/or most coral reefs worldwide are not routinely studied (Altieri et al. 2017). However, recent studies have emerged and implicated hypoxia as the cause of some coral reef mortality events (Altieri et al. 2017; Baird et al. 2017; Gajdzik and DeCarlo 2017; Nelson and Altieri 2019). These studies have shown that hypoxic events were preceded by high sea surface temperatures, low wind speeds and restricted circulation, and were typically associated with coral bleaching.

The overall purpose of this dissertation research is to provide information on the environmental conditions and processes that support or inhibit coral reef growth, and understand how changing conditions will affect future ecosystem health. In the second chapter, we provide the most comprehensive analysis, to date, of surface seawater CO_2 system dynamics in the GoM and set the stage for future work examining the sensitivity of GoM ecosystems, including the coral reefs of the Flower Garden Banks (FGB), to ocean acidification and global change. The third chapter characterizes water chemistry

and microbial communities within the FGB following a hypoxia-driven localized mortality event, and investigates the potential mechanisms leading to this event. In the fourth chapter, we investigated net ecosystem calcification (NEC; calcification-dissolution) and oceanic particulate organic carbon (POC) uptake at Kāneʻohe Bay barrier reef in Hawaii, and show evidence for a significant, positive correlation between these two parameters. This was the first study to find a direct connection between NEC and oceanic POC uptake and suggests that while heterotrophy may increase resistance to climate change stressors, the documented decline in oceanic productivity could also lead to lower rates of coral reef calcification. I conclude this dissertation in Chapter V by summarizing the major findings of these studies and providing recommendations to guide subsequent, complimentary research that will aid in our understanding of future coral reef health under a multi-stressor ocean.

CHAPTER II

CO_2 VARIABILITY IN THE GULF OF MEXICO (1996-2017)

Introduction

Since the onset of the Industrial Revolution, atmospheric carbon dioxide (CO_2) has increased by approximately 40% (Le Quéré et al. 2018). The ocean is responsible for absorbing ~25% of anthropogenic CO_2 emissions, which modulates climate by reducing global warming. However, oceanic absorption of atmospheric CO_2 also leads to an increase in seawater partial pressure of CO_2 (pCO_2), and a decrease in seawater pH and saturation state (Ω) (Caldeira and Wickett 2003; Feely et al. 2004). This process, termed ocean acidification, has numerous negative consequences for marine organisms, especially those that form calcium carbonate ($CaCO_3$) skeletons and shells (e.g. corals and shellfish), including a reduction in biogenic calcification and an increase in $CaCO_3$ dissolution (Andersson et al. 2009; Shamberger et al. 2011; Albright et al. 2013; Shaw et al. 2015; Enochs et al. 2016).

Gulf of Mexico (GoM) ecosystems support fisheries that are essential to the Gulf Coast and U.S. economies. The 2015 GoM seafood landings revenue was $858 million, which is almost 20% of the total U.S. landings revenue (National Marine Fisheries Service 2017). Despite serving as a critical component for regional economic stability, the GoM is subject to numerous anthropogenic pressures that contribute to the decline of ecosystem health, including eutrophication, hypoxia, oil spills, warming, and acidification (Scavia et al. 2002; Cai et al. 2011; Laurent et al. 2017). Hypoxia in the

northern GoM is driven by the spring flux of nutrients from the Mississippi and Atchafalaya River System combined with water column stratification that prevents mixing of bottom waters with oxygenated surface water (Rabalais et al. 2002; Belabbassi et al. 2005; Bianchi et al. 2010). The production of CO_2 through respiratory processes also lowers pH (i.e., increases acidity) (Cai et al. 2011). Hypoxia and associated bottom water acidification, along with global ocean acidification, are predicted to intensify with future climate change, making acidification-induced stresses highly relevant for GoM ecosystems.

In an effort to characterize GoM carbonate chemistry trends, several studies involving both observational and model data have been conducted (Gledhill et al. 2008, 2009; Keul et al. 2010; Wang et al. 2013a; Huang et al. 2015a; b; Wanninkhof et al. 2015; Chen et al. 2016; Xue et al. 2016). Much of the carbonate chemistry work done thus far has focused on northern GoM continental shelf waters, where Mississippi and Atchafalaya River outflow and seasonal bottom water hypoxia occur (Keul et al. 2010; Huang et al. 2015a; b). Surface CO_2 is elevated immediately adjacent to these river mouths due to the high pCO_2 (~2000 μatm) of river water combined with turbidity that blocks sunlight and inhibits photosynthesis (Huang et al. 2015a). On the inner shelf, mixing of freshwater and seawater drives outgassing of CO_2 (Cai 2003a; Lohrenz and Cai 2006; Huang et al. 2015a). Riverine nutrients enhance productivity further lowering CO_2 and dissolved inorganic carbon (DIC). Shelf surface water CO_2 and DIC is therefore lower than offshore concentrations, with the lowest concentrations observed on the Louisiana shelf near the Mississippi and Atchafalaya River outflow (Wang et al.

2013a). Total alkalinity (TA) (mostly in the form of bicarbonate) in the freshwater end-member is highly variable, and depends on the volume of river discharge available to dilute the weathering signal produced by the dissolution of continental rock minerals, which varies seasonally (Cai 2003a; Lohrenz and Cai 2006; Cai et al. 2010). Photosynthetic drawdown of shelf surface water DIC increases TA:DIC (to approximately 1.24), aragonite saturation state (Ω_{ar}; to > 5) and the buffering capacity of Louisiana shelf water (Wang et al. 2013a; Wanninkhof et al. 2015). In addition, seasonal CO_2 trends have been identified on the shelf. Seasonal trends in nutrient inputs and temperature cause the northern GoM and west Florida shelves to act as sinks for atmospheric CO_2 in the winter and spring, and sources of atmospheric CO_2 in the summer and fall (Chen et al. 2016; Robbins et al. 2018). The western GoM shelf is less influenced by fluvial nutrient inputs from the Mississippi and Atchafalaya rivers and serves as a CO_2 source for most of the year, except during winter when temperatures are low (Xue et al. 2016).

Compared to coastal waters, GoM open ocean carbonate chemistry is considered to be fairly stable. Temperature drives CO_2 variability and the open ocean has been shown to be a sink for atmospheric CO_2 for most of the year, except during the summer when temperatures are high (Coble et al. 2010; Xue et al. 2016). Offshore surface TA:DIC (~1) and Ω_{ar} (~4) are fairly constant and primarily influenced by evaporation and dilution (Wanninkhof et al. 2015). The Loop Current originates in the Caribbean, enters the GoM through the Yucatan Strait, extends north toward the shelf and exits

through the Straits of Florida. This warm water current delivers relatively low pCO_2 and DIC, and high TA water into the GoM (Gledhill et al. 2008; Wang et al. 2013a).

Although regional and seasonal GoM carbonate chemistry trends have been identified, there are also some discrepancies across studies. For example, Chavez et al. (Chavez et al. 2007) classified the entire GoM as a net annual CO_2 source to the atmosphere, while more recent studies characterize the GoM as an annual CO_2 sink (Coble et al. 2010; Robbins et al. 2014; Xue et al. 2016). Xue et al. (Xue et al. 2016) and Huang et al. (Huang et al. 2015a) found the northern GoM shelf serves as an annual CO_2 sink but Xue et al. (Huang et al. 2015a) showed strong, cross-shelf variations that were linked to seasonal and spatial salinity gradients. In addition, the coupled physical-biogeochemical model developed by Xue et al. (Xue et al. 2016) simulated higher summer pCO_2 values on the northern GoM shelf than are shown in the observational data. Discrepancies between studies are likely the result of the dynamic physical (e.g. shelf circulation) and biological (e.g. organic metabolism) controls on coastal pCO_2, which introduces variability on multiple time and space scales.

The objective of this paper is to synthesize all publicly available, underway surface seawater CO_2 data in the GoM in order to investigate spatial, seasonal, and long-term basin-wide trends. This analysis avoids the spatial and temporal limitations of subregion-specific observational studies while still allowing for detailed assessments over small spatial scales. The limitations of this dataset include a bias towards spring and summer observations; incomplete spatial coverage in the western GoM and on the West Florida and Mexican continental shelves; and limited spatial and temporal overlap

between datasets. Nevertheless, this study is the most comprehensive compilation of GoM observational CO_2 data to date, includes a 65% increase in the number of observations since the last synthesis report of Robbins et al. (Robbins et al. 2014), and allows for the examination of surface CO_2 system dynamics at a regional scale over more than two decades. As CO_2 measurements continue to be collected, it will be important to update this analysis in order to assess the GoM CO_2 system response to regional and global perturbations.

Methodology

Approximately 621,000 underway measurements of sea surface temperature (SST), sea surface salinity (SSS) and surface seawater CO_2 within the GoM spanning 1996-2017 were used in this analysis. The data were separated into regions of the coastal (0-200 m depth) and open ocean GoM (>200 m depth, i.e. beyond the continental shelf). There are approximately 261,000 coastal measurements and 360,000 open ocean measurements and the majority of data (99%) were collected after 2001. Summer (Jun-Sept: ~256,000) and spring (Mar-May: ~210,000) seasons account for 75% of the dataset with far fewer measurements collected during the winter (Dec-Feb: ~85,000) and fall (Oct-Nov: ~70,000) seasons (Fig. 2.1).

Databases

To ensure the most comprehensive compilation of data, continuous measurements of SST, SSS and surface seawater CO_2 within the GoM were downloaded from Surface Ocean CO_2 Atlas (SOCAT v6, Bakker et al. 2016), Lamont-Doherty Earth Observatory (LDEO, Takahashi et al. 2017) database and NOAA's National Centers for

Environmental Information (NCEI) for the years 1996-2017. Since these repositories contain some of the same datasets, duplicates were identified and removed. SOCAT data are reported in fCO_2, and for consistency across all datasets, were converted to pCO_2. These publicly available data were made possible by the hard work of many groups including: (Gledhill et al. 2008; Keul et al. 2010; Lohrenz et al. 2010; Huang et al. 2013, 2015a; b; Wang et al. 2013a; Wanninkhof et al. 2015) and others.

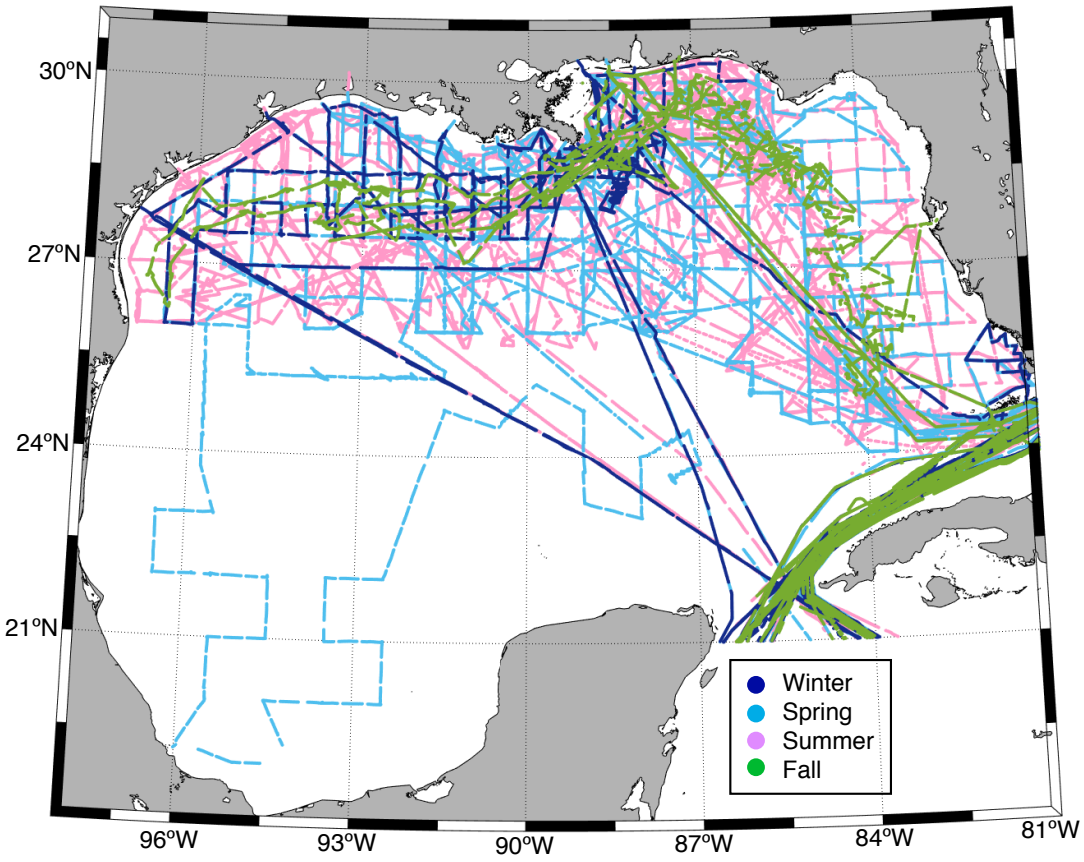

Figure II.1 Approximately 621,000 underway measurements were collected between 1996 and 2017. Measurements are colored according to season: winter (dark blue), spring (light blue), summer (pink) and fall (green).

Underway Data

Although underway CO_2 systems vary slightly across research vessels, there are general principles of operation and quality control procedures (Pierrot et al. 2009). pCO_2 was calculated using SST measured at the intake port, temperature and pressure of the equilibrator, water vapor pressure, and atmospheric pressure (Pierrot et al. 2009). Seawater is drawn in from an intake port located 5 m below the sea surface and circulated through a chamber which allows for CO_2 equilibration between the water and overlying air. To limit the effects of water vapor, the head space gas travels through a condenser and Nafion tube before the CO_2 mole fraction is measured by an infrared gas analyzer (IRGA). In most cases, the IRGA is calibrated using four CO_2 gas standards within the range of 200-450 ppm in order to verify an accuracy within ± 2 ppm. Approximately 50,000 measured values in this dataset were beyond the standard range, and should be considered accurate to within ± 5 ppm. A typical sequence consists of 60 equilibrator samples, six atmospheric boundary layer samples and one set of calibration gases, each measured at 2-min intervals.

During some cruises the salinity or temperature sensor malfunctioned, or the range of surface seawater CO_2 observations was well beyond the range of calibration gases. These data were flagged as questionable in the original datasets or metadata, and examined individually for quality control. In cases of obvious drift in the IRGA (e.g., a large increase in pCO_2 in open ocean water with no change in salinity or temperature), or when the salinity/temperature sensors were not working for an extended period of time (e.g., hours to days), the data were removed from this analysis. This led to the removal

of ~50,000 measurements. Another ~65,000 measurements were removed due to duplications across datasets. After these quality control procedures were performed, approximately 621,000 of the initially downloaded ~740,000 measurements were used in this analysis.

The calculation for air-sea CO_2 flux (F) is given as: $F=k\alpha\Delta pCO_2$, where k is the gas transfer velocity, α is the solubility of CO_2 in seawater at in situ temperature and salinity (Weiss 1974), and ΔpCO_2 is the seawater pCO_2 minus the atmospheric pCO_2. Positive (negative) F represents a CO_2 flux from the ocean to the atmosphere (atmosphere to the ocean). The wind speed parameterizations for k proposed by Ho et al. (Ho et al. 2006) and Wanninkhof (Wanninkhof 1992) were used to calculate F to be consistent with previous studies that used Wanninkhof (Wanninkhof 1992) and to compare results between different parameterizations. Since atmospheric CO_2 data were not collected during every cruise, the monthly CO_2 record at the Mauna Loa Observatory (https://www.esrl.noaa.gov/gmd/ccgg/trends/data.html) was used in the CO_2 flux calculation. Atmospheric CO_2 data are initially reported as a mole fraction in dry air. These data were corrected to 100% humidity by computing the water vapor pressure at SST and SSS, then converting to pCO_2 using the instantaneous pressure reported in the underway datasets (Weiss and Price 1980). Daily average winds speeds at each location were obtained from the Cross-Calibrated Multi-Platform (CCMP) Wind Vector Analysis Product v2, which are referenced to a height of 10 m. Important to note is that there is only a single spring dataset in the southwestern GoM (18-25 ºN, 87-97 ºW) (Fig. 2.1), which means that the open ocean and coastal CO_2 summer, fall, and winter flux

estimates reported in this study do not include this region and the spring flux estimates do not incorporate a comprehensive representation of this region. The southwestern GoM is one of the major gaps in our knowledge of the GoM CO_2 budget.

To aid in examining pCO_2 trends driven by processes other than changing temperature (e.g. biological productivity), pCO_2 was normalized to a constant temperature ($n$$pCO_2$). The effects of temperature on isochemical water conditions for a temperature range of 2-28 °C and salinity range of 34-36 is 0.0423 C^{-1} is given by the equation: $n$$pCO_2$=$pCO_{2insitu}$*exp(0.0423*($SST_{mean}$-$SST_{insitu}$)), where $pCO_{2insitu}$ and SST_{insitu} are the measured values and SST_{mean} is the annual mean SST (26.71°C) of the entire dataset (Takahashi et al. 1993, 2002). This relationship has previously been used across the global surface ocean, including in the GoM (Takahashi et al. 2002, 2009). Although summer SSTs in the GoM sometimes exceed 30°C, in general, temperatures are within the range of 2-28°C (Fig. A-1). Coastal salinity is highly variable, particularly near the river mouths (Fig. A-2). For a fixed TA and DIC, the pCO_2 increase or decrease °C^{-1} at a salinity of 5 is about half the change of a water sample with a salinity of 35. Furthermore, freshwater TA can be significantly different from open ocean TA. Therefore, although we have calculated $n$$pCO_2$ for the entire dataset, care must be taken when interpreting absolute values in areas that encompass a wide range of salinity values. While important to consider, especially in localized areas with strong salinity gradients, these confounding factors have a minimal effect on the interpretation of the overall trends.

In order to evaluate long-term pCO_2 trends, we followed the deseasonalization procedure described in Takahashi et al. (2009). Briefly, we estimated the seasonal trend by calculating a monthly mean from the 20 year data composite and an annual mean from each monthly mean. The difference between the monthly mean and the annual mean is the correction applied to the monthly mean of each individual year (i.e., the deseasonalization). The deseasonalization was performed for the coastal ocean (0-200 m) and open ocean (>200 m) separately, and assumes that the seasonal trends and corrections do not change over the time period covered by the dataset.

Empirical Orthogonal Function

A Principal Component Analysis (PCA), or equivalently Empirical Orthogonal Function (EOF) analysis (Thomson and Emery 2014), decomposes the input data into a linear combination of statistically independent (orthogonal) basis functions. The basis functions are the eigenvectors of the covariance matrix of the input data and are referred to as the modes of variability. The amplitudes of the basis functions are estimated as the projections of the eigenvectors onto the original data set. The eigenvalues of the covariance matrix represent the fractional percent of variance each eigenvector represents in the original data set. The EOF amplitudes can be interpreted spatially and temporally to identify patterns that can be associated with process mechanisms. The number of independent modes, (i.e., eigenvectors), is limited to the number of variables used in the calculation, which in this case is four: SST, SSS, pCO_2 and $n pCO_2$. The analysis was performed separately on GoM coastal (0-200 m) and open ocean data (>200 m) since drivers behind variability can be different in these regions. The results of the

analyses presented in Section 3.4 show that despite the number of EOF modes being limited to four, discernable temporal and spatial patterns emerge that are interpretable as being related to seasonal variability and proximity to terrestrial freshwater sources. The interpretations are necessarily broad due to the limited number of variables. However, in future studies the addition of other variables (e.g., currents, nutrients and other carbonate parameters) will better focus the processes responsible for the variances.

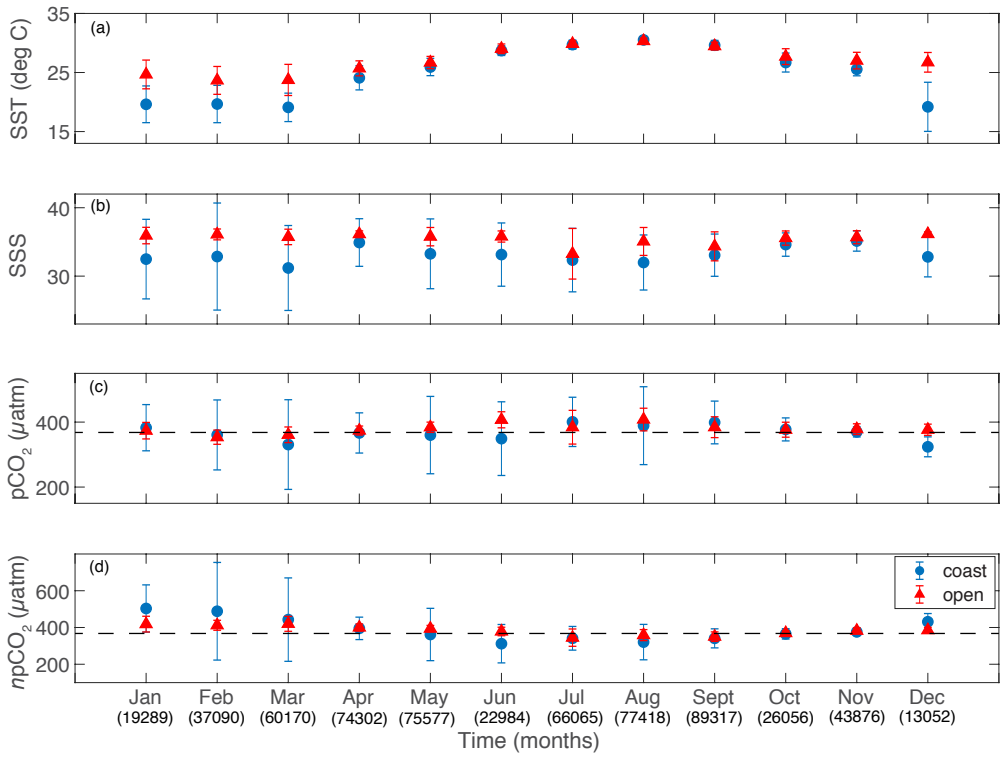

Figure II.2 Monthly mean sea surface temperature (SST in °C) (a), sea surface salinity (SSS) (b), sea surface partial pressure of CO_2 (pCO_2 in µatm) (c) and temperature-normalized sea surface pCO_2 ($npCO_2$ in µatm) (d). Coastal means (± std) are represented by the blue circles and open ocean means (± std) are shown by the red triangles. The dotted lines represent mean atmospheric CO_2 concentration (376 ± 6 µatm) over the study period. The number of measurements included for each month are given in parentheses on the x-axis.

Results

Open Ocean GoM

Open ocean SSTs ranged from 13.4 °C to 32.2 °C, with the lowest mean SSTs occurring in winter (Dec-Feb) to early spring (Mar-May) (March mean SST=23.7± 2.4 °C; means presented as the average of all data collected during each month or season ± one standard deviation throughout) and maximums occurring in the summer (Jun-Sep) (August mean SST=30.3±0.5 °C) (Figs. 2.2 and A-1; colormaps herein from Thyng et al (Thyng et al. 2016)). Average open ocean SSS was 35.3±2.0 (range=18.3-37.2) (Figs. 2.2 and A-2). Monthly averaged salinity was fairly constant, except in July when the mean value decreased to 33.3±3.7. The seasonal cycle of pCO_2 (range=124-508 µatm) mirrored SST, with lower levels in the winter (February mean pCO_2=354±22 µatm) and higher levels in the summer (August mean pCO_2=408±35 µatm) (Figs. 2.2 and 2.3). pCO_2 normalized to an annual mean temperature ($npCO_2$) ranged from 125-648 µatm, with the lowest monthly means in summer (July mean *n*pCO2=345±47 µatm) and the highest monthly means in late winter through early spring (March mean $npCO_2$=420±41 µatm) (Figs. 2.2 and A-3). The average annual increase in deseasonalized open ocean pCO_2 from 1996-2017 was 1.2±0.3 µatm yr^{-1} (R^2=0.12, $p<0.001$) (Fig. 2.4).

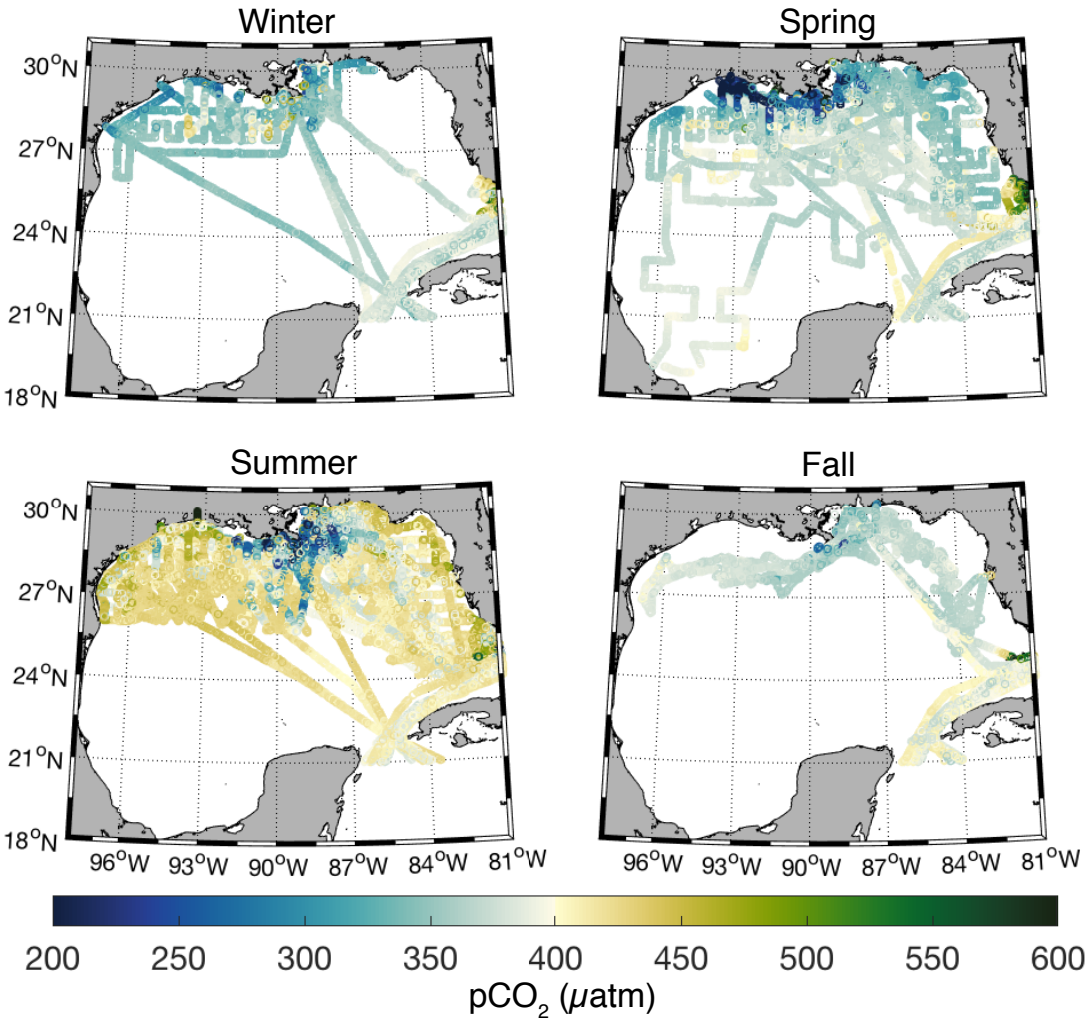

Figure II.3 Surface seawater CO_2 partial pressure (pCO_2 in µatm) during winter, spring, summer and fall. Note that the actual minimum and maximum values are 69 and 2084 µatm, respectively.

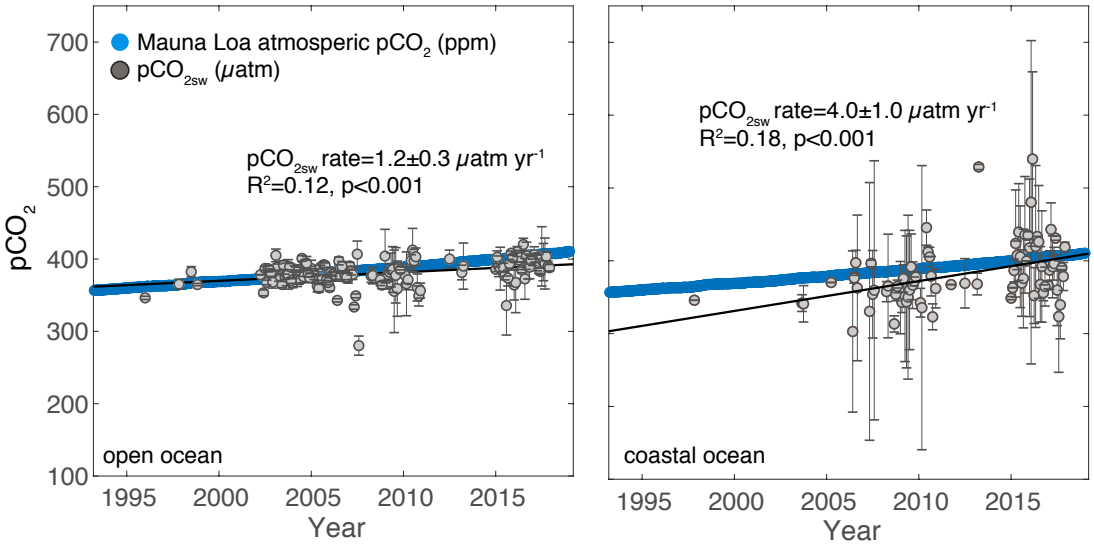

Figure II.4 Time-series (1996-2017) of monthly-averaged deseasonalized pCO_2 (gray circles with error bars representing ±standard deviation) in the open (left panel) and coastal (right panel) ocean Gulf of Mexico. The black lines represent the linear trends for seawater pCO_2 (pCO_{2sw}) with slope, R^2, and p-values shown in each panel. The Mauna Loa atmospheric CO_2 record is shown in blue.

Air-sea CO_2 fluxes for both wind speed parameterizations (Wanninkhof 1992; Ho et al. 2006) agreed well (fluxes reported in the text and Table 2.1 are calculated using the parameterization of Ho et al. (Ho et al. 2006) and fluxes for both parameterizations are shown in Fig. A-4). Open ocean air-sea CO_2 fluxes ranged from -7.71 to 6.03 mol C m^{-2} yr^{-1} with an annual mean of -0.05±0.42 mol C m^{-2} yr^{-1} indicating that the open ocean shows some seasonal variability, but is roughly balanced in terms of source and sink characteristics on an annual basis (Fig. 2.5; Table 2.1). Since the majority of measurements were collected in the spring and summer, calculating the average annual flux based on all values introduces a seasonal bias. Hence, the average annual flux was calculated from the mean seasonal fluxes shown in Table 1. In the summer, the open ocean was a source for CO_2 (0.15±0.60 mol C m^{-2} yr^{-1}), with the greatest flux occurring in August (0.35±0.67 mol C m^{-2} yr^{-1}). The open ocean was a sink for CO_2 in the winter (-0.28±0.64 mol C m^{-2} yr^{-1}), whereas spring and fall fluxes were close to balanced and showed less variability than summer and winter (Table 2.1).

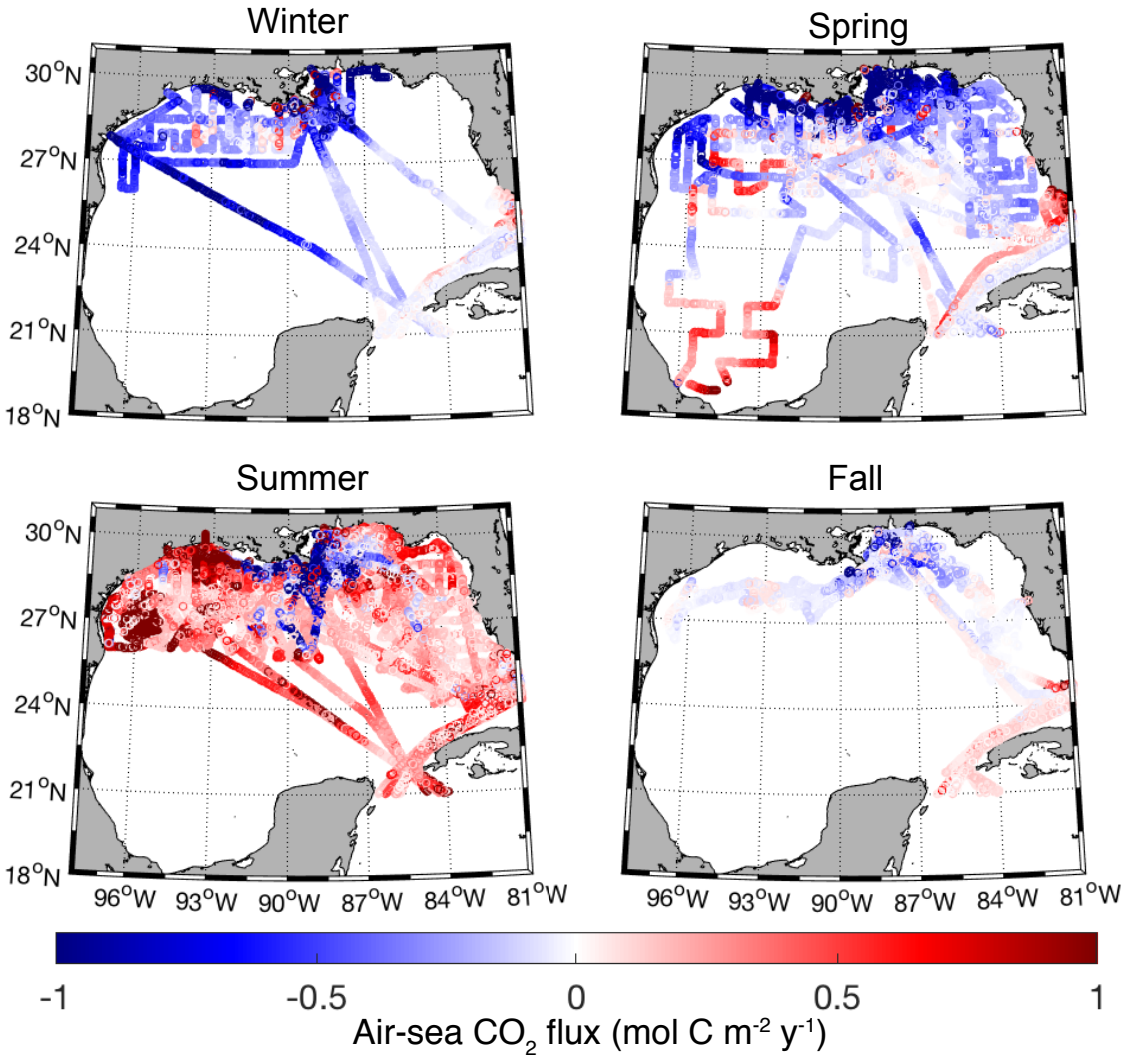

Figure II.5 Seasonal air-sea CO_2 fluxes (mol C m^{-2} yr^{-1}) calculated using the wind speed parameterization of Ho et al. (2006). Note that the actual minimum and maximum values are approximately -30 and 39 mol C m^{-2} yr^{-1}, respectively. Positive values (red symbols) indicate an oceanic CO_2 source to the atmosphere and negative values (blue symbols) indicate oceanic uptake of CO_2.

Table II.1 Seasonal and annual means, minimum month, and maximum month air-sea CO_2 fluxes (mol C m^{-2} yr^{1}) for the open and coastal ocean using the wind speed parameterizations of Ho et al. (2006). Positive fluxes indicate the ocean is a CO_2 source to the atmosphere while negative values indicate the ocean is a CO_2 sink.

Open Ocean			
Season	**Mean**	**Min**	**Max**
Winter	-0.28±0.64	-0.48± 0.84 (Feb)	0.06±0.18 (Dec)
Spring	-0.03±0.26	-0.20±0.27 (Mar)	0.05±0.26 (May)
Summer	0.15±0.60	-0.02±0.764 (Jul)	0.35±0.67 (Aug)
Fall	-0.04±0.18	0.04±0.19 (Oct)	-0.03±0.17 (Nov)
Annual	-0.05±0.42		
Coastal Ocean			
Season	**Mean**	**Min**	**Max**
Winter	-0.12±3.51	-0.46±0.26 (Dec)	-0.14±1.38 (Jan)
Spring	-0.47±2.06	-0.79±2.48 (Mar)	-0.26±1.40 (Apr)
Summer	0.15±1.29	-0.45±1.27 (Jun)	0.24±1.92 (Aug)
Fall	-0.09±0.29	-0.09±0.27 (Nov)	-0.07±0.29 (Oct)
Annual	-0.13±1.79		

Coastal Ocean

The monthly means of GoM open and coastal SST, SSS, and pCO_2, with the exception of SST from Dec-Mar, were not statistically different (Fig. 2.2). However, the

GoM coastal ocean was approximately two times more variable in SST and SSS and four times more variable in pCO_2, than the open ocean GoM. Coastal SSTs ranged ~8-32 °C, with the lowest mean value in March (19.1±2.5°C) and the highest mean value in August (30.5±0.6 °C) (Figs 2.2 and A-1). Salinities ranged from 0.1 to 40.3 along the shelf and minimum values were recorded near river mouths, particularly the Mississippi and Atchafalaya (Figs 2.2 and A-2). Winter, spring and summer displayed the lowest average salinities (~32), while fall had the highest salinity (35.0±1.5). The range for pCO_2 in the coastal region was 69-2084 µatm, with the lowest mean monthly values occurring in the winter (December mean=326±32 µatm) and highest mean monthly values in the summer (July mean=400±76 µatm) (Figs 2.2 and 2.3). When pCO_2 is normalized to an annual mean temperature (i.e., $n$$pCO_2$), the upper limit increased to 3061 µatm ($n$$pCO_2$ range=64-3061 µatm) due to the removal of the dampening effect of low winter temperatures on pCO_2 (Fig. A-3). Maximum pCO_2 and $n$$pCO_2$ values were recorded on the west Florida Shelf and in the river mouths. Lowest coastal ocean average $n$$pCO_2$ values occurred in the summer, particularly in June (312±104 µatm), and maximum average $n$$pCO_2$ values were in the winter (January mean=503±128 µatm) (Figs. 2.2 and A-3). The average annual increase in deseasonalized coastal pCO_2 from 1996 to 2017 was 4.0±1.0 µatm yr^{-1} (R^2=0.18, $p<0.001$), which is almost 4 times greater than the open ocean acidification signal (Fig. 2.4).

The annual mean air-sea CO_2 flux of the coastal ocean was slightly negative (mean=-0.13±1.79 mol C m^{-2} yr^{-1}) (Table 1) with a large range and variability (-29.91 to 38.57 mol C m^{-2} yr^{-1}) when compared to the open ocean (Fig. 2.5 and Table 2.1). Except

for the summer (mean=0.15±1.29 mol C m^{-2} yr^{-1}), the coastal ocean was a sink for CO_2 during all seasons, particularly during the spring (mean=-0.47±2.06 mol C m^{-2} yr^{-1}). Waters immediately adjacent to the major river mouths (Mississippi and Atchafalaya) were a year-round, source of CO_2 to the atmosphere (mean=6.74±10.90 mol C m^{-2} yr^{-1}, defined as waters with salinity less than 17) but cover a small geographic area of the GoM coastal ocean.

EOF Analysis

The results of the open ocean EOF show that about half of the observed variance is attributed to Mode-1, Mode-2 represents 38 % of the variance, and Mode-3 accounts for 10 %. Because of this distribution, only Modes 1 and 2 of the open ocean data decomposition are likely statistically significant (North et al. 1982). Based on examination of the magnitudes of the eigenvectors (Fig. 2.6, gray symbols), SSS and $npCO_2$ are positively correlated to each other and are strongly tied to Mode 1; SST is anti-correlated (i.e., of opposite sign) to SSS and $npCO_2$, but is of about equal magnitude. pCO_2 variability is weakly accounted for in Mode 1. It is therefore possible that Mode 1 represents a biological component linked to river discharge when warm, low salinity and low $npCO_2$ waters derived from the coast in the summer are advected into the oligotrophic open ocean, which is salty and comparatively cool. A map showing amplitudes of Mode 1 for each observation location (Fig. A-5, left panel) highlights the relationship of Mode 1 to the proximity of the Mississippi River delta in the northern GoM near 90ºW.

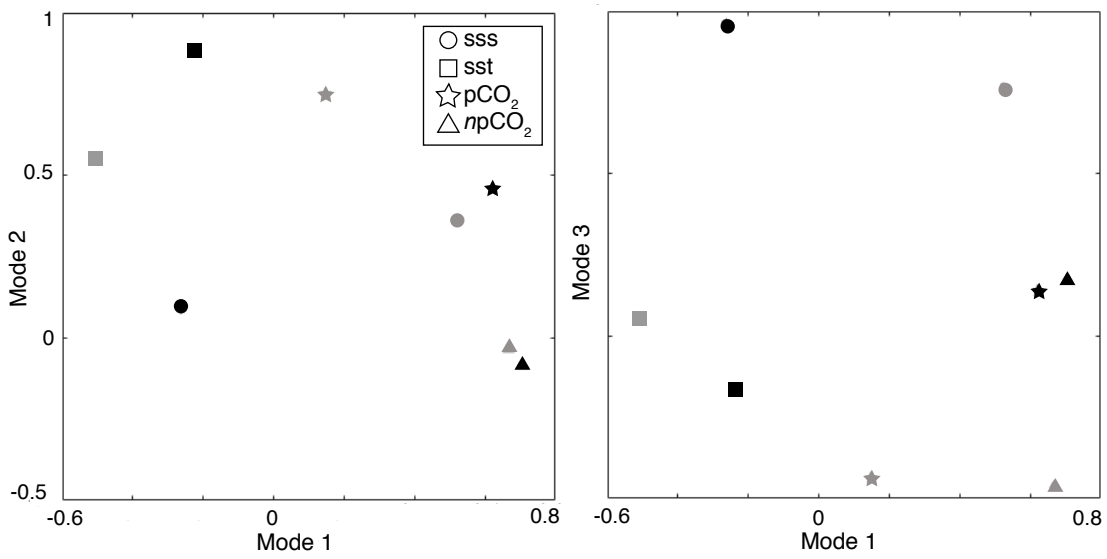

Figure II.6 EOF analysis of Mode 1 and Mode 2 (left panel) and Mode 1 and Mode 3 (right panel) for the coastal ocean (black symbols) and open ocean (gray symbols). The four parameters of the EOF analysis include sea surface salinity (sss, circles), sea surface temperature (sst, squares), sea surface partial pressure of CO_2 (pCO_2, stars) and temperature-normalized sea surface pCO_2 ($npCO_2$, triangles).

SST and pCO_2 load high, 0.55 and 0.7, respectively, for open ocean Mode 2 (Fig. 2.6, gray symbols), while SSS loading is relatively small (0.35) and $npCO_2$ is near zero. Examination of seasonal variability of Mode 2 shows a pronounced annual cycle that peaks in summer (June-August) and is of opposite sign in winter (February/March) (Fig. A-5: right panel). Therefore, Mode 2 is likely tied to seasonal changes in temperature. Mode 3 is not a significant component of the open ocean EOF but the amplitudes show that this mode is dominated by SSS, and all other amplitudes, SST, pCO_2, $npCO_2$, are relatively small. To summarize, the EOF shows that proximity to the Mississippi River plume accounts for more than half of the observed variance in the open ocean and the

remaining variance is accounted for by seasonal variations related to temperature.

In the coastal ocean, the EOF indicates that Mode-1 represents 46%, Mode-2 represents 30% and Mode-3 represents 24% of the observed variance in the data. Based on examination of the magnitudes of the eigenvectors (Fig. 2.6, black symbols), pCO_2 and $npCO_2$ are positively correlated to each other and strongly tied to Mode 1. There is also a small negative correlation of pCO_2 and $npCO_2$ to SST and SSS (i.e., high CO_2 implies low SST and low SSS and vice versa). There is a clear spatial pattern in Mode 1 that highlights the regions of the Louisiana continental shelf near the Mississippi-Atchafalaya Rivers, the middle West Florida Shelf, and Florida Bay to the south (green symbols, Fig. A-6, left panel).It is therefore likely that the coastal Mode 1 is linked to biological activity, which can be heavily influenced by nutrient loading from river water. Initially, river water has high CO_2, and low salinity and temperature. When mixed with shelf-water (higher salinity and temperature), degassing and photosynthesis decrease CO_2 in these waters.

Coastal ocean mode 2 variability is driven mostly by SST, as indicated by the high coefficient (0.9) (Fig. 2.6, black symbols). Mode 2 likely represents the seasonality of temperature. The coastal Mode 3 amplitude is dominated by the strong SSS value, ~0.9, and the spatial map of the Mode 3 amplitudes strongly highlights the locations in close proximity to the Mississippi River delta (Fig. A-6, right panel). Mode 3 therefore represents the importance of the Mississippi River alone in driving the salinity variability on the Texas-Louisiana Shelf. The results of the coastal EOF indicate about half of the observed variance can be attributed to biological processes, which can be

associated with terrestrial freshwater input, about a quarter of the variance can be attributed to seasonal temperature variations, and about a quarter of the observed variance can be attributed to salinity variability associated specifically with the Mississippi River.

We also examined the EOF results to investigate how the forcings of variability change over time. The open ocean data were separated into two temporal groups: 2007-2012 and 2013-2017. Data before 2007 were excluded due to limited temporal and spatial coverage in the earlier years. Regardless of time, the main driver of open ocean variability (i.e., Mode 1) is a biological component linked to river discharge and accounts for half of the variance in the dataset. The coastal ocean data were grouped into temporal groups of 2003-2010 and 2011-2017. Biological production remains as the main driver (i.e., Mode 1) over time, but its relative importance to the other modes increased from 46% in the earlier years to 58% in the latter years.

Discussion

Open Ocean

Spatial and temporal trends in GoM open ocean CO_2 are controlled by temperature, biological production, and physical forcings. Seasonal changes in temperature dominate the pCO_2 seasonal cycle with lower pCO_2 in the winter and higher pCO_2 in the summer (Fig. 2.2). This trend is a result of the effect of temperature on CO_2 solubility (i.e., higher temperature increases CO_2 solubility). However, the summer warming effect on CO_2 is partially offset by photosynthetic drawdown of CO_2 as shown by the winter-to-summer decrease of approximately 50 μatm in $npCO_2$ (Fig. 2.2).

Organic production associated with freshwater input is the primary driver of variability in the open ocean data (Fig. A-5). This is due to cross-shelf transport events like the one that occurred in July 2009 (Huang et al. 2013, 2015b; Xue et al. 2013; G.Fichot et al. 2014; Chakraborty and Lohrenz 2015), when low pCO_2 and low salinity water extended from the coast, beyond the shelf break, and greater than 300 km offshore (Fig. 2.7). River flow during 2009 was higher than average (220,000 m^3 s^{-1} compared to an annual average of 174,000±32,800 m^3 s^{-1} (http://rivergages.mvr.usace.army.mil/; station 01100Q)). Persistent winds drove coastal surface currents and the river plume upcoast (eastward) and offshore (http://pong.tamu.edu; http://tabs.gerg.tamu.edu, Buoy R) (Fig. A-7), causing low-salinity and low CO_2 freshwater discharge to pool within the north central and northeastern GoM (Li et al. 1997; Chen et al. 2000). Sea surface height anomalies obtained from the Colorado Center for Astrodynamics Research (CCAR) reveal two cyclonic eddies located in the northeastern GoM during July 2009 (Fig. A-8). These eddies, which have -30 cm and -20 cm sea surface height anomalies at the eddy core, are located along the boundary of the prominent anticyclonic eddy shedding off the Loop Current. As these eddies impinge on the continental shelf, they enhance cross-shelf exchange by transporting coastal waters seaward (Biggs and Muller-Karger 1994; Zhang et al. 2012a). Cross-shelf transport of nutrient-rich coastal waters in July 2009 also led to anomalously high chlorophyll and organic matter concentrations, and low DIC in the oligotrophic open ocean (Huang et al. 2013, 2015b; G.Fichot et al. 2014).

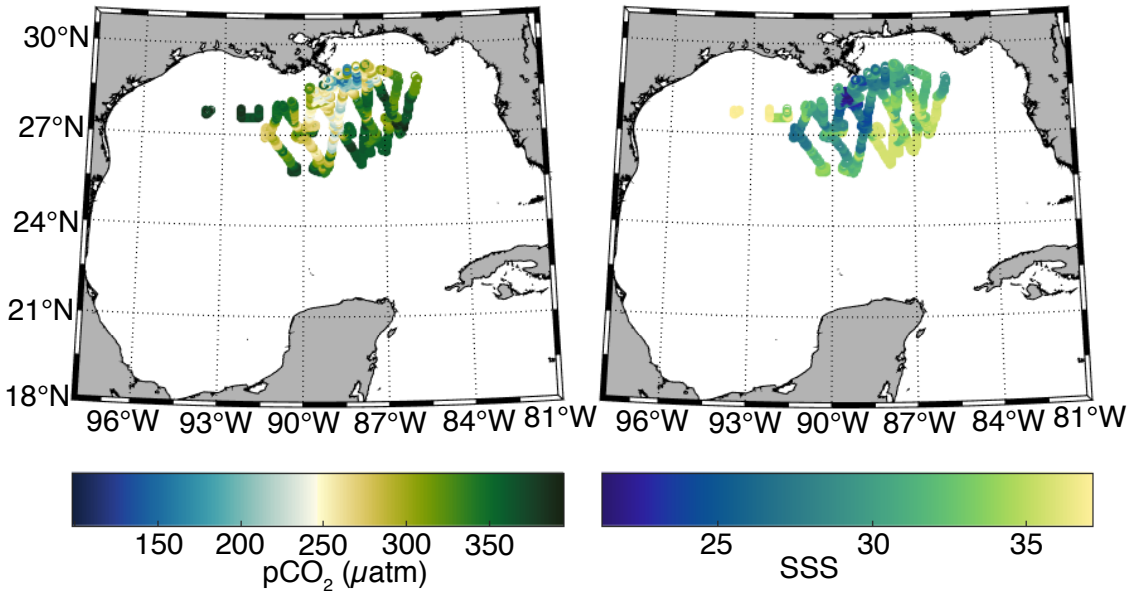

Figure II.7 Open ocean surface seawater partial pressure of CO_2 (µatm) (left panel) and sea surface salinity (right panel) during July 2009.

Open ocean GoM waters are typically a summertime source of CO_2 to the atmosphere, but this combination of physical processes can cause tens of thousands of square kilometers of the open ocean GoM to serve as a CO_2 sink. Underway data in this study show average open ocean pCO_2 during July 2009 (360 ± 57 uatm) is lower than for all years combined (373 ± 50 µtam), though not significantly different (Fig. 2.2). The patches of low pCO_2 and low salinity water in the area persisted through August and dissipated by October, indicating that the effects of these combined processes (high river flow, offshore currents, and eddy activity) on open ocean surface water CO_2 took about 1-2 months after peak spring flow to develop and lasted approximately three months. Processes that enhance exchange at the shelf break can therefore transport low salinity, low CO_2 and potentially nutrient-rich water associated with the Mississippi-Atchafalaya

Rivers hundreds of kilometers offshore, enhance CO_2 variability in the open ocean, and have the potential to impact north-central GoM open ocean ecosystems.

The chemical characteristics and spatial extent of the Loop Current also influence open ocean CO_2 variability. The Loop Current has been characterized by high temperature (~27.0°C), low DIC (2042 μmol kg^{-1}) and comparable TA (2399 μmol kg^{-1}), relative to surrounding GoM open ocean waters (Wang et al. 2013a). Xue et al. (Xue et al. 2016) classified the Loop Current as a strong, year-round CO_2 sink. Underway CO_2 measurements in this study show that waters within and just north of the Yucatan Strait are a CO_2 source during the summer and fall (Fig. 2.5), which suggests that treating the Loop Current as a year-round sink for atmospheric CO_2 may not be a good assumption. Intrusion of the Loop Current into the northern GoM can also entrain Mississippi-Atchafalaya River discharge, enhance cross-shelf exchange and transport low CO_2 and low DIC coastal water to the interior basin and out through the Florida Strait. Hence, spatial variability in the extension of the Loop Current as well as seasonal and interannual carbonate chemistry variability on the shelf, will influence the GoM open ocean inorganic carbon budget as well as the source water supplied to coral reef ecosystems of the Florida Reef Tract.

Air-sea flux estimates indicate the open ocean GoM is approximately neutral in terms of an annual source or sink for atmospheric CO_2 (-0.05±0.42 mol C m^{-2} yr^{-1}, Table 1). Model simulations showed the GoM open ocean is a strong annual CO_2 sink (-1.04±0.46 mol m^{-2} yr^{-1} C), particularly in the winter (-2.44±0.49 mol m^{-2} yr^{-1} C) (Xue et al. 2016) while Robbins et al. (Robbins et al. 2014) classified the open ocean GoM as a

much smaller annual CO_2 sink (-0.48±0.07 mol m^{-2} yr^{-1} C. Discrepancies in the magnitude of the fluxes may result from interannual variability in cross-shelf events, differences in wind speed averages (10-day intervals (Xue et al. 2016) vs. monthly mean winds in Robbins et al. (Robbins et al. 2014) and here), binning and averaging of CO_2 data, time span of the dataset analyzed and spatial or seasonal sampling biases.

Coastal Ocean

The main drivers of spatiotemporal variability of coastal surface seawater CO_2 are biological production, which can be associated with river discharge, temperature and coastal water circulation. Nutrient loading enhances coastal biological production in the spring and results in low CO_2 on the northern GoM shelf despite increasing SSTs (Cai 2003a; Lohrenz and Cai 2006; Wang et al. 2013a) (Figs. 2.2 and 2.3). High summer SSTs cause coastal CO_2 to increase in most areas, except in the north central GoM, which is likely due to the residual effects of spring discharge and subsequent biological production. Low temperatures resulting from cooling of shallow coastal waters, the migration of cold fronts from the north that extend over the coastal region, and/or mixing with cold, freshwater outflow, cause coastal CO_2 to decline in the winter.

Surface currents play a key role in determining the spatial extent of Mississippi and Atchafalaya discharge and its influence on GoM coastal carbonate chemistry. The effect of coastal circulation on CO_2 variability on seasonal time scales is apparent through the salinity distribution over the coastal shelf during the spring and summer (Fig. A-2). Although river discharge peaks in the spring, the influence of these low salinity waters persists for several months. From the fall through spring, downcoast

(toward the west) currents carry river discharge along the inner shelf of the northwestern Gulf (Cochrane and Kelly 1986). Surface water CO_2 is low in these nutrient-rich, freshwater plumes due to elevated organic productivity (Figs. 2.3 and A-3). When the winds shift eastward in the summer, upcoast (toward the east) coastal currents drive oligotrophic open ocean waters onto the northwestern shelf (Chen et al. 2000). Westward flow of river discharge is restricted by the coastline causing these productive, low CO_2 waters to pool on the central and northeastern GoM shelves and even be transported offshore.

In general, coastal waters are a sink for atmospheric CO_2 during the winter and spring due to cooler temperatures and enhanced biological productivity, respectively; a CO_2 source during the summer due to increased temperatures; and neutral during the fall (Fig. 2.5; Table 2.1). These results are in general agreement with Xue et al. (Xue et al. 2016) although some spatial and seasonal differences do exist. For example, Xue et al. (Xue et al. 2016) characterizes the coastal shelf as a CO_2 source during the fall and found western GoM shelf waters to be a CO_2 source during the spring. Modeling studies have classified the west Florida shelf as a winter sink (Chen et al. 2016; Xue et al. 2016) though the underway data have revealed that there are limitations to modeling results in this region. In this study, the lone winter dataset for the west Florida shelf indicates this region is a strong winter CO_2 source, which is dramatically different from the surrounding shelf regions, despite similar temperatures (Fig. 2.5). Processes that could produce such high CO_2 levels include respiration in bottom waters followed by strong mixing, groundwater inputs or river discharge, and upwelling of deep, high CO_2 waters

onto the shelf. Most of the salinity measurements were >35 and do not indicate the presence of freshwater (Fig. A-2). Since this is the only publicly available west Florida shelf winter dataset we were able to access for this study, we are unable to determine whether this feature is persistent or anomalous.

GoM CO_2 System Dynamics on a Coral Reef Ecosystem

Coral reefs located on the Texas-Louisiana continental shelf, including the FGB, are essential GoM habitat that support valuable fisheries and tourism, and are impacted by Gulf-wide CO_2 system dynamics. The FGB coral reef communities grow on salt domes that rise from approximately 100 m depth to within 17 m of the ocean surface (Edwards 1971). As a high-latitude coral reef system, FGB corals are subject to low winter temperatures (~17°C; Buoy V, http://tabs.gerg.tamu.edu) and light levels, which may limit growth or influence community composition and structure (Kleypas et al. 1999; Deslarzes and Lugo-Fernández 2007). Despite somewhat marginal environmental conditions, the FGB National Marine Sanctuary contains some of the healthiest reefs remaining in the GoM, with average coral cover exceeding 50% (Johnston et al. 2013a). However, an unprecedented invertebrate mortality event occurred on the East Bank of the FGB in July 2016 (see Chapter III). In October 2016, higher than average ocean temperatures drove the largest-ever recorded bleaching event in FGB history (M. Johnson, NOAA FGBNMS, unpublished data). Since the FGB lie at the edge of the continental shelf, these coral reefs are influenced by both coastal and open ocean GoM processes. Understanding carbonate chemistry dynamics throughout the GoM directly informs the processes controlling the seawater-CO_2 system within this ecosystem, and

will lead to important information for predicting the long-term sustainability of these coral reefs.

Other than open ocean water, two major potential source waters that could significantly affect carbonate chemistry variability at the FGB include land-based freshwater discharge and deep water beyond the shelf break. Mississippi-Atchafalaya River water reaching the FGB may have variable TA and Ω_{ar} while deep water is acidified, with low pH and Ω_{ar} (Cai 2003b; Keul et al. 2010; Georgian et al. 2016). However, deep water typically has elevated nutrient concentrations, which may help to offset the negative effects of acidified water on calcification by providing extra nutrition for coral reef calcifiers (Cohen and Holcomb 2009). Thus, these two source waters could have very different effects on the health of FGB coral reef ecosystems.

Although the FGB is a relatively remote, oceanic reef system, low salinity water (<33) has been observed at the reefs following periods of anomalously high river flow. While these low-salinity waters are short-lived and typically confined to a shallow surface water layer that does not extend to the depth of the coral reef cap (~17 to 49 m), the impact of river discharge on the FGB coral reef ecosystems has been a subject of debate (Dodge and Lang 1983; Nowlin Jr et al. 1998). For example, terrigenous runoff contains particulate and dissolved organic matter, which could decrease light attenuation and inhibit photosynthesis. Mississippi River water also contains high nutrient concentrations and has been linked to eutrophication and hypoxia on the coast (Rabalais et al. 2002). Deslarzes and Lugo-Fernandez (2007) found that episodic low-salinity events reach the FGB, but these events were associated with low nutrient and

chlorophyll concentrations, suggesting that by the time freshwater reaches these reefs, the nutrients have already been consumed.

To evaluate the impact of freshwater discharge on carbonate chemistry at the FGB, approximately 11,000 underway measurements within 50 km of the EFGB, WFGB and Stetson Bank boundaries were collected during 2003, 2008, 2009, 2010 and 2013. Salinities less than 33 were measured by underway systems within ~15 km of the EFGB coral cap in the spring and summer of 2008, 2009 and 2010. As previously discussed, 2009 (220,000 m^3) was a higher than average Mississippi-Atchafalaya River System discharge year, but 2008 (218,400 m^3) and 2010 (195,000 m^3) were also relatively high flow years. The underway data show that fCO_2 in low salinity (i.e., <33) water near the FGB is within the range of open ocean GoM average fCO_2. This suggests that there has been enough time for mixing and/or air-sea CO_2 equilibration to remove any influence that river water may have on surface water CO_2. Furthermore, this indicates that nutrients from the freshwater have been depleted by the time they reach the FGB.

Long Term Trends

The underway CO_2 data presented here span 21 years, a sufficient length of time to detect changes in open ocean carbonate chemistry driven by ocean acidification (Dore et al. 2003, 2009, Bates et al. 2012, 2014). However, unlike the Hawaii Ocean Time-series (HOT) in the Pacific, the Bermuda Atlantic Time-series Study (BATS) in the Atlantic, the CArbon Retention In A Colored Ocean (CARIACO) time series station in the Cariaco Basin of the south Caribbean Sea, and other long-term time series programs, this dataset is inconsistent across time and space. Despite the non-ideal nature of this

dataset for examining interannual trends, there is evidence that ocean acidification is already affecting carbonate chemistry dynamics in the GoM open ocean. The time-series analyses reveal that open ocean pCO_2 is increasing at a rate of 1.2±0.3 μatm yr^{-1} (Fig. 2.4). This rate is comparable to the pCO_2 increase at HOT (1.72±0.09 μatm yr^{-1}), BATS (1.69±0.11 μatm yr^{-1}) and CARIACO (2.95±0.43 μatm yr^{-1}) [57]. Furthermore, deseasonalized monthly average data show that GoM open ocean air-sea CO_2 fluxes are decreasing over time, suggesting that the open ocean may be transitioning towards a sink for atmospheric CO_2 (Fig. A-9). The establishment of a GoM open ocean time series station that includes carbonate chemistry measurements is needed to elucidate long-term ocean acidification trends with better certainty and to understand how this global phenomenon will impact the health of GoM coral reefs and fisheries.

The annual increase in coastal pCO_2 is 4.0±1.0 μatm yr^{-1}, which is almost 4 times faster than the open ocean acidification signal (Fig. 2.4), and similar to long-term CO_2 trends measured in coral reefs and the southeastern U.S. coastal margin (Cyronak et al. 2014; Reimer et al. 2017). Many of the pCO_2 values lie above the Mauna Loa observations, which suggests that rising atmospheric CO_2 is not the sole driver of the coastal acidification signal. The deseasonalized coastal temperature trend reveals a 3.8 °C increase over 21 years (0.18±0.06 °C yr^{-1}, R^2=0.1, p=0.003). This increase in coastal temperature can account for a pCO_2 increase of ~54 μatm, which is ~65% of the total coastal ocean pCO_2 increase (Pierrot et al. 2006). The remaining 35% (~30 μatm) is approximately equal to the overall pCO_2 increase in the open ocean GoM, which does not see a warming trend, and is therefore likely due to absorption of atmospheric CO_2.

However, an increase in net respiration, potentially driven by inputs of terrestrial-derived organic matter, cannot be ruled out and should be further explored in future studies.

CHAPTER III

LOCALIZED HYPOXIA DRIVES CORAL REEF MORTALITY AT THE FLOWER GARDEN BANKS

Introduction

Approximately 200 km off the Texas-Louisiana coast lies the Flower Garden Banks (FGB). The FGB includes three shallow banks: East Bank (EB), West Bank (WB), and Stetson Bank (SB). These banks are underwater mounds overlying salt domes at the edge of the continental shelf. The surrounding water is greater than 100 m deep, while the banks rise to as shallow as 17 m (Bright 1977). Coral reef communities grow on the banks and are a critical component of the Gulf Coast economy by providing habitat for Gulf of Mexico (GoM) fisheries and recreational diving for the tourism industry. The FGB coral reef ecosystems are particularly unique because they are geographically isolated and lie at the northern latitudinal limits for which environmental conditions are conducive to coral reef growth (Kleypas et al. 1999). Due to their remote offshore location, coastal associated stressors (e.g., eutrophication and sedimentation) have not been observed at the FGB. As such, the FGB are one of the healthiest coral reef ecosystems remaining in the Caribbean and GoM with coral cover persisting at >50% over the past 25 years, despite a dramatic global decline in coral reef health (Gardner et al. 2003; Pandolfi et al. 2003; Johnston et al. 2013b).

Extensive agricultural activity in the watersheds of GoM rivers results in freshwater plumes with high nutrient loads that enhance primary productivity and lead to low CO_2 in coastal surface waters (Huang et al. 2015a). This enhanced surface

productivity results in excess organic matter that is respired at depth, and combined with stratification, causes the depletion of dissolved oxygen (i.e., hypoxia), accumulation of CO_2, and decrease in pH (i.e., acidification) in bottom waters of the Texas-Louisiana Shelf (Bianchi et al. 2010; Cai et al. 2011). During periods of high river discharge and offshore flow, river-influenced waters (salinity <33), presumably from the Mississippi, Atchafalaya and Texas rivers, have been documented near the FGB as a thin, low salinity layer confined to the surface (Rezak et al. 1990). This is consistent with a weakly upwelling summertime circulation pattern established over the Texas-Louisiana shelf that tends to pull fresher coastal waters offshore (Cochrane and Kelly 1986; Cho et al. 1998; Nowlin et al. 2005). While Dodge and Lang (1983) found that coral growth at EB negatively correlated with the annual discharge of the Atchafalaya River, the impacts of freshwater on FGB ecosystem health remain a subject of debate. Deslarzes and Lugo-Fernández (2007) observed low salinity surface waters at the FGB but found low nutrient concentrations that could no longer induce phytoplankton blooms. Hu et al. (2018) have reported on seasonal changes in surface water (<25 m depth) carbonate chemistry in the FGB sanctuary and found that the biological effect on CO_2 is slightly greater than at the Bermuda Atlantic Time Series, but temperature is still the dominant driver of seasonal CO_2 variability.

While surface waters over the FGB can be influenced by riverine runoff, bottom waters on the banks may be influenced by deep water masses. Cool waters (~14°C) that originate at ~200 m depth have been recorded at <50 m depth at EB, indicating that upwelling can bring deep water onto the bank (Teague et al. 2013). The mechanisms for

upwelling have not been thoroughly investigated, but topographic upwelling at EB could be caused by propagating Kelvin waves, eddies or strong mixing events. Hydrographic casts conducted off the Texas-Louisiana Shelf indicate that water at 200 m has high DIC, (~2175 μmol kg^{-1}), low Ω_{ar}, (~2), and low dissolved oxygen (~3 ml L^{-1}) (Morrison et al. 1983; Nowlin Jr et al. 1998; Wang et al. 2013b; Wanninkhof et al. 2015; Georgian et al. 2016). Although the impacts of these waters on coral reef health are currently unknown, upwelling could lead to localized hypoxia and/or acidification.

Hypoxia in coral reefs is not well-documented, potentially because dead zones are primarily studied in temperate, rather than tropical regions (Diaz and Rosenberg 2008; Altieri et al. 2017). Die-offs are often discovered following the presumed hypoxic event, when water chemistry has returned to normal conditions. Furthermore, coral reef monitoring efforts do not systematically include the measurement of oxygen, which makes it difficult to pinpoint hypoxia-driven mortality. However, a few studies have reported mortality events in coral reefs and implicated hypoxia as the cause (Altieri et al. 2017; Baird et al. 2017; Gajdzik and DeCarlo 2017). These events usually occur following high sea surface temperatures, calm conditions and reduced circulation, and can be associated with coral bleaching. Despite the proximity of the FGB to the dead zone on the Louisiana continental shelf to the north, it is generally understood that the low oxygen conditions and processes that control that dead zone are typically in shallower water (< 60 m) to the east of the FGB and do not extend to the FGB (Bianchi et al. 2010).

On July 25, 2016, recreational divers at EB reported green, hazy water, dead invertebrates on the ocean floor and white mats covering corals and sponges. The FGB scientific team was notified and initiated an investigation into the health of the corals and the nature of the mortality event. Benthic surveys determined that mortality had spread over 6.5 acres on the EB southern coral cap, with some areas experiencing up to 70% mortality (Johnston 2018). Signs of mortality and stress (e.g., tissue sloughing and white mats) appeared in a distinct horizon within ~1 m of the bottom (Fig. 3.1). Organisms that form calcium carbonate shells were noted to crumble upon collection. While the impact of the mortality event was widespread on EB, the ecosystems of WB and SB were not visually impacted. Five days after the discovery of this die-off, we conducted a rapid response cruise to characterize surface and deep water masses within and around the FGB National Marine Sanctuary in order to uncover the mechanisms that led to the localized mortality event. We present here data on the hydrography, biogeochemistry, and microbiology in the water column within a week of initial reports of the mortality event and hypothesize on potential mechanisms causing the die-off.

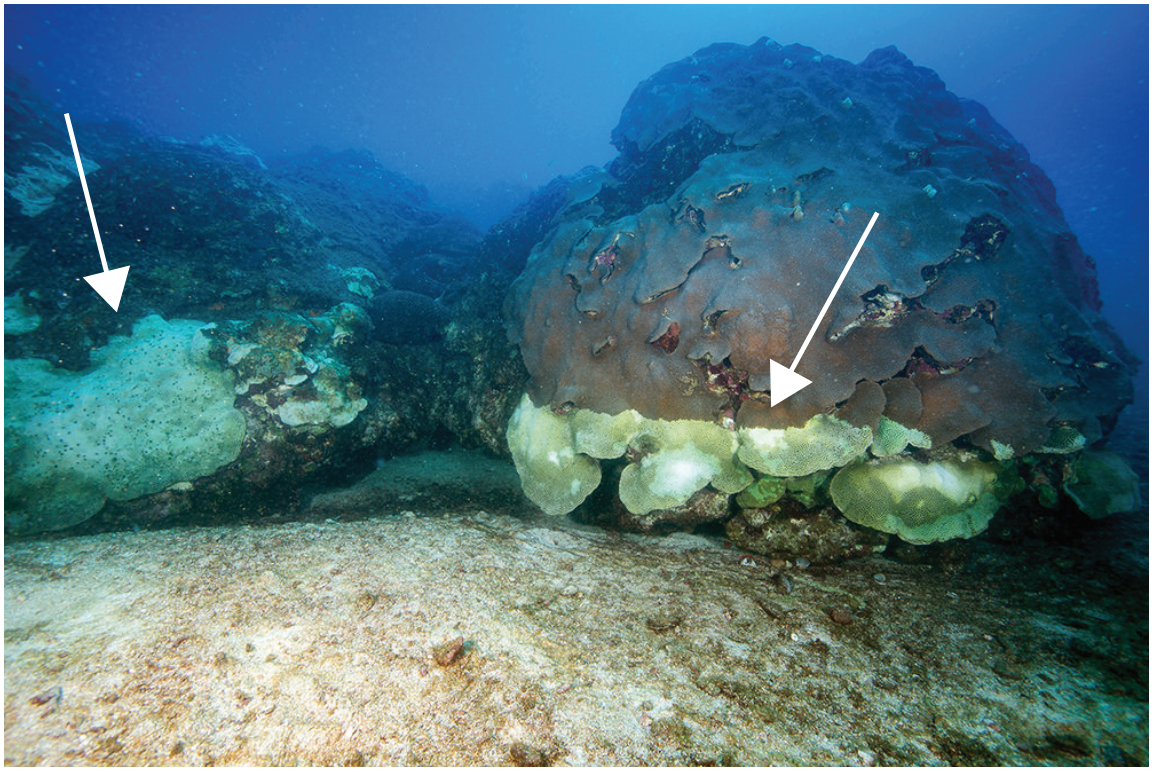

Figure III.1 Invertebrate mortality was observed within a ~1 m layer above the ocean floor and heavily localized in the EB (NOAA FGBNMS/Schmahl).

Materials and methods

Environmental setting

East Bank is approximately 5 km wide and 8 km in length. (Fig. 3.2). Approximately 20 km to the west lies the WB, which is 5 km wide and 11 km long. Gradual sloping occurs along the banks of WB, while the EB has a steeper topography on the south and east sides. Although long-term ecological and water quality monitoring is conducted across all three sanctuary banks, EB remains the most studied, particularly with respect to hydrography. Surface currents at EB are generally eastward throughout the year but can be reversed for short periods of days to weeks by westward propagating

eddies that originate from the Loop Current (Teague et al. 2013). At depth, currents flow to the south following the bathymetry of the bank, but can also be reversed. Sea surface temperature (SST) ranges from 17°C in the winter and may reach >31°C in the summer (Buoy V; http://tabs.gerg.tamu.edu). The mixed layer is deepest (~80 m) in Dec-Jan and can shoal to ~10 m during the remainder of the year (Teague et al. 2013).

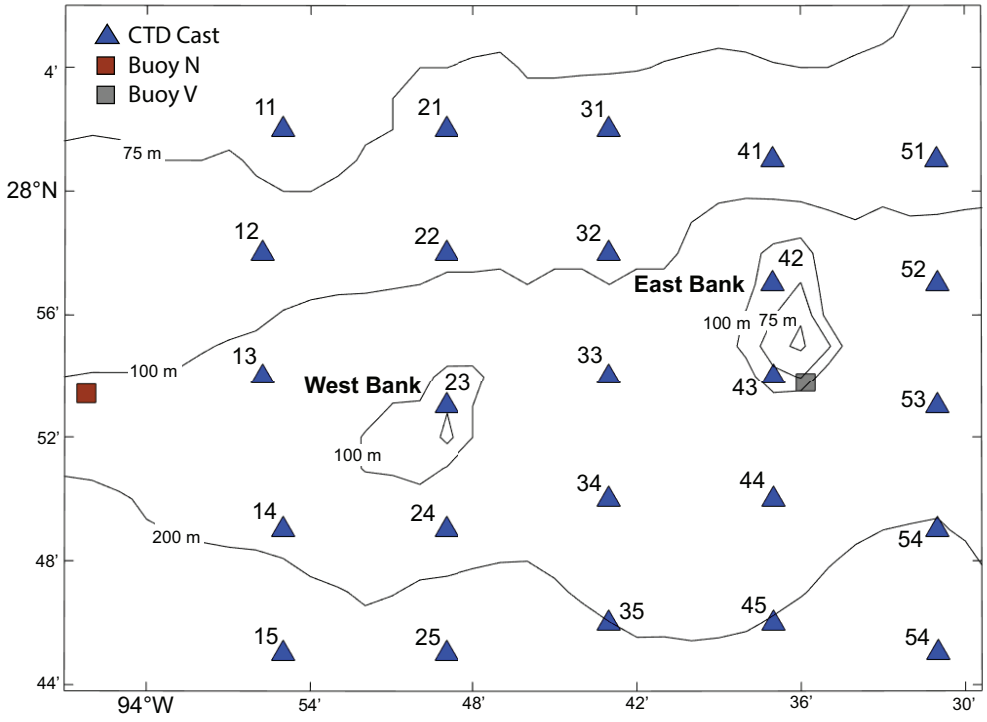

Figure III.2 Map of WB and EB and locations of CTD casts (blue triangles) labeled by station number during the rapid response cruise.

Sample collection

Discrete water samples for dissolved oxygen (DO), dissolved nutrients, salinity, TA, DIC, cell counts, and microbial community analyses were collected between July 30th and August 2nd 2016 aboard the R/V *Manta*. A total of 39 conductivity, temperature and depth (CTD) profile stations were performed in a 5x5 grid that encompassed the East and West banks (Fig. 3.2). Seawater samples were collected using a Niskin bottle rosette on a Seabird Electronic (SBE) 25 CTD profiler.

Chemical analyses

Discrete water samples for TA and DIC were collected using borosilicate 250 ml glass bottles, poisoned with 100 µl of saturated mercuric chloride, and sealed with Apiezon grease (Dickson et al. 2007). Samples were analyzed at Texas A&M University (TAMU) using a Versatile INstrument for the Determination of Total inorganic carbon and titration Alkalinity (VINDTA) produced by Marianda Marine Analytics and Data. Certified Reference Materials (CRMs) were provided by A. Dickson at Scripps Institute of Oceanography (Dickson et al. 2007) and were used to calibrate for TA and DIC. The reproducibility of these samples was 1.43 ± 1.07 µmol kg^{-1} for TA and 2.64 ± 1.24 µmol kg^{-1} for DIC. CO_2 fugacity (fCO_2), Ω_{ar}, and the remaining parameters of the carbonate system were calculated using CO2SYS (Pierrot et al. 2006) and the equilibrium constants of Mehrbach et al. (1973) refit on the seawater pH scale by Dickson and Millero (1987).

Dissolved oxygen was measured using Winkler titrations (WHP 1994). After collecting the water from the Niskin into flasks, aliquots of manganese chloride and

sodium hydroxide-sodium iodide were added. The titration was performed directly after water collection using sodium thiosulfate; Winkler titration was performed with an amperometric dead-stop endpoint determination with a double platinum electrode. Nutrient samples (nitrate, nitrite, ammonium, phosphate and silicate) were collected into polycarbonate flasks after filtration through GF/C 0.7µm filters, frozen, and analyzed ashore using standard World Ocean Circulation Experiment (WOCE) segmented flow methodologies using an Astoria Analyzer (Astoria-Pacific) (WHP 1994).

Cell counts

Cell count samples (10 ml) were fixed with formalin (final concentration 2%) and stored at 4°C until analysis. Direct cell counts were performed with an epifluorescence microscope (Zeiss Axio Imager.M2) after staining the fixed samples with DAPI (45µM final concentration) for 5 minutes in the dark and filtering them onto 25 mm, 0.2 µm black polycarbonate filters. Each filter was mounted on a glass microscope slide with coverslip using two drops of Citifluor AF1 anti-fade solution. A 100 µm×100 µm ocular counting grid was used at 1000× magnification for cell counts.

Microbial sampling and DNA extractions

For each sample, 1 L of seawater was vacuum filtered (≤ 20 cm Hg) through a 47 mm, 0.22 µm Supor PES filter membrane (Pall) and immediately stored on the ship at -20°C. After returning to port, samples were transported on dry ice to TAMU and stored at -80°C until DNA extraction. Total DNA was extracted from filters using FastDNA Spin kits (MP Biomedical) and stored at -20°C until PCR amplification.

16S rRNA gene sequencing and analysis

The hyper-variable V4 region of the 16S rRNA gene was PCR amplified from the DNA extracts in triplicate with GoTaq Flexi DNA Polymerase (Promega) as described previously (Doyle et al. 2018). Amplicon libraries were sequenced at the Georgia Genomics Facility (Athens, GA, USA) using Illumina MiSeq sequencing (v2 chemistry, 250bp paired-end reads). Paired-end reads were processed using MOTHUR v.1.39.5 (See Appendix C, Supplementary Methods).

Patterns in microbial community structure were visualized with non-metric multidimensional scaling (NMDS) ordination of Bray-Curtis dissimilarity distances (Bray and Curtis 1957) and tested for significance using AMOVA (analysis of molecular variance). Dirichlet multinomial mixtures (DMM) modelling (Holmes et al. 2012) was used to assign samples into clusters (metacommunities). The number of metacommunities was determined from the number of components that gave the minimum Laplace approximation. Linear discriminant effect size (LEfSe) analysis was used to identify differentially abundant OTUs between sample groups identified via NMDS ordination or DMM modeling. Constrained correspondence analysis was used to identify environmental variables which significantly shaped the microbial communities following a strategy similar to the one described in Parada and Fuhrman (2017) (Supplementary Methods). Paired Spearman correlation analysis was performed using the rcor.test function in the "ltm" R package to identify OTUs correlated with low dissolved oxygen in near-bottom waters. Only correlations with Spearman's rho values > 0.60, P-values <0.005, and q-values (false discovery rate) <0.05 were considered.

Physical modeling

We used the TXLA regional hydrodynamic model (Zhang et al. 2012a) to estimate the ratio of Mississippi/Atchafalaya river water to Texas rivers' water in surface waters across the northern GoM. The TXLA model includes numerical dyes to trace Mississippi, Atchafalaya, and Brazos river discharge (Zhang et al. 2012b). The Brazos River is located in the region where rivers had elevated discharge in 2016, and roughly tracks the total discharge of Texas rivers (Fig. 3.3, left panel). As such, we used the Brazos river as a proxy for all Texas rivers combined by multiplying the Brazos discharge by 3.5 which is the mean ratio of the sum of all Texas rivers to the Brazos discharge during spring and early summer (Fig. 3.3, left panel).

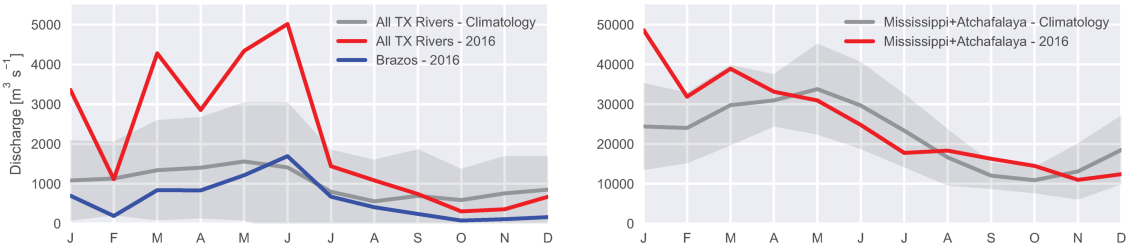

Figure III.3 The left panel shows the sum of all major Texas rivers (the Guadalupe at Victoria, Colorado at Wharton, Brazos at Rosharon, San Jacinto at Conroe, Trinity at Goodrich, Sabine at Ruliff, Neches at Evadale, Lavaca at Edna, San Antonio at Goliad, Nueces at Mathis, Aransas at Skidmore, and Mission at Refugio) for 2016 (red), and climatology based on the entire record for each river gauge (grey with SD shaded). The Brazos 2016 discharge is shown in blue. The right panel shows the Mississippi and Atchafalaya discharge for 2016 (red) and climatology (grey with SD shaded).

Results

River water influence

When compared to the climatological mean, Texas rivers' discharge was unusually high in summer 2016, particularly from March to June (Fig. 3.3, left panel). This increased discharge was focused primarily in the northern Trinity, San Jacinto, and Brazos rivers. During this same period, the Mississippi/Atchafalaya River discharge was well within the envelope of historical variability (Fig. 3.3, right panel). Despite the unusually high Texas rivers' discharge at this time, the Mississippi/Atchafalaya discharge was still 5-10 times larger than the total Texas rivers' discharge from March to June, and much more than 10 times larger outside of this time period. Numerical dye tracing with the TXLA model revealed the estimated ratio of Mississippi/Atchafalaya River water to the Texas river proxy at the ocean surface across the northern GoM (Fig. 3.4). Most of the modeled domain is influenced more strongly by the Mississippi/Atchafalaya waters, as expected based on the relative magnitude of the Mississippi/Atchafalaya discharge to total Texas river discharge. However, the western half of the domain shows that there is a small but significant influence of Texas rivers, particularly in July through September, when these rivers supplied approximately one fifth of the total river water that made it to the FGB (Figs. 3.4 and A-10). These numerical experiments are consistent with measured stable isotopes ratio, which show Texas river influence in the localized region of the Texas coast (DiMarco et al. 2012).

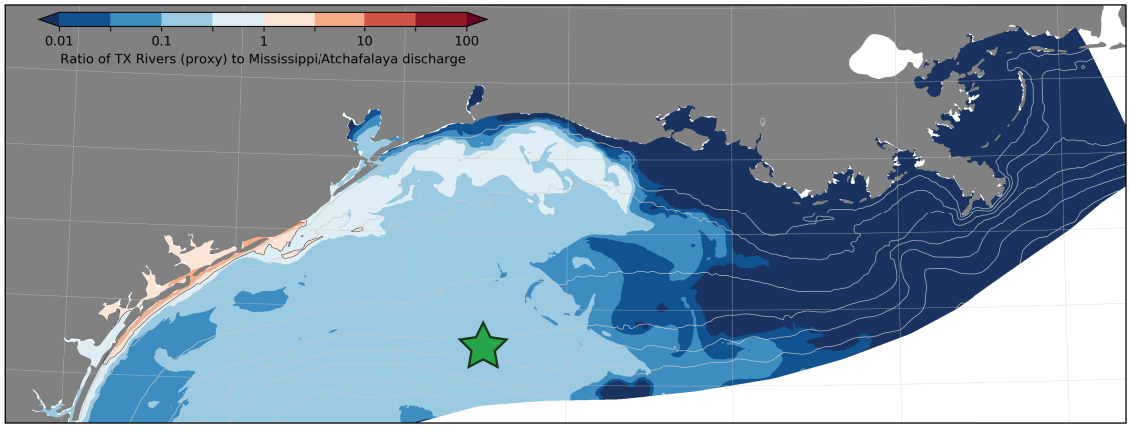

Figure III.4 The ratio of Mississippi and Atchafalaya water to a proxy for Texas river discharge (Brazos discharge times 3.5, see text for details) based on a numerical dye study is shown for July 23, 2016. The region of the FGB is marked with an orange circle, and bathymetry (10, 20, 50, 100, 200, 500, and 1000 m) is shown in contours. Red colors indicate a higher ratio of Texas river water, blue colors indicate more Mississippi/Atchafalaya water, so that, e.g., a value of 0.1 indicates ten times more Mississippi/Atchafalaya water than Texas river water at the ocean surface at the location this value is found.

Surface water chemistry

SSTs (≤10 m depth) during the rapid response cruise ranged from 29.9-31.9°C (mean±SD; 30.6±0.6°C), and were up to 2°C warmer on the east than on the west side of the sampling grid (Fig. A-11). Mean SSTs at Buoy V (located near the EB) and Buoy N (located near the WB) in July 2016 were comparable (30.6±0.3°C; maximum SST at Buoy V=32.2°C and maximum SST at Buoy N= 31.8°C). The historical SST record at Buoy V indicates that July SSTs have steadily increased by 0.4°C yr^{-1} since 2011, and July 2016 was the warmest July on record between 2002 and 2016 (Fig. A-12).

A low salinity layer was observed confined to the top ~10 m of the water column over EB (Fig. A-13). Across the grid, surface salinity ranged from 31.36-35.05

(mean=33.76±1.45) (Fig. 3.5, left panel). Similar to SST, an east-west gradient was observed with lower salinity in the east and higher salinity in the west. Buoy N was the first to record the presence of river-derived water (salinity<33) on June 21, 2016, followed by Buoy V a week later. Sea surface salinity decreased to <30 for more than a week beginning near June 25, 2017, with a minimum salinity of ~27.5 recorded at Buoy N (Fig. A-14).

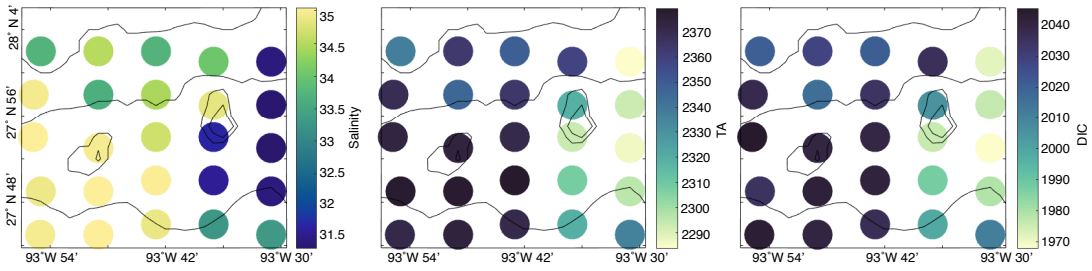

Figure III.5 Spatial distribution of near-surface observations of salinity (left panel), total alkalinity (TA, middle panel) and dissolved inorganic carbon (DIC, right panel).

Surface seawater TA (Fig. 3.5, middle panel) and DIC (Fig. 3.5, right panel) ranged from 2284-2379 µmol kg^{-1} and 1968-2046 µmol kg^{-1}, respectively, with the lowest values measured in the two eastern transects (stations 40-45 and 50-55). There were weak east-west gradients in surface Ω_{ar}, fCO_2 and oxygen; surface Ω_{ar} (range=3.69-4.02) was slightly lower over EB (3.69) than WB (3.91), and mean surface fCO_2 (range=410-475 µatm) was approximately 34 µatm lower over the eastern transects than over the western transects. There were no obvious east-west gradients in most surface

water nutrients, except ammonium (range=0.6-50.7 μM, mean=13.3±21.1 μM), which is higher over the eastern stations (Fig. A-15).

Deep water chemistry

At 75 m depth, north-south and/or east-west gradients in temperature, salinity, density and the carbonate parameters were apparent. At the northern and eastern stations, potential density (σ_θ) (Fig. 3.6a), salinity and DIC were higher, and Ω_{ar} (Fig. 3.6c) and temperature were lower than in surrounding waters at the same depth. A closer look at vertical contours of σ_θ (Fig. 3.6b) and Ω_{ar} (Fig. 3.6d) show that the isolines associated with these parameters at 75 m depth are deeper offshore (e.g., at station 35) and shallower onshore (e.g., at station 31). Additionally, there were north-south gradients in oxygen at 75 m, with oxygen generally being slightly lower onshore (by <1 ml L^{-1}, Fig. A-16), and ammonium concentrations were on average 8.8 μmol L^{-1} higher at the eastern stations at 75 m (Fig. A-17).

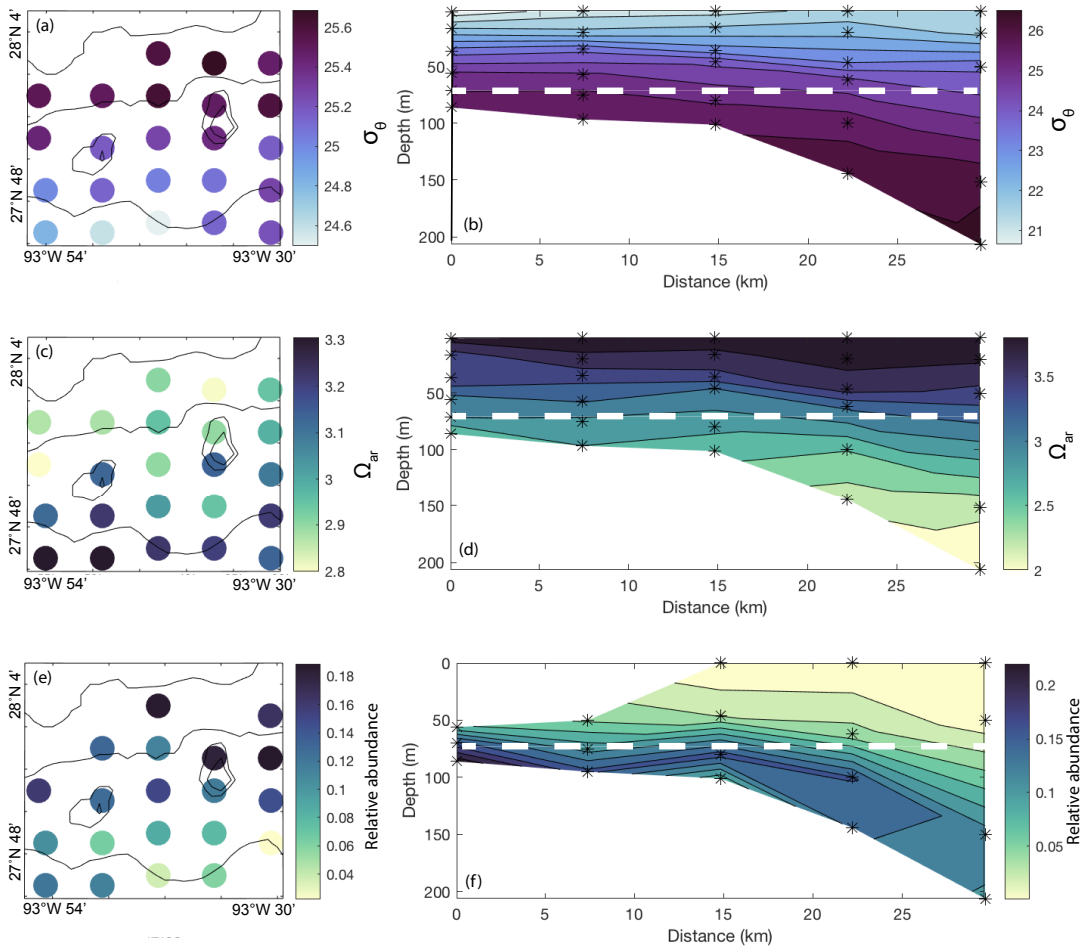

Figure III.6 Potential density (a), aragonite (c) and abundance of deep water taxa (e) at 75 m depth. Vertical contours of potential density (b), aragonite (d) and abundance of deep water taxa (f) at stations 31-35, where distance (km) is calculated from the furthest onshore station (i.e., 31). The white dotted line indicates the location of 75 m. Black asterisks (*) denote the location of discrete samples.

Microbial community composition and structure

DMM modelling of the 16S rRNA gene libraries partitioned the samples into three metacommunities (Fig. A-18b). AMOVA of Bray-Curtis dissimilarity confirmed these three clusters to be statistically significant groupings [$F(2,75)=58.5$, $p<.001$]. NMDS ordination suggested water depth was the primary environmental parameter which differentiated the three metacommunities (Fig. 3.7). This was confirmed by a constrained correspondence analysis, which indicated water depth explained 39.5% ($p=.001$, $q=.002$) of the total prokaryotic community variation, the highest of any variable in the final model (Table B-1). The first metacommunity partition comprised samples from a median depth of 0 m (interquartile range (IQR) = 0-30 m), the second from a median depth of 61 m (IQR = 50-70m), and the third from a median depth of 100 m (IQR = 87-146 m; Fig. 3.8c). Hence, for simplicity we named the three metacommunities Shallow, Mid-Depths, and Deep, respectively. Microbial diversity and richness were lowest and least variable in the Shallow metacommunity, and highest and most variable in the Deep metacommunity (Fig. A-18a). Average microbial cell abundances (Fig. A-18c) were very similar in the Shallow and Mid-Depths samples ($2.6 \pm 1.1 \times 10^6$ cells $mL^{-1;}$ $M \pm S.E.$) and slightly lower in the Deep samples ($1.5 \pm 0.9 \times 10^6$ cells mL^{-1}).

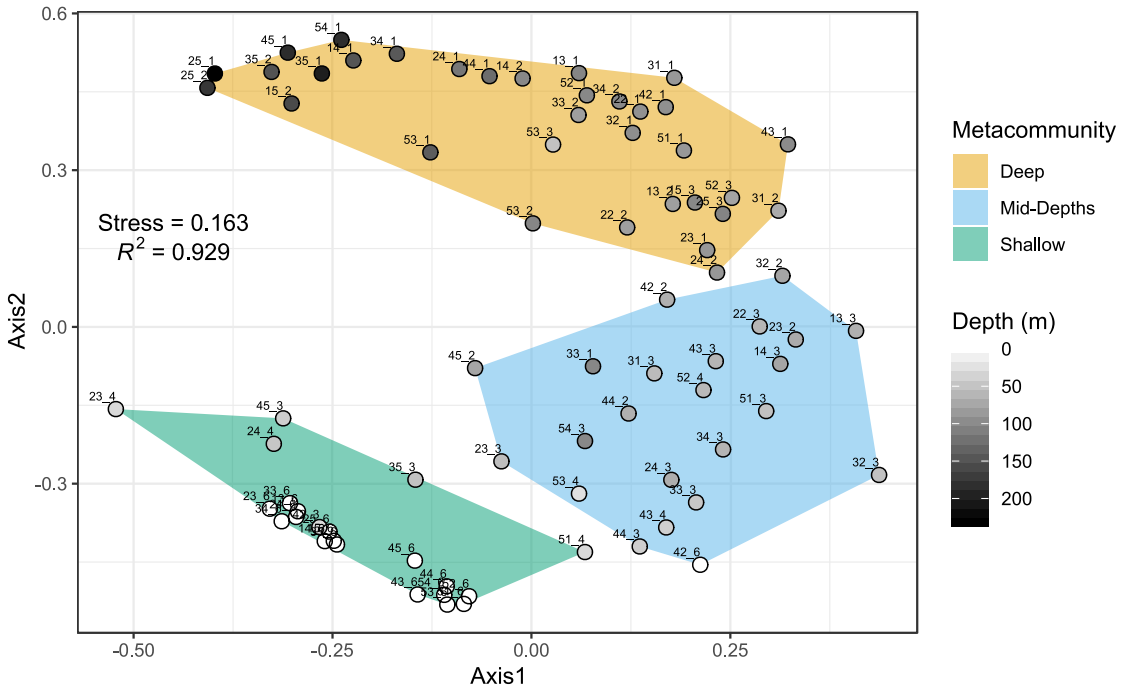

Figure III.7 NMDS ordination plot of Bray-Curtis dissimilarity between 78 water samples taken from the FGB. Each circle represents a water sample. The distance between circles represents the similarity of those samples' respective microbial communities based on OTU richness and abundance. Samples with similar microbial communities are closer together while those with more dissimilar microbial communities are farther apart. Each circle is shaded according to depth and grouped by metacommunity.

The microbial community composition of each metacommunity is summarized in Fig. 3.8a. The individual OTUs most indicative of each metacommunity, identified through LEfSe analysis, are shown in Fig. A-19. The Shallow metacommunity samples contained primarily bacteria (~99% of total community) from the orders *Cyanobacteria* subsection I, *Pelagibacterales* (formerly SAR11), *Oceanospirillales*, *Rhodospirillales*, *Acidimicrobiales*, *Flavobacteriales*, and *Rickettsiales*. Within the Mid-Depths samples, the relative abundance of bacteria decreased to ~90%, mostly due to lower cyanobacterial abundances and an increase in relative abundance of the archaeal lineages

Thaumarchaeota Marine Group I (MGI) and *Thermoplasmatales*. The Deltaproteobacteria SAR324 clade also displayed increased abundance in these samples. The Deep metacommunity samples contained the largest relative abundances of archaea (~24% of the total community) as *Cyanobacteria* became increasingly rare with depth. Compared to the Shallow and Mid-Depths samples, the Deep samples were primarily represented by *Thaumarchaeota* MGI, SAR324, *Thermoplasmatales*, and *Marinimicrobia* (Fig. 3.8b).

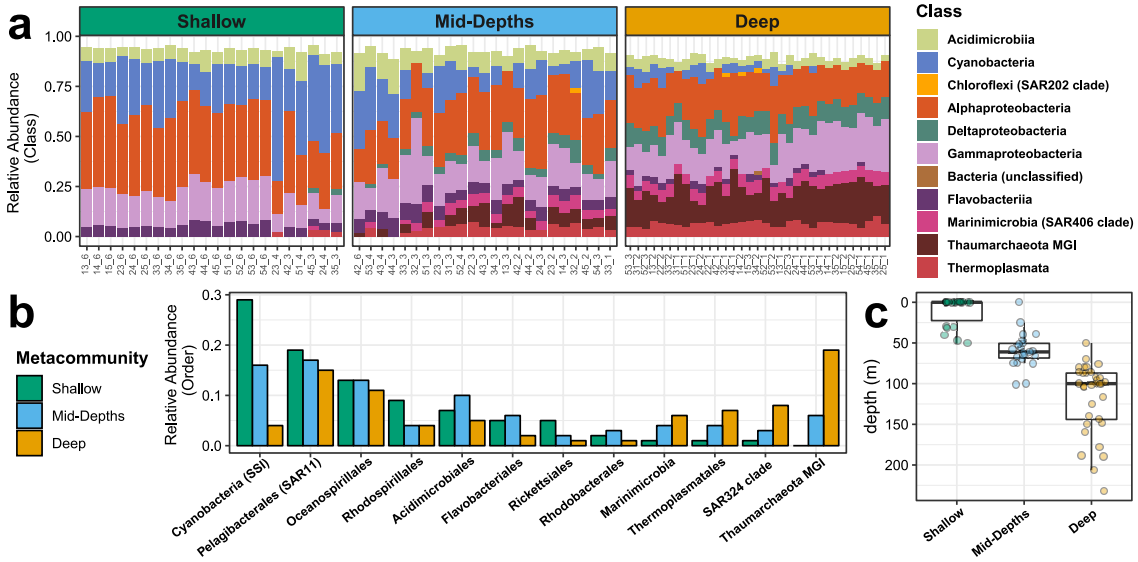

Figure III.8 (a) Relative abundances of the microbial lineages (Class) observed in the three metacommunities. Taxa with relative abundances less than 2% were excluded for clarity. Each bar represents a water sample (N=78). All samples are arranged by depth within each metacommunity, with the deepest samples located to the right. (b) Relative abundances of the twelve most abundant Orders within each metacommunity. (c) Boxplots of the sample depth distribution within each metacommunity.

The shallow metacommunity contained two significantly distinct clusters [$F(1,15)=35.8$, $p<.001$] of surface samples in the NMDS ordination (Fig. 3.7). The samples forming these two clusters were located from the EB and WB, respectively. Variations in microbial community structure between these two clusters was explained predominantly by salinity ($F(1,13)=8.204$, $R^2=0.387$, $p=.001$). Average surface salinities were significantly lower ($t(13)=13.1$, $p < 10^{-8}$) in samples from the eastern cluster (31.8‰ ± 0.68‰) compared to the western cluster (35.0‰ ± 0.12‰). LEfSe analysis revealed that EB surface waters were enriched with *Synechococcus* and SAR86 related OTUs, while the higher salinity WB surface waters instead harbored larger abundances of *Prochlorococcus*, *Pelagibacter*, and SAR116 (Fig. A-20).

Paired Spearman correlation analysis was used on bottom water samples from all stations to identify OTUs, which were correlated with low DO concentrations. We found 14 OTUs from five taxonomic classes were strongly correlated (Spearman's rho >0.6) with low DO concentrations in bottom waters samples. Seven of these OTUs were members of the same lineage—Marine Group I (MGI) *Thaumarchaeota*. The remaining 6 OTUs included 2 members of the *Marinimicrobia* (formerly known as SAR406), and 1 member each of the *Acidimicrobiales* marine group Sva0996, *Deltaproteobacteria* clade SAR324, *Gammaproteobacteria* clade SAR86, *Salinisphaeraceae* marine group ZD0417, and *Gammaproteobacteria* marine group E01-9C-26.

Discussion

The objective of this study is to resolve the mechanisms that led to the development of the 2016 FGB localized morality event. The chemical, microbial and

physical data reveal the presence of low-salinity waters at the surface and a deep water mass surrounding EB at ~75 m depth. We hypothesize that the combination of these two water masses provided a physical environment that favored rapid development of hypoxia that was centralized at EB.

River-derived water in the FGB

Low surface seawater TA, DIC and salinity are clear evidence for river-derived water, which was only present within the eastern part of the grid and over EB during our sampling cruise (Figs. 3.5, A-13 and A-15). During periods of high river flow, the weathering signal of dissolved continental rock, which contains high loads of carbonate material, is diluted, causing this water to have low TA and DIC (Cai 2003a). DIC is further reduced in coastal waters due to photosynthetic uptake of CO_2 that is supported by the high nutrient concentrations of the Mississippi River (Lohrenz et al. 1997). Salinity, TA, DIC and CO_2 increase as this water mixes with open ocean water in transit to the shelf break.

Low salinity was first measured by Buoy N in mid-June 2016 and persisted for over one month. The 2016 discharge from the Mississippi/Atchafalaya rivers was highest from January through May while discharge from Texas rivers was highest in March through June, indicating that it takes several months for river water to be advected to the FGB. Buoy N measured low salinities before Buoy V, suggesting that the freshwater plume migrated over the banks from the west (Fig. A-14). This is consistent with the freshwater plume moving offshore under the influence of upwelling favorable winds, but does not necessarily indicate a Texas River source as the

Mississippi-Atchafalaya plume typically extends far down the Texas coast during winter (Zhang et al. 2012b). This observation is also supported by regional wind data that show strong southerly winds during the 2016 summer (Fig. A-21). Strong, southerly winds enhance upwelling along the Texas coast, and are associated with a stronger northward coastal jet, though still confined to approximately the inner half of the shelf (Zhang and Hetland 2012). Further offshore, stronger southerly winds can enhance Ekman transport to the east, but this feature is likely to be much weaker than the mesoscale activity observed along the edge of the continental shelf in the vicinity of the FGB.

The increased abundance of the cyanobacterial genus *Synechococcus* in the low salinity waters over the EB in concert with elevated ammonium concentrations corroborate a freshwater source for the surface water anomalies; *Synechococcus* generally dominate in coastal and more mesotrophic open ocean waters, while *Prochlorococcus* are usually more abundant in oligotrophic waters (Partensky et al. 1999; Zwirglmaier et al. 2008).

Upwelling of dense water over East Bank

Upwelling is more likely to occur at EB than WB for two reasons: (1) eddies propagate over the FGB from the east and, (2) the southeast of EB has steeper seafloor topography than WB. We observed higher water density, DIC, ammonium concentrations, and salinity concurrently with lower temperature and Ω_{ar} at 75 m at the northern and easternmost stations, which implies a deeper source water at these stations (Fig. 3.6). We observed that the combined relative abundances of OTU5 (*Nitrosopelagicus*), OTU6 (uncultured marine bacterium ZD0405), and OTU9 (SAR324

clade) were highest in shallower stations in the northeast quadrant of our sampling grid, near EB (Fig. 3.6 e, f). These three OTUs are the strongest indicator taxa of the Deep metacommunity (Fig. A-19) and their unexpectedly high relative abundance in these shallower stations implies that deep water upwelling may have occurred in this area (Fig. A-22 and Fig. 3.6e, f).

Analysis of observed stratification and associated geostrophic shear also revealed evidence for upwelling at EB, likely due to deep GoM forcing. Calculated Richardson numbers were much less than 10 at a number of stations, even dropping to about 1.5 for many, indicating unstable stratified shear flow and the potential for vertical mixing (e.g., Pacanowski and Philander 1981). Additionally, the slope of the isopycnals is high, up to about 0.1, roughly two orders of magnitude steeper than the bottom slope (≈ 0.001 over the continental slope) and three orders of magnitude steeper than the bathymetric slopes over the shelf (typically about 0.0001 over the shelf). All of these lines of evidence point to upwelling associated with energetic, along-slope flow. However, because upwelling events at EB only last for a few days, it is possible that we missed the strongest signals associated with this process (Teague et al. 2013). The spatial distribution of chemical properties indicative of upwelling was variable, but a comparison to previous hydrographic studies in the GoM suggests the upwelled water originated from depths of approximately 100-200 m (Morrison et al. 1983; Georgian et al. 2016).

Localized hypoxia over East Bank

Coral reefs are highly productive ecosystems, with very high photosynthesis and respiration rates that are often close to balanced. Nonetheless, net ecosystem production

(NEP; photosynthesis- respiration) rates can range from as low as -60 mmol C m^{-2} h^{-1} (net respiration) to as high as 150 mmol C m^{-2} h^{-1} (net photosynthesis) (Gattuso et al. 1996; Shamberger et al. 2011; Falter et al. 2012; DeCarlo et al. 2017). With a hazy surface layer to block sunlight and potentially reduce photosynthetic rates, the benthic ecosystem could quickly become net respiring even during daylight hours. Respiration of reef organic matter that consumes O_2 and produces CO_2, coupled with upwelling of dense, oxygen-deficient, lower pH waters and bottom water stratification to prevent re-oxygenation, could rapidly result in localized hypoxia on the reef. Hypoxia would also elevate CO_2 and lower pH and Ω_{ar} to levels beyond those typically observed on coral reefs. Although we did not measure hypoxia—probably because the chemical signal was mixed out by the time we arrived at the FGB, or because the Niskin bottles were always at least a few meters above bottom—many of the microbial taxa sampled at EB are members of taxa commonly associated with oxygen minimum zones. The majority of these OTUs classified as MGI *Thaumarchaeota*, a clade of ammonia-oxidizing archaea which thrive in hypoxic conditions and have been implicated in maintaining sustained oxygen drawdown in environments with low DO (Stewart et al. 2012; Tolar et al. 2013; Gillies et al. 2015). In this study, the largest relative abundance of this lineage was observed in the deepest sample taken at station 43, near the EB coral cap.

W calculated the time it would take for the EB bottom water layer to reach hypoxia using the equation:

$$Residence\ Time = \frac{1.05*(O_{2i}-O_{2f})*d}{NEP} \quad (3.1)$$

where 1.05 mol O_2/mol CO_2 is the photosynthetic quotient (Smith and Marsh 1973), O_{2i} (195.51 mmol O_2 m^{-3}) is the initial concentration of oxygen we measured on the reef cap during the rapid response cruise, O_{2f} is the oxygen concentration on the reef if these waters were hypoxic (62.53 mmol O_2 m^{-3}), d is the depth (1 m) of the hypoxic bottom water layer and NEP (-400 mmol C m^{-2} d^{-1}) is the maximum -NEP observed on other reefs (e.g., maximum net respiration) (Shamberger et al. 2011). A depth of 1 m was chosen because dead coral tissue and the white mats covering coral heads and sponges extended about a meter off the bottom (Fig. 3.1). Given these conditions, minimum movement of bottom water, and a strongly stratified bottom layer preventing re-oxygenation, hypoxia could have occurred within 8 hrs. Even with a conservative estimate of -NEP (e.g., -200 mmol C m^{-2} d^{-1}) and increasing the bottom stratified layer to 2 m, these waters could have gone hypoxic within 36 hrs. We acknowledge this is a rough estimate; however, it does provide a minimum time for the onset of hypoxia.

Hypoxia of the Louisiana Shelf is typically considered to be inshore of the 60 m isobath (Bianchi et al. 2010; Dale et al. 2010) with peak frequencies of occurrence east of 93ºW (Rabalais et al. 2007). Investigation of cross-shelf variability of stratification, chlorophyll, and DO concentration during 2003-2014 confirms that low oxygen water masses emanating from stratified near shore locations will encounter oxygen rich water masses of the continental shelf and ventilate within 10-20 km (Zhang et al. 2015; DiMarco and Zimmerle 2017). We therefore consider the probability of a near-shore low oxygen water mass advecting more than 100 km offshore intact and impinging on the FGB as unlikely.

We present a conceptual diagram for the formation of localized hypoxia on EB in Fig. 3.9. A fresh, hazy, surface water plume migrated over the EB from the west. This layer blocked sunlight, which reduced photosynthesis and increased net respiration of coral reef organic matter. An intrusion of dense, deep water migrated onto the bank, settled in pockets on the reef, and created a stratified bottom layer. Within these pockets, oxygen declined due to the combined influences of enhanced net respiration and stratification. Whether respiration of organic matter alone was enough to drive hypoxia, or hypoxia was aided by the low oxygen concentration of the deep water intrusion, is unclear. However, our residence time calculation suggests hypoxia could occur in less than a day with normal, initial oxygen concentrations on the reef.

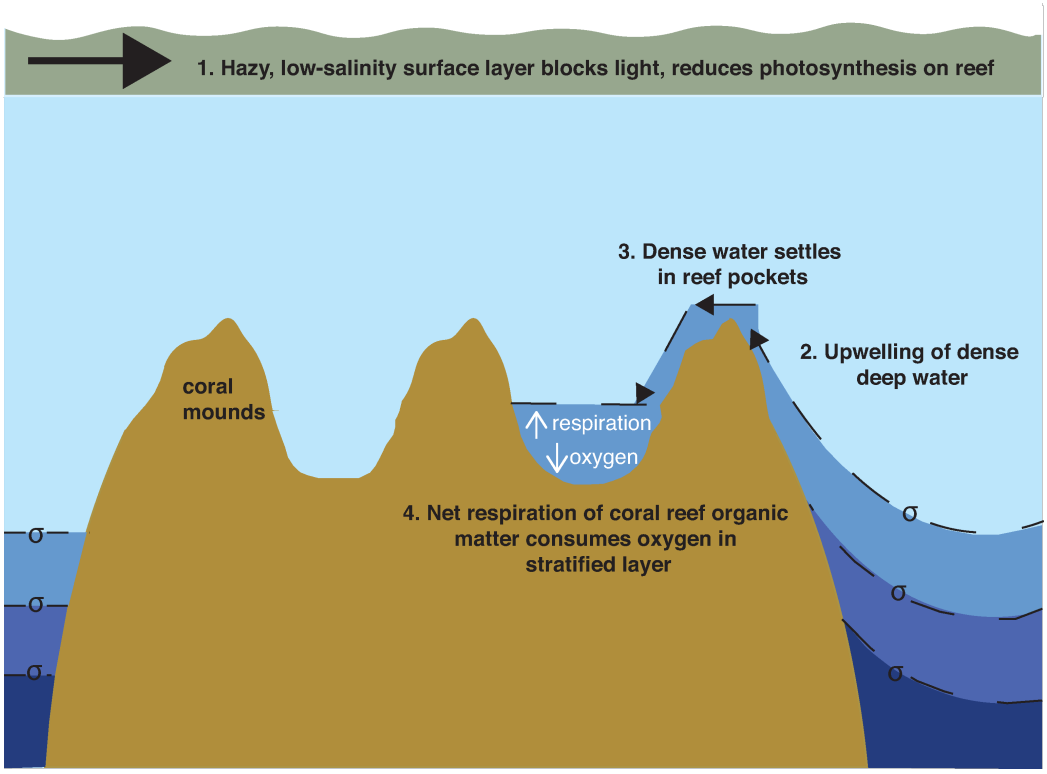

Figure III.9 Conceptual diagram illustrating the formation of hypoxia on the EB.

The largest FGB coral bleaching event ever recorded occurred in October 2016, approximately 10 weeks after the mortality event. Although a direct connection between these two events has not been established, hypoxic stress is known to increase the susceptibility of corals to bleaching (Baohua et al. 2014; Altieri et al. 2017). Furthermore, bleaching was almost two times as high in some areas of EB than at WB where no mortality event was observed and upwelling is less likely. Widespread coral reef bleaching events are expected to become more common in the future as global SSTs rise (Hoegh-Guldberg et al. 2007). Between 2011 and 2016, July SSTs at Buoy V increased at a rate of 0.4 °C yr^{-1}, and mean July temperatures crossed the 30°C bleaching

threshold in 2015 (Hagman and Gittings 1992) (Fig. A-12). If this trend continues, FGB corals will be annually exposed to temperatures beyond their bleaching thresholds. How FGB corals respond to isolated upwelling events that bathe these reefs with low DO, Ω_{ar}, and pH water has yet to be investigated. However, coupled with a turbid low salinity surface layer and increasing SSTs, mortality events such as the July 2016 event described here are likely to occur in the future. Management strategies should account for threats to coral reef resilience associated with freshwater discharge (e.g., low salinity, eutrophication, hypoxia) and upwelling (e.g., acidification and hypoxia) by increasing detection efforts with autonomous, high-resolution monitoring systems, which must include the measurement of oxygen.

CHAPTER IV

HETEROTROPHY OF OCEANIC PARTICULATE ORGANIC MATTER ELEVATES NET ECOSYSTEM CALCIFICATION

Introduction

Coral reefs support the health and livelihoods of millions of people worldwide by providing food, coastal protection, cultural sustenance and economic revenue (Moberg and Folke 1999). In order to maintain their structure and persist over time, coral reefs must produce more calcium carbonate ($CaCO_3$) than is lost through destructive processes. NEC is an important measure of coral reef health that provides an estimation of net $CaCO_3$ production at the ecosystem scale. Climate-related perturbations (e.g., ocean acidification and warming) threaten the delicate balance between calcification and dissolution, and considerable attention has been given to identifying the suite of environmental factors important for maintaining positive NEC. Relationships between NEC and net ecosystem production (NEP: production - respiration), Ω_{ar}, light, temperature, dissolved nutrient concentration, coral cover and water flow have been documented in previous studies (e.g. Langdon and Atkinson 2005; Silverman et al. 2009; Shamberger et al. 2011; Comeau et al. 2014; DeCarlo et al. 2017), but the strength and slopes of these correlations varies between reef systems. Even when coral reefs experience conditions unfavorable for growth, NEC can be positive (e.g., Shamberger et al. 2018) which suggests that we have not fully constrained the range of factors that influence calcification.

Corals receive energy to meet their metabolic demands in two ways. The first, and primarily, is through their symbiotic relationship with dinoflagellates, which can provide corals with up to 100% of their daily metabolic needs via photosynthesis (Muscatine et al. 1981). The second is through heterotrophy, which is also an important source of nutrients (e.g., phosphorous and nitrogen), and can contribute up to 66% of the fixed carbon incorporated into coral skeletons (Houlbrèque and Ferrier-Pagès 2009). The interactive effects of heterotrophy and light, acidification, and temperature on coral calcification have been explored primarily in laboratory settings. The calcification rates of *Stylophora pistillata* increased by 30% under feeding enhancement, and fed corals maintained growth rates under low light (Ferrier-Pagès et al. 2003). With the addition of particulate nutrients, both juvenile corals (Drenkard et al. 2013) and massive *Porites* (Edmunds 2011) sustained high rates of calcification under elevated seawater CO_2. While heterotrophy can account for up to 35% of daily metabolic requirements in healthy corals, some bleached corals can receive up to 100% of daily metabolic requirements from heterotrophy (Grottoli et al. 2006). Combined, these studies suggest some corals can allocate more energy to calcification through increased heterotrophic feeding, and that heterotrophy may allow corals to maintain calcification rates under some stressors.

Coral reefs live in oligotrophic environments and yet maintain some of the highest production rates of any ocean ecosystem (Sargent and Austin 1949; Odum and Odum 1955). Early studies suggested that particulate organic matter (POM) transported to the reef from offshore was an insignificant source of nutrients and high productivity

was therefore attributed to efficient, internal nutrient recycling (Johannes et al. 1972). More recently, however, it has become apparent that oceanic POM in small size fractions (< 5μm) is a significant external source of nutrients to coral reefs and that reefs actively consume this POM (Yahel et al. 1998; Wyatt et al. 2010, 2013; Patten et al. 2011). Taken together, laboratory and field studies suggest that coral reef consumption of oceanic POM may elevate NEC. In fact, Yeakel et al. (2015) hypothesized a connection between increased offshore productivity and enhanced calcification on a Bermuda coral reef, though the relationship between NEC and oceanic POM uptake has not been measured directly.

In this study, we utilized metabolically-induced changes in carbonate chemistry and POC to test for a correlation between NEC and oceanic POC uptake on the Kāneʻohe Bay barrier reef in Oʻahu, Hawaiʻi. Our data show a significant and positive correlation between oceanic POC consumption and NEC, suggesting that the documented decline in offshore productivity could have important implications for the ability of coral reefs to maintain net calcification (Behrenfeld et al. 2006; Polovina et al. 2008; Boyce et al. 2010).

Methods

Site description

Kāneʻohe Bay is located on the east side of Oʻahu, Hawaiʻi (Fig 4.1). The estuarine bay consists of numerous patch and fringing reefs and two channels located on the north and south of a barrier reef. Based on our analysis using Coral Point Count (Kohler and Gill 2006), coral cover on the barrier reef ranges between 0-10%, similar to

the estimate of 5-10% from (Jokiel 1991). The major coral species in the bay are *Porites compressa* and *Montipora capitata*. Other important substrates include coral rubble, sand, macroalgae and coralline algae.

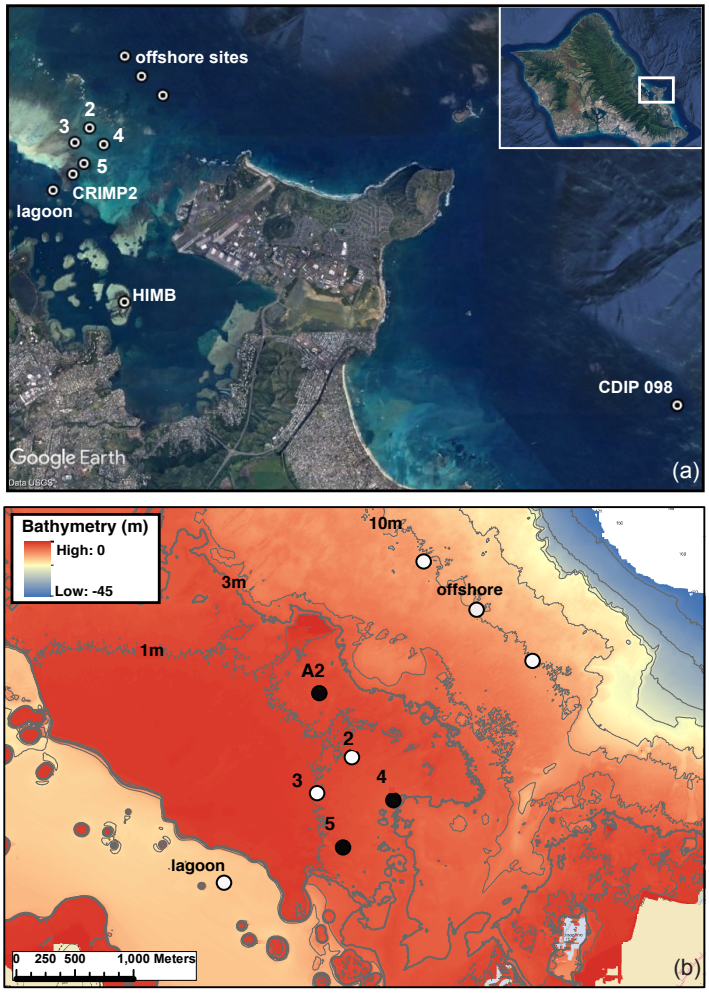

Figure IV.1 a) Satellite image of O‘ahu and location of Kāne‘ohe Bay with study site boxed in white (inset) and image of bay with locations of sampling sites, CDIP Buoy 098, HIMB and CRIMP2 buoy; b) bathymetric image of study location and sampling sites Discrete sampling sites in (b) are show in white. Instruments were deployed at stations 2, 3, 4 and 5, but stations 4 and 5 were not sampled for water chemistry. The primary offshore site for sampling was the middle station. A2 was used as a reference point in the residence time calculations (Lowe et al. 2009b).

Study set up

Two, four-day deployments during January 2017 (1/14-1/17 and 1/23-1/26) were conducted on the southeast portion of the Kāneʻohe Bay barrier reef (Fig 4.1). Discrete surface samples for TA, DIC, POC concentration ([POC]), δ^{13}C-POC and dissolved inorganic nutrients (nitrate, nitrite, ammonium, phosphate and silicate) were collected at morning (7:00-9:00), noon (12:30-13:30) and evening (16:00-17:00) at six sites along an assumed water flow path, from offshore of the reef crest (3 offshore sites), across the reef flat (sites 2 and 3) and into the lagoon (1 lagoon site) (Fig. 4.1). Due to time constraints, it was not possible to sample all open ocean sites for each sampling trip. Therefore, the middle offshore station was sampled during each sampling trip and those samples were used in this analysis. Several samples for [POC] and δ^{13}C-POC were also collected from ʻĀhuimanu Stream, which empties into the central bay. Conductivity, temperature, and depth (CTD) profiles were conducted concurrently with each offshore sample using a SonTek Castaway CTD. Temperature and salinity at stations 2 and 3 were measured with Seabird SBE-37 MicroCATs deployed on the reef at each site. Wind speed and photosynthetically active radiation (PAR) were measured at a weather station located on Moku o Loʻe at the Hawaii Institute of Marine Biology (HIMB) (pacioos.hawaii.edu/weather/obs-mokuoloe/) in southern Kaneohe Bay and offshore wave heights were obtained from the Coastal Data Information Program (CDIP) Buoy 098.

Nortek Aquadopp Acoustic Doppler current Profilers (ADP) were placed at stations 2, 3, 4 and 5 and measured current velocities at 4-min intervals (Fig 4.1).

Current measurements at sites 3 and 5 were interrupted near the end of the deployment. When measurements were not available, currents at these sites were estimated using current measurements at site 2. To reconstruct currents at sites 3 and 5, a linear relationship between transport at site 2 and site 3 or 5 was made when measurements were available. This relationship was used, along with measurements at site 2, to reconstruct currents at sites 3 and 5. To test this method, currents were reconstructed for periods where current measurements were available, and the R^2 between the actual and reconstructed currents was 0.71 ($p << 0.01$) at both sites 3 and 5.

Sampling and analysis procedures

Seawater samples for TA and DIC analyses were collected using a Niskin bottle deployed at 1 m depth. Water was transferred into 250 mL borosilicate glass bottles fixed with 100 µL saturated mercuric chloride and sealed with Apiezon grease (Dickson et al. 2007). TA and DIC were analyzed on a Versatile Instrument for the Determination of Total inorganic carbon and titration Alkalinity (VINDTA) 3C, which uses an open cell potentiometric titration for TA and coulometric titration for DIC. Certified Reference Materials (CRMs) were provided by A. Dickson (Scripps Institute of Oceanography) and used to standardize TA and DIC measurements (Dickson et al. 2007). The mean precision of these measurements was ±2.6 µmol kg^{-1} for DIC and ±2.0 µmol kg^{-1} for TA. The remaining parameters of the carbonate system (e.g., pH, carbon dioxide partial pressure (pCO_2), Ω_{ar}) were calculated using CO2SYS (Pierrot et al. 2006) and the constants of Mehrbach et al. (1973) refit by Dickson and Millero (1987). Nutrient samples were analyzed using standard World Ocean Circulation Experiment

(WOCE) segmented flow methodologies on an Astoria Analyzer (Astoria-Pacific) (WHP 1994).

Samples for [POC] and δ^{13}C-POC analyses were obtained by filtering 4 liters of seawater through pre-combusted glass-fiber filters (GF/F, Whatman) within 2 hours of collection, and stored in a -80 °C freezer until shipment to the Stable Isotope Geosciences Facility (SIGF) at Texas A&M University. The filters were acidified with HCl to remove inorganic carbon, rinsed with DI water and folded into tin capsules which were combusted with pure O_2 at 1020°C to CO_2 and analyzed using a Carlo Erba NA 1500 Series 2 Elemental Analyzer attached to a ThermoFinnigan Conflo III and a ThermoFinnigan Delta Plus XP isotope ratio mass spectrometer (IRMS). Raw sample δ^{13}C measurements are converted to the VPDB isotopic scales through an intra-run, two-point calibration of ~1 mg of L-glutamic acid standards (USGS 40 δ^{13}C = -26.39‰ VPDB, and USGS 41 δ^{13}C = 37.63‰ VPDB). Internal laboratory standards, are utilized as internal checks of the accuracy and precision of the calibrations. Precision of δ^{13}C was ±0.2‰ and ±0.2% for mass C (mg). Blank filters were also analyzed to check background levels which were negligible to non-existent.

Residence times

To determine the residence time of water on the reef flat, we used a "quasi-Lagrangian framework" (similar to DeCarlo et al., 2017). This involved tracing the path of a water parcel on the reef using water velocity and bathymetry data. Velocities were measured every 4 minutes at sites 2, 3, 4 and 5 with ADPs (Fig 4.1). For each seawater sample taken at site 2 or 3, the residence time was estimated by back-tracking in time,

using depth-averaged velocity (in two-dimensions) and water depth (d) at the four ADPs, and bathymetry data from LIDAR (accuracy=0.15 m) for the whole reef. Velocities at each point were calculated by linearly interpolating the transport between the four ADPs, and when the water parcel was outside the bounds of the four stations, nearest-neighbor extrapolation was used. The "tidal difference" (η) in water depth was also interpolated in the same way as the water velocity, and the bathymetry (b) at any point was used to calculate a depth at each parcel location ($d = \eta + b$). Water parcels were tracked across the reef flat until they reached deeper water (3m depth), and were deemed "offshore" of the reef crest.

Since many of the parcels originated to the north of our sampling sites, more information was needed to determine the transport in that section of the reef. When parcels were outside of the bounds of the four current meters, unphysical results were seen due to the nearest-neighbor extrapolation method. Lowe et al. (2009) took current measurements north of the transect (point A2, Fig 4.1). These current measurements, and a model of flow, were compared to the data that was taken during this deployment. Measured mean flow and direction at A2 was similar in magnitude and direction to flow at site 3 during this deployment. The average depth at A2 is 2 m, and the average depth at site 3 was 1.7 m. Currents at site 3 were approximately 33% smaller during this deployment, and the principal axes of site 3 major and minor components were approximately 13% and 34% smaller than at A2, respectively. The orientation of the principal axes at A2 was 246°, and site 3 was 277° for this deployment (Lowe et al. 2009). For the parcel tracing, the current data from site 3 was assumed to be similar

enough to A2, and was repeated at the location of A2, to expand the area where current data and depth could be interpolated for the parcel tracing.

One source of error in the residence time calculations is instrument error, which is 1% of the current measurements. Likely the largest source of error is the methodological assumption that the measured currents are representative of currents at other locations on the reef. We estimated this error by performing a sensitivity analysis, where we artificially relocated the current measurements and recalculated the residence times, giving a residence time error of up to 20%.

Calculations

NEC was calculated using the alkalinity anomaly method (Chisholm and Gattuso 1991) shown in the following equation:

$$NEC = \frac{\Delta TA \rho h}{2t} \quad (4.1)$$

where ΔTA is the change in TA (μmol kg^{-1}) between the reef crest (defined here as 3m depth) and site 2 or 3. We assume that the carbonate chemistry and POM chemistry of the water at our offshore sites is representative of water entering the reef crest from offshore. ρ is seawater density (kg m^{-3}), h is the time-averaged depth (m) of the water parcel and t is the residence time (hrs) from the reef crest to site 2 or site 3.

NEP was calculated using changes in DIC and correcting for the influence of NEC and air-sea CO_2 flux (F_{CO2}, mmol C m^{-2} d^{-1}) according to the equations:

$$NEP = \frac{\Delta DIC\rho h}{t} - NEC - F_{CO2} \quad (4.2)$$

$$F_{CO2} = ks(pCO_{2sw} - pCO_{2air}) \quad (4.3)$$

where ΔDIC is the DIC (μmol kg^{-1}) change from the reef crest to site 2 or 3, k is the gas transfer velocity (Ho et al. 2006), s is the solubility of CO_2 as a function of temperature and salinity (Weiss 1974), and pCO_{2sw} and pCO_{2air} are the pCO_2 of seawater and air, respectively. pCO_{2sw} was calculated using our discrete TA and DIC measurements and CO2SYS (Pierrot et al. 2006) and pCO_{2air} was obtained from the nearby CRIMP2 mooring (https://www.pmel.noaa.gov/co2/story/CRIMP2).

In order to calculate oceanic POC uptake across the reef transect, we must distinguish between POC produced by the reef and POC supplied to the reef by the nearby open ocean. First, a two end-member isotope mixing model was used to determine the concentration of oceanic POC ($[POC_{oc}]$) in the total POC pool. This equation is expressed as:

$$[POC_{oc}] = \frac{\delta^{13}C_{2(3)} - \delta^{13}C_{rf}}{\delta^{13}C_{oc} - \delta^{13}C_{rf}} * [POC_{2(3)}] \quad (4.4)$$

where $\delta^{13}C_{2(3)}$ is the measured isotopic composition of POC at either site 2 or 3, $\delta^{13}C_{rf}$ is the estimated isotopic composition of reef-derived POC, $\delta^{13}C_{oc}$ is the measured isotopic composition of oceanic POC (e.g., the offshore sample) and $[POC_{2(3)}]$ is the measured

concentration of total POC at site 2 or 3. The $\delta^{13}C_{rf}$ was estimated from the literature assuming the major components of reef POM are coral mucus (30%), coral zooxanthellae (30%), fish feces (30%) and macroalgae (10%) (Table 4.1). The contributions of each component are based on Wyatt et al. (2013) who found roughly comparable releases of each component at Ningaloo reef, Australia. Average $\delta^{13}C$ of coral mucus (-15.9‰, range = -16.9 – -15‰) and zooxanthellae (-14.7‰, range = -15 – -14.5‰) were obtained from a study conducted in Kāneʻohe Bay, using the major coral species in the bay, *Porites* and *Montipora* (Rodrigues and Grottoli 2006). As far as we know, there are no published data on the isotopic composition of fish feces and macroalgae in Kāneʻohe Bay. Therefore, we obtained isotopic values for these components from coral reef studies conducted in Ningaloo reef and the Caribbean Sea (de la Moriniere et al. 2003; Wyatt et al. 2013). These studies report a range of $\delta^{13}C$ for fish feces and macroalgae (e.g., turf algae, *Halimeda*) as -17 – -12‰ (mean=-16.5‰) and -18.5 – -15‰ (mean=-17.5‰), respectively. The weighted average $\delta^{13}C_{rf}$ was -15.87‰. Once $[POC_{oc}]$ was determined, oceanic POC uptake ($POC_{oc\text{-}up}$) was calculated by:

$$POC_{oc-up} = \frac{\Delta POCh}{t} \tag{4.5}$$

where ΔPOC is the change in $[POC_{oc}]$ between the reef crest and site 2 or 3.

To acquire offshore TA, DIC, δ^{13}C-POC and [POC], water samples were collected offshore, 3 times a day. During deployment 1, upstream values for each reef sample were determined by using the time it took the water parcel to travel from the reef crest to site 2 or 3 (i.e., residence time) and connecting it to the nearest time of the offshore sample. For deployment 2, three samples (1/23 16:45, 1/24 07:32 and 16:46) were flagged as outliers and so the average offshore TA (2301±4.85 µmol kg^{-1}), DIC (1993±6.7 µmol kg^{-1}), and δ^{13}C (-26.24±1.64), excluding the outliers, was used for the entire deployment.

Table IV.1 Average δ^{13}C (‰) associated with each of the components in reef POM, along with associated ranges found in the literature. δ^{13}C values for coral mucus and zooxanthellae were obtained from a study conducted in Kāneʻohe Bay for the major species in the bay (Rodrigues and Grottoli 2006). Percent (%) contributions of each component were estimated in Wyatt et al. (2013). Weighted average δ^{13}C of reef POM is -15.7‰.

	Coral Mucus*	Zooxanthellae*	Fish Feces	Macroalgae
Average δ^{13}C (δ^{13}C ranges)	-15.9 (-16.9 – -15)	-14.7 (-15 – -14.5)	-16.5 (-17 – -12)	-17.5 (-18.5 – -15)
% Contribution	30	30	30	10

The uncertainties in NEC, NEP and $POC_{oc\text{-}up}$, were estimated using a Monte Carlo approach (n=10^4), which propagates the uncertainties (standard deviation or standard error) of each of the parameters through the calculations (Table B-2). To incorporate an uncertainty associated with the estimation for average $\delta^{13}C_{rf}$, we calculated $POC_{oc\text{-}up}$ assuming reef POC was composed of 100% macroalgae (i.e., $\delta^{13}C_{rf}$ =-17.5‰), and of 100% zooxanthellae (i.e., $\delta^{13}C_{rf}$ =-14.7‰). This introduced an ~18%

uncertainty into the calculation. Excluding values not statistically different from 0, the relative standard deviations (%RSD) for NEC and NEP were approximately 30% and 40% for deployment 1 and 2, respectively. For $POC_{oc\text{-}up}$ uptake, %RSD was approximately 40% and 50% for deployment 1 and 2, respectively. The uncertainties increased ~10% during the second deployment due to the averaging of offshore values. For NEC, NEP and $POC_{oc\text{-}up}$, sources that contributed greatest to the total uncertainty were residence time during the first deployment and the averaging of offshore TA, DIC and δ^{13}C-POC during the second deployment.

Results

Residence times

During the first deployment, average wave height was 1.44±0.11 m, wind speed was 2.66±1.30 m s^{-1} and current speeds were 3.33±1.84 cm s^{-1} at site 3 and 7.40±3.76 cm s^{-1} at site 2. Stormy conditions during the second deployment increased average swell height and wind speed to 2.52±0.45 m and 4.86±2.07 m s^{-1}, respectively. Average current speed also increased to 7.44±3.33 cm s^{-1} at site 3 and 20.29±6.91 cm s^{-1} at site 2. This led to different water flow paths during each deployment (Fig 4.2). Water flow during the first deployment was driven by tides and bathymetry, causing water parcels to meander back and forth across the reef flat. Due to these tidal oscillations, 11 water parcels traveled from the lagoon to our reef sites. These data were not included in this analysis. During deployment 2, wave breaking on the reef crest drove water across the reef, which lead to unidirectional flow. Consequently, average residence time during the first deployment was 13.1±4.3 hours, compared to 3.7±1.4 hours during the second

deployment. After excluding samples affected by offshore flow, as well as a few POM samples lost in laboratory analysis errors (e.g., carbonate contamination, dropped samples), a total of 33 (out of 48) paired NEC-$POC_{oc\text{-}up}$ samples were deemed reliable for this analysis.

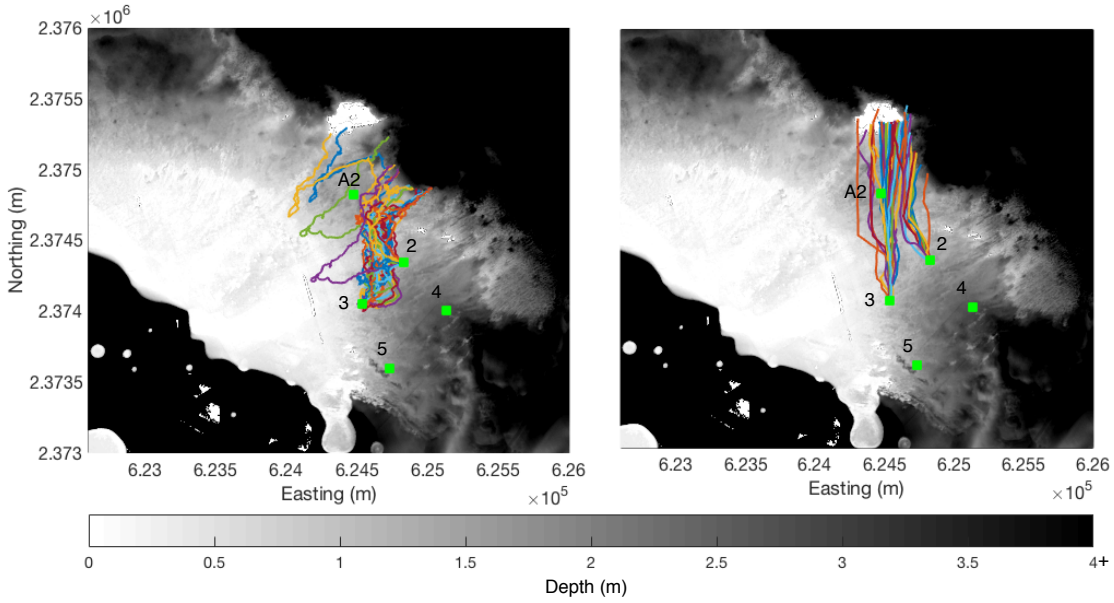

Figure IV.2 Flow paths for individual water parcels at sites 2 and 3 during deployment 1 (left) and deployment 2 (right).

Carbon isotopes and POC

The two end-member isotope mixing model relies on the assumptions that each of the sources have a distinct isotopic composition, there are no additional sources of POC other than the open ocean and the reef, and the δ^{13}C-POC increases as water traverses across the reef (e.g., from POC composed of autotrophic phytoplankton to POC

derived from a mix of heterotrophic and autotrophic reef organisms). First and second deployment average open ocean δ^{13}C-POC was -25.11±0.86‰ and -26.24±1.64‰, respectively (Fig 4.3a). At site 2, mean δ^{13}C-POC was -22.18±1.16‰ and -22.71±2.04‰ for deployments 1 and 2, respectively. Mean δ^{13}C-POC at site 3 was -20.24±0.74 ‰ and -23.22±1.43‰ for deployments 1 and 2, respectively. Within each site, there was no significant difference ($p<0.001$) in average δ^{13}C between deployments, except at site 3 which had a heavier (more positive) δ^{13}C during the first deployment. This is probably because water residence time was longer, which allows reef POM to accumulate and contribute a greater proportion to the total POM pool. Open ocean δ^{13}C-POC was significantly different from site 2 and 3, but not from the river (-25.84±0.80‰) or lagoon (1st deployment=-25.21±0.63‰, 2nd deployment=-24.14±2.27‰). Although lagoon δ^{13}C-POC might be influenced by river POC, samples at site 2 and 3 that originated in the lagoon were removed from this analysis. Hence, there should be no influence of lagoon or river water at sites 2 or 3 for samples with which we calculated $POC_{oc\text{-}up}$. There was no significant difference in [POC] (6.72±4.50 μmol L^{-1}) between sites or deployments (Fig 4.3b). Mean [POC] for all sites in Kaneohe bay is greater than the mean surface [POC] at HOT (2.2±0.5 μmol kg^{-1}), and at the higher end of [POC] measured at other reefs (2.2-8.7 μmol L^{-1}, Atkinson and Falter 2003).

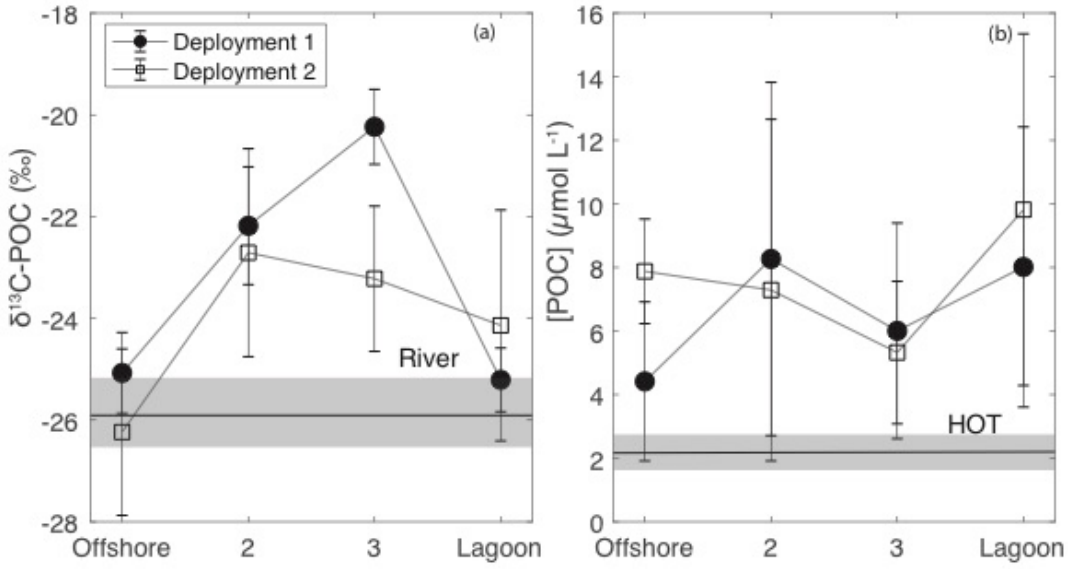

Figure IV.3 a) First and second deployment δ^{13}C-POC (‰) (mean±std dev) at each site, including the ʻĀhuimanu Stream mean (black horizontal line) and standard deviation (shading), and b) POC concentration ([POC], µmol L^{-1}) at each site, including the Hawaii Ocean Time-series (HOT) 1989-2016 mean (black horizontal line) and standard deviation (shading).

NEC and oceanic POC uptake

NEC and $POC_{oc\text{-}up}$ were calculated across two flow paths: from the reef crest to site 2, and from the reef crest to site 3 (Figs 4.1 and 4.2). There was no significant difference in average NEC or $POC_{oc\text{-}up}$ between sites 2 and 3, during either deployment (Table B-3). Average NEC for deployments 1 and 2 were 1.85±1.54 mmol C m^{-2} h^{-1} and 5.46±3.59 mmol C m^{-2} h^{-1}, respectively (Fig 4.4, Table B-3). NEC was significantly higher during deployment 2 at both sites 2 and 3. There were four negative NEC values (2 during each deployment) measured during morning hours, although three of these values were not statistically different from 0. Average $POC_{oc\text{-}up}$ for deployments 1 and 2

were 0.35±0.25 mmol C m^{-2} h^{-1} and 0.96±0.70 mmol C m^{-2} h^{-1}, respectively. $POC_{oc\text{-}up}$ was also higher during the second deployment, but only significantly higher at site 2. A linear, positive correlation exists between NEC and $POC_{oc\text{-}up}$ (slope±SE=4.30±0.71, n=33, R^2=0.54, p<0.001), and higher NEC and $POC_{oc\text{-}up}$ correspond to faster average flow speeds and greater turbulent velocities ($u^* = \sqrt{C_d * U^2}$, where C_d is the bottom drag coefficient, C_d = 0.02 for Kaneohe Bay (Lowe et al. 2009a) and U is the magnitude of the velocity along the flow path) (Fig 4.4). Average flow speed was correlated to NEC ($R^2 \geq 0.54$) and $POC_{oc\text{-}up}$ ($R^2 \geq 0.67$) with significant linear and exponential regressions (Fig A-23). No significant correlations exist between NEC or $POC_{oc\text{-}up}$ and NEP, Ω_{ar}, light, temperature, or inorganic nutrients.

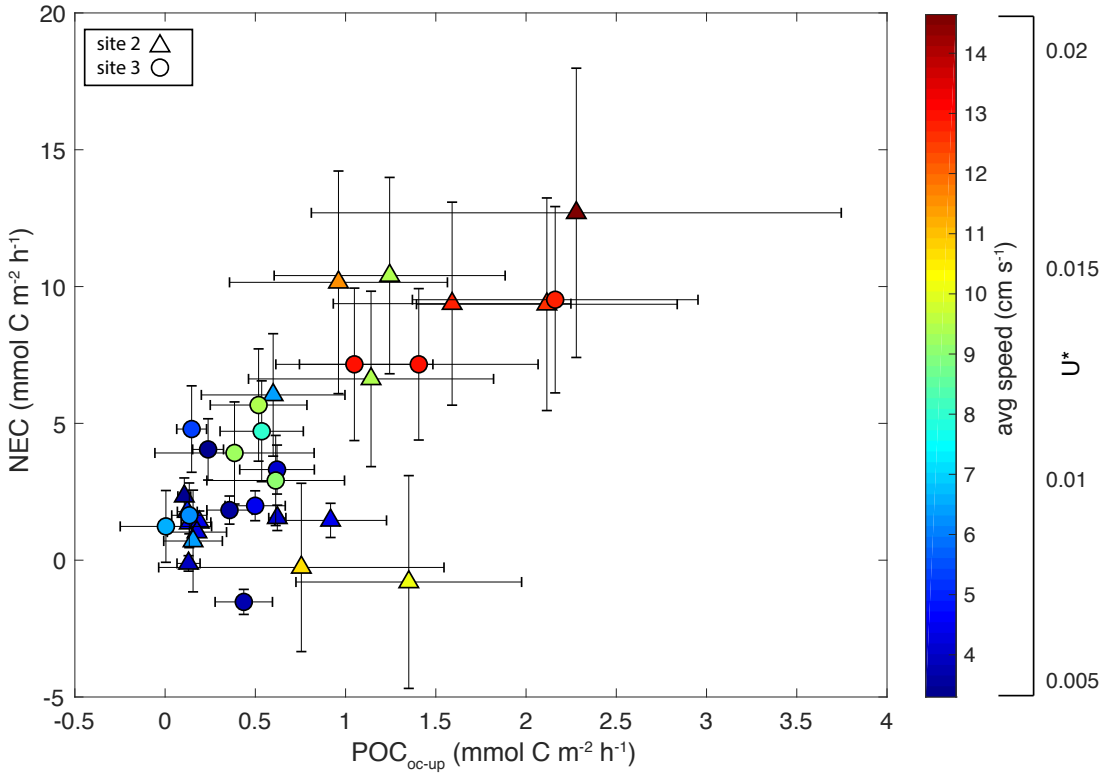

Figure IV.4 $POC_{oc\text{-}up}$ and NEC for site 2 (triangles) and site 3 (circles). The color bar represents average flow speed and turbulent velocity (U*) across the transect, for each water parcel sampled.

Discussion

Our results show that the Kāne‘ohe Bay barrier reef was net calcifying during most of this study. There were four measurements of net dissolution (-NEC) that correspond to measurements of net respiration (-NEP), which causes an increase in CO_2 and can drive $CaCO_3$ dissolution in undersaturated environments such as sediment pore waters (Yates and Halley 2006; Eyre et al. 2018). Although these four negative NEC values correspond with negative NEP, there was not an overall correlation between NEC and NEP. However, NEC was positively correlated with flow speed, which influences

the thickness of the bottom boundary layer. Faster flow speeds lead to a thinner benthic boundary layer and enhance exchange with the overlying water column. This may benefit calcification by promoting uptake of carbonate and bicarbonate ions and export of hydrogen ions between the coral and the surrounding water (Jokiel 2011; Comeau et al. 2014).

NEC was also significantly correlated with $POC_{oc\text{-}up}$, which may suggest that the reef ecosystem can utilize this external source of food to elevate calcification (Fig 4.4). Heterotrophy has been hypothesized to elevate NEC on other reef systems (Shamberger et al. 2011; Yeakel et al. 2015; DeCarlo et al. 2017). For example, Shamberger et al. (2011) hypothesized that high NEC rates on the Kaneohe Bay barrier reef may be due to high rates of heterotrophic feeding and our latest results support this hypothesis. Yeakel et al. (2015) observed a correlation between enhanced offshore productivity and NEC on a Bermuda coral reef, and speculated that pulses of external nutrients were increasing heterotrophy and NEC on the reef. DeCarlo et al. (2017) measured the highest coral reef NEC rates at Dongsha reef in the northern South China Sea, a region affected by strong internal waves (Decarlo et al. 2015). Internal waves deliver nutrient-rich water to the surface, enhance phytoplankton productivity and can increase the flux of organic matter to nearby coral reefs (Leichter et al. 1998). Corals exposed to large internal waves show signs of enhanced heterotrophy and growth, relative to corals sheltered from internal waves (Roder et al. 2010). Hence, external inputs of POM and subsequent heterotrophic consumption of this organic matter may have provided additional nutrients to elevate NEC at Dongsha and other reefs (DeCarlo et al. 2017).

The rate of $POC_{oc\text{-}up}$ appears to be affected by flow regime, where faster speeds lead to greater $POC_{oc\text{-}up}$. The effects of flow speed on capture rates by suspension feeders have been explored in both laboratory and field studies and in most cases, optimal flow speeds for particle trapping are approximately 10-30 cm s^{-1} (Sebens and Johnson 1991; Fabricius et al. 1995; Sebens et al. 1998; Ribes et al. 2003). We measured the greatest $POC_{oc\text{-}up}$ rates during deployment 2, when average current speed was near or within the range of optimal flow for particle capture (site 3=7.44±3.33 cm s^{-1}; site 2=20.29±6.91 cm s^{-1}). Turbulent velocity (U*) was also greater during the second deployment, suggesting that stronger, vertical mixing aids POC consumption by breaking down the bottom boundary layer and replacing POC removed by reef organisms (Monismith et al. 2010). Alternatively, slow water flow (e.g., during deployment 1) reduces advection and may lead to a depleted POM boundary layer.

Ribes et al. (2003) found that particle removal by coral communities was proportional to concentration. At the global scale, it has been shown corals consume more carbon via heterotrophy in areas with higher concentrations of chlorophyll-*a*, a proxy for phytoplankton (Fox et al. 2018). We observed a significant correlation (slope±SE=0.34±0.11, n=9, R^2=0.59, p<0. 01) between initial [POC_{oc}] and $POC_{oc\text{-}up}$ during the second deployment but $POC_{oc\text{-}up}$ was less sensitive to changes in initial [POC_{oc}] during the first deployment (slope±SE=0.09±0.04, n=6, R^2=0.56, p=0.09) when flow speeds were slower (Fig 4.5). These relationships may suggest that at optimal flow (e.g. during deployment 2), the availability of oceanic POC can either limit or enhance

particle consumption. However, reduced flow may inhibit POC consumption by the reef through limited advection, despite sufficient offshore availability.

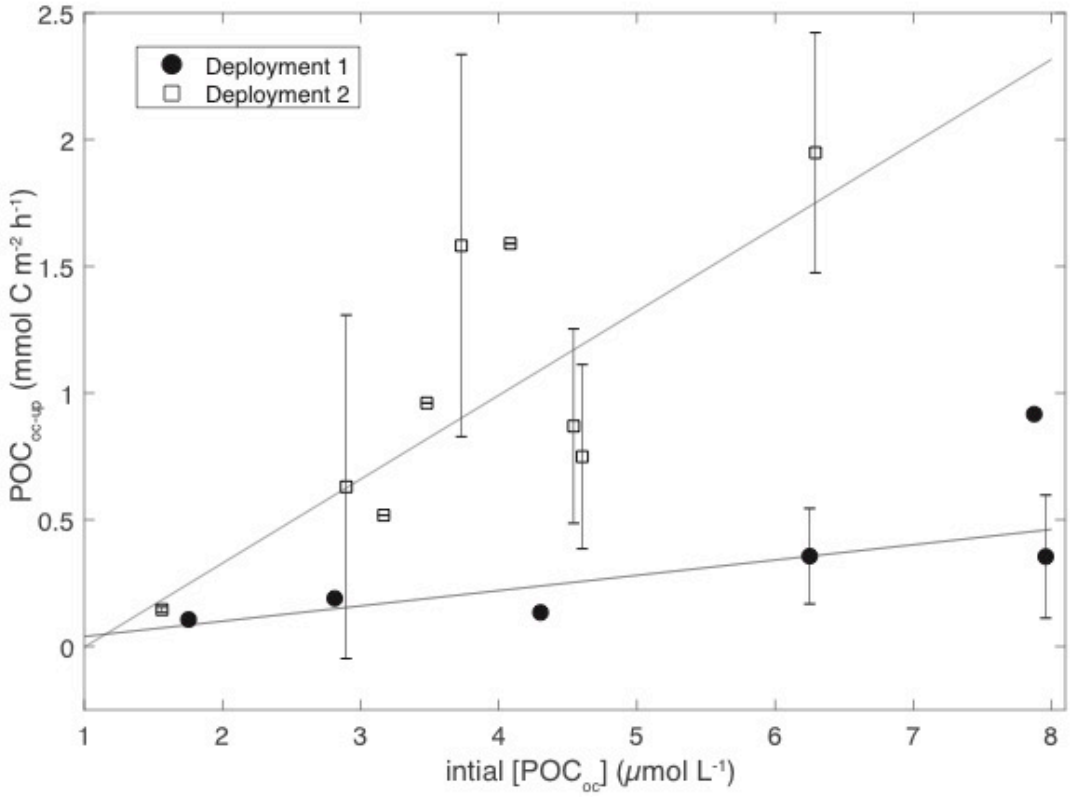

Figure IV.5 Relationship between initial oceanic POC concentration ([POC_{oc}], µmol L^{-1}) and average POC_{oc-up} (mmol C m^{-2} h^{-1}) at sites 2 and 3, for deployments 1 (circles) and 2 (squares). Since multiple parcels at sites 2 and 3 were tracked back to the same initial oceanic POC measurement, we used the average POC_{oc-up} associated with each offshore POC measurement.

Significant relationships between NEC and Ω_{ar} and between NEC and NEP have been observed in previous studies of individual reef ecosystems, though the sensitivity of NEC to changing Ω_{ar} and NEP (i.e. NEC-Ω_{ar} and NEC-NEP slopes) is highly variable

(e.g., Andersson et al. 2009; Shamberger et al. 2011; Albright et al. 2013; Shaw et al. 2015). However, when examining all the data in this study, there is no correlation between NEC and Ω_{ar} or NEP (Fig 4.6). Similarly, when combining data from coral reefs globally, no significant relationship is found between NEC and Ω_{ar} or NEP (DeCarlo et al. 2017). In contrast, our data do show a significant relationship between NEC and Ω_{ar} and between NEC and NEP when $POC_{oc\text{-}up}$ rates are low (<0.9 mmol C m^{-2} h^{-1}) (Fig 4.6). It is possible that a global relationship between NEC and Ω_{ar} or NEP is not apparent because data from reefs with both high and low $POC_{oc\text{-}up}$ are being combined. Furthermore, the Kaneohe Bay barrier reef ecosystem maintained positive NEC at low $POC_{oc\text{-}up}$, indicating that there are other important factors driving NEC at low $POC_{oc\text{-}up}$. We do not have enough data to evaluate the sensitivity of NEC to Ω_{ar} or NEP under high $POC_{oc\text{-}up}$, but laboratory experiments suggest that although consumption of particulates increases the rate of coral calcification, it does not change the sensitivity of calcification to decreasing Ω_{ar} (i.e., coral calcification decreases at similar rates under fed and not fed conditions) (Edmunds 2011; Drenkard et al. 2013). In other words, coral reefs with higher $POC_{oc\text{-}up}$ may not respond any differently to ocean acidification, but they may persist longer because their initial supply of food and energy is greater and hence, supports higher initial NEC rates. Considering heterotrophic consumption of oceanic POM in NEC studies may help to resolve variability across individual reefs and in the global NEC-Ω_{ar} relationship, and identify coral reefs that are likely to maintain net calcification further into the future under climate change stressors.

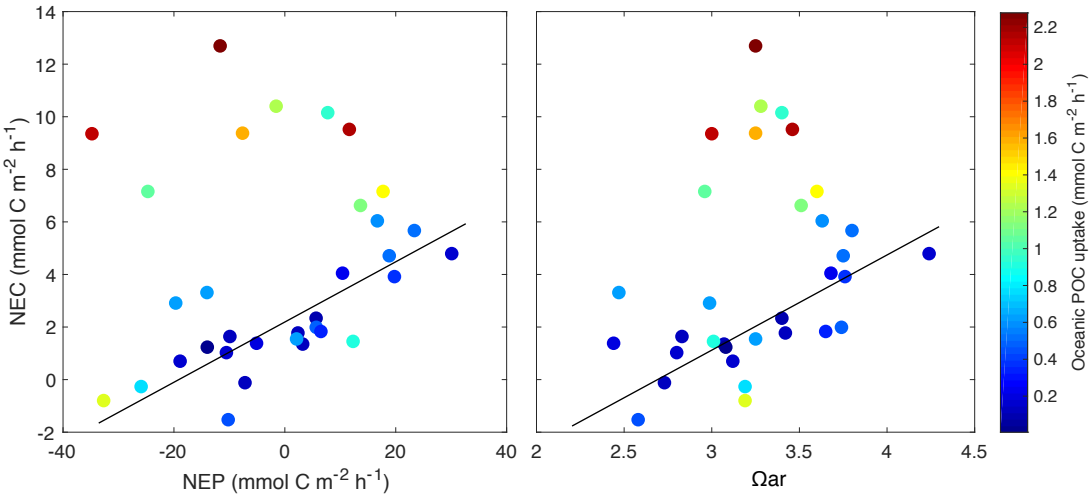

Figure IV.6 Relationships between NEC-NEP (left panel) and NEC-Ω_{ar} (right panel). Colors represent $POC_{oc\text{-}up}$. Strong, significant ($p<0.001$) correlations for NEC-NEP ($R^2=0.56$) and NEC-Ω_{ar} ($R^2=0.43$) exist at $POC_{oc\text{-}up} < 0.9$ mmol C m^{-2} h^{-1}, which also corresponds to lower NEC (~<6 mmol C m^{-2} h^{-1}).

Coral reef calcification is expected to decline as a result of ocean acidification and warming, and the observed reduction in offshore productivity will exacerbate these effects. Oceanic productivity is limited by light, temperature and nutrients, all of which are affected by physical processes that influence mixed-layer depth (Raymont et al. 1980; Sarmiento et al. 2004; Behrenfeld et al. 2006; Sarmiento and Gruber 2006). Rising sea surface temperatures have enhanced stratification at low-latitudes, where coral reefs reside. These areas experience reduced nutrient fluxes to the upper ocean and a decrease in surface ocean productivity. The areal size of oligotrophic regions has also expanded (Polovina et al. 2008). Furthermore, ocean acidification is expected to impair calcification and enhance dissolution in phytoplankton that form calcium carbonate tests (e.g., coccolithophores), shifting the structure of oceanic phytoplankton communities

(Doney et al. 2009; Beaufort et al. 2011). Although studies on phytoplankton selectivity by corals are sparse, there is some evidence of selection based on prey species or size (Houlbrèque and Ferrier-Pagès 2009; Leal et al. 2013). Changes in small and large scale circulation patterns may also affect phytoplankton diversity and dispersal (Barton et al. 2010). Combined, these processes could alter or reduce oceanic POM export to coral reefs, thereby decreasing the availability of external nutrients required to maintain high calcification rates.

This is the first study to examine the relationship between oceanic POC uptake and NEC, and more studies are needed to comprehensively understand this relationship, and determine its applicability to other coral reefs worldwide. We acknowledge that the observed correlation may be driven by the dependency of both NEC and $POC_{oc\text{-}up}$ on flow speeds. However, given the documented link between heterotrophy and coral calcification in laboratory studies (Edmunds 2011; Drenkard et al. 2013), the correlation we observed between $POC_{oc\text{-}up}$ and NEC in the field should be further explored. In this study, we also measured particulate organic nitrogen (PON), but the $\delta^{15}N$ of POM did not follow the assumptions of the isotope mixing model and we were unable to calculate uptake rates for oceanic PON. However, coral reefs are nitrogen-limited and allochthonous PON is also an important source of nutrients to the ecosystem (Wyatt et al. 2010). The oceanic PON uptake-NEC relationship could also improve predictions of coral reef health under climate change.

CHAPTER V

CONCLUSIONS

Gulf of Mexico and Flower Garden Banks

The ~20 year time-series of observational CO_2 measurements in the GoM provides information on source water carbonate chemistry characteristics to the FGB. Spatial and temporal variability in the underway dataset were primarily driven by biological activity, which can be linked to terrestrial freshwater inputs, as well as seasonal changes in temperature. We show evidence for an open ocean acidification signal in pCO_2, which is similar to the trends measured in the Altlantic and Carribean Sea. The coastal GoM acidification rate was approximately four times faster than the open ocean, and is primarily due to an increase in SST, which was not observed in the open ocean. Hence, global ocean acidification and enhanced coastal acidification are a major concern for the future health of GoM ecosystems, including the FGB coral reefs.

Although seasonal eutrophication-induced hypoxia occurs in the northern GoM, we determined this hypoxia did not extend to the FGB and cause the mortality event. Instead, we hypothesize that hypoxia at the EB formed independently by the presence of two water masses: river-derived water at the surface, and deep water that upwelled onto the bank. The fresh, hazy surface layer blocked sunlight, and increased net respiration of organic matter on the reef. Deep, dense, upwelled water settled in pockets on the reef to create bottom-water stratification. As respiration in the bottom layer increased, oxygen declined, and within ~ 2 days, hypoxia formed. Although this was an isolated event at the FGB, hypoxia is emerging as a global concern to coral reefs. Moving forward, coral

reef monitoring efforts should increase temporal sampling resolution and routinely include oxygen and carbonate chemistry measurements for detection of future hypoxia events.

NEC and Oceanic POC Uptake

The results of our study indicate that the Kāne‘ohe Bay barrier reef ecosystem is consuming oceanic POC and may be utilizing this resource to elevate calcification rates. $POC_{oc\text{-}up}$ appears to be sensitive to flow speeds, as well as the availability of offshore POC. Reductions in offshore productivity via changes in surface ocean temperatures, stratification and nutrient supply have already been documented in low-latitude regions (Behrenfeld et al. 2006; Polovina et al. 2008; Boyce et al. 2010). Ocean acidification, warming, and open ocean circulation changes will also impact phytoplankton community composition and dispersion (Riebesell et al. 2000; Karl et al. 2001; Doney et al. 2009; Barton et al. 2010). These changes could decrease the food supply to coral reefs, resulting in reef-scale calcification declines and negatively impacting the structure and health of the ecosystem. Alternatively, coral reefs that continue to receive a healthy supply of oceanic POC (e.g., via internal waves and upwelling), and that have faster water flow, may be more resistant to stressors that impede calcification. Since this is the first study to document a direct connection between NEC and $POC_{oc\text{-}up}$, subsequent studies are needed to confirm this relationship, characterize potential variability in the relationship over different time scales, improve our understanding of the mechanisms driving the relationship, and refine and improve the methodologies used in this study.

Additionally, conducting this study in coral reefs with variable inputs of POM may help to identify hot spots for coral reefs more resilient to climate change.

REFERENCES

Albright, R., C. Langdon, and K. R. N. Anthony. 2013. Dynamics of seawater carbonate chemistry, production, and calcification of a coral reef flat, central Great Barrier Reef. Biogeosciences **10**: 6747–6758. doi:10.5194/bg-10-6747-2013

Altieri, A. H., S. B. Harrison, J. Seemann, R. Collin, R. J. Diaz, and N. Knowlton. 2017. Tropical dead zones and mass mortalities on coral reefs. Proc. Natl. Acad. Sci. **114**: 3660–3665. doi:10.1073/pnas.1621517114

Andersson, A. J., I. B. Kuffner, F. T. MacKenzie, P. L. Jokiel, K. S. Rodgers, and A. Tan. 2009. Net Loss of CaCO3 from a subtropical calcifying community due to seawater acidification: Mesocosm-scale experimental evidence. Biogeosciences **6**: 1811–1823. doi:10.5194/bg-6-1811-2009

Atkinson, M. J., and J. L. Falter. 2003. Coral Reefs, p. 40–64. *In* K. Black and G. Shimmield [eds.], Biogeochemistry of Marine Systems. CRC Press.

Baird, A. H., S. A. Keith, E. Woolsey, R. Yoshida, and T. Naruse. 2017. Rapid coral mortality following doldrums-like conditions on Iriomote, Japan. F1000Research **6**: 1728. doi:10.12688/f1000research.12660.1

Baohua, Zhu Guangce, Wang Bo, Huang Tseng, C. 2004. Effects of temperature, hypoxia, ammonia and nitrate on the bleaching among three coral species. Chinese Sci. Bull. **49**: 1923–1928. doi:10.1360/04wc0195

Barton, A., S. Dutkiewicz, G. Flierl, J. Bragg, and M. Follows. 2010. Patterns of diversity in marine phytoplankton. Science (80-.). **525**: 1509–1512.

doi:10.1016/B978-0-12-693010-8.50008-6

Bates, N., Y. Astor, M. Church, and others. 2014. A Time-Series View of Changing Ocean Chemistry Due to Ocean Uptake of Anthropogenic CO2 and Ocean Acidification. Oceanography **27**: 126–141. doi:10.5670/oceanog.2014.16

Bates, N. R., M. H. P. Best, K. Neely, R. Garley, A. G. Dickson, and R. J. Johnson. 2012. Detecting anthropogenic carbon dioxide uptake and ocean acidification in the North Atlantic Ocean. Biogeosciences **9**: 2509–2522. doi:10.5194/bg-9-2509-2012

Beaufort, L., I. Probert, T. De Garidel-Thoron, and others. 2011. Sensitivity of coccolithophores to carbonate chemistry and ocean acidification. Nature **476**: 80–83. doi:10.1038/nature10295

Behrenfeld, M. J., R. T. O'Malley, D. A. Siegel, and others. 2006. Climate-driven trends in contemporary ocean productivity. Nature **444**: 752–755. doi:10.1038/nature05317

Belabbassi, L., P. Chapman, W. D. Nowlin, A. E. Jochens, and D. C. Biggs. 2005. Summertime nutrient supply to near-surface waters of the northeastern gulf of Mexico: 1998, 1999, and 2000. Gulf Mex. Sci. **23**: 137–160. doi:10.18785/goms.2302.01

Bianchi, T. S., S. F. DiMarco, J. H. Cowan, R. D. Hetland, P. Chapman, J. W. Day, and M. A. Allison. 2010. The science of hypoxia in the northern Gulf of Mexico: A review. Sci. Total Environ. **408**: 1471–1484. doi:10.1016/j.scitotenv.2009.11.047

Biggs, D., and F. Muller-Karger. 1994. Ship and satellite observations of chlorophyll stocks in interacting cyclone-anticyclone eddy pairs in the western Gulf of Mexico.

J. Geophys. Res. Ocean. **99**: 7371–7384.

Boyce, D. G., M. R. Lewis, and B. Worm. 2010. Global phytoplankton decline over the past century. Nature **466**: 591–596. doi:10.1038/nature09268

Bray, J. R., and J. T. Curtis. 1957. An ordination of the upland forest communities of southern Wisconsin. Ecol. Monogr. **27**: 325–349.

Breitburg, D. 2002. Effects of hypoxia, and the balance between hypoxia and enrichment, on coastal fishes and fisheries. Estuaries **25**: 767–781. doi:10.1007/BF02804904

Bright, T. J. 1977. Coral reefs, nepheloid layers, gas seeps and brine flows on hard banks in the northwestern Gulf of Mexico. *Proc.(3rd) Int. Coral Reef Symp*. 3946.

Brown, B. E. 1997. Coral bleaching: causes and consequences. Coral Reefs **16**: 129–138. doi:10.1007/s003380050249

Cai, W.-J. 2003a. Riverine inorganic carbon flux and rate of biological uptake in the Mississippi River plume. Geophys. Res. Lett. **30**: 1032. doi:10.1029/2002GL016312

Cai, W. J. 2003b. Riverine inorganic carbon flux and rate of biological uptake in the Mississippi River plume. Geophys. Res. Lett. **30**: 1997–2000. doi:10.1029/2002GL016312

Cai, W. J., X. Hu, W. J. Huang, and others. 2011. Acidification of subsurface coastal waters enhanced by eutrophication. Nat. Geosci. **4**: 766–770. doi:10.1038/ngeo1297

Cai, W. J., X. Hu, W. J. Huang, L. Q. Jiang, Y. Wang, T. H. Peng, and X. Zhang. 2010. Alkalinity distribution in the western North Atlantic Ocean margins. J. Geophys.

Res. Ocean. **115**: 1–15. doi:10.1029/2009JC005482

Caldeira, K., and M. E. Wickett. 2003. Anthropogenic carbon and ocean pH. Nature **425**: 365. doi:10.1038/425365a

Chakraborty, S., and S. E. Lohrenz. 2015. Phytoplankton community structure in the river-influenced continental margin of the northern Gulf of Mexico. Mar. Ecol. Prog. Ser. **521**: 31–47. doi:10.3354/meps11107

Chavez, F., T. Takahashi, W. Cai, G. Friederich, B. Hales, R. Wanninkhof, and R. Feely. 2007. Chapter 15: The Coastal Ocean, p. 242. *In* A. King, L. Dilling, Z. GP, D. Fairman, R. Houghton, F. Marland, A. Rose, and T. Wilbanks [eds.], The first state of the carbon cycle report (SOCCR): The North American carbon budget and implications for the global carbon cycle. U.S. Climate Change Science Program.

Chen, S., C. Hu, R. H. Byrne, L. L. Robbins, and B. Yang. 2016. Remote estimation of surface pCO2 on the West Florida Shelf. Cont. Shelf Res. **128**: 10–25. doi:10.1016/j.csr.2016.09.004

Chen, X., S. E. Lohrenz, and D. Wiesenburg. 2000. Distribution and controlling mechanisms of primary production on the Louisiana - Texas continental shelf. J. Mar. Syst. **25**: 179–207.

Chisholm, J. R. M., and J. Gattuso. 1991. Validation of the Alkalinity Anomaly Technique for Investigating Calcification and Photosynthesis in Coral Reef Communities. Limnol. Oceanogr. **36**: 1232–1239.

Cho, K., R. O. Reid, and W. D. Nowlin. 1998. Objectively mapped stream function fields on the Texas-Louisiana shelf based on 32 months of moored current meter

data. J. Geophys. Res. Ocean. **103**: 10377–10390. doi:10.1029/98JC00099

Coble, P. G., L. L. Robbins, K. L. Daly, W.-J. Cai, K. Fennel, and S. E. Lohrenz. 2010. A preliminary carbon budget for the Gulf of Mexico. Ocean Carbon Biogeochem. News **3**: 1–4.

Cochrane, J. D., and F. J. Kelly. 1986. Low-frequency circulation on the Texas-Louisiana continental shelf. J. Geophys. Res. **91**: 10645. doi:10.1029/JC091iC09p10645

Cohen, A., and M. Holcomb. 2009. Why Corals Care About Ocean Acidification: Uncovering the Mechanism. Oceanography **22**: 118–127. doi:10.5670/oceanog.2009.102

Comeau, S., P. J. Edmunds, C. A. Lantz, and R. C. Carpenter. 2014. Water flow modulates the response of coral reef communities to ocean acidification. Sci. Rep. **4**. doi:10.1038/srep06681

Cyronak, T., K. G. Schulz, I. R. Santos, and B. D. Eyre. 2014. Enhanced acidification of global coral reefs driven by regional biogeochemical feedbacks. Geophys. Res. Lett. **41**: 5538–5546. doi:10.1002/2014GL060849

Dale, V. H., C. L. Kling, J. L. Meyer, and others. 2010. Hypoxia in the Northern Gulf of Mexico Introduction, B. Anderson, R. Howarth, and L. Walker [eds.]. Springer.

DeCarlo, T. M., A. L. Cohen, G. T. F. Wong, F.-K. Shiah, S. J. Lentz, K. A. Davis, K. E. F. Shamberger, and P. Lohmann. 2017. Community production modulates coral reef pH and the sensitivity of ecosystem calcification to ocean acidification. J. Geophys. Res. Ocean. **122**: 745–761. doi:10.1002/2016JC012326

Decarlo, T. M., K. B. Karnauskas, K. a Davis, and G. T. F. Wong. 2015. Climate modulates internal wave activity in the Northern South China Sea. 1–8. doi:10.1002/2014GL062522.Received

Deslarzes, K. J., and A. Lugo-Fernández. 2007. Influence of terrigenous runoff on offshore coral reefs: an example from the Flower Garden Banks, Gulf of Mexico, p. 126–160. *In* Geological approaches to coral reef ecology. Springer.

Diaz, R. J., and R. Rosenberg. 2008. Spreading Dead Zones and Consequences for Marine Ecosystems. Science (80-.). **321**: 926–929. doi:10.1126/science.1156401

Dickson, A. G., and F. J. Millero. 1987. A comparison of the equilibrium constants for the dissociation of carbonic acid in seawater media. Deep Sea Res. Part A, Oceanogr. Res. Pap. **34**: 1733–1743. doi:10.1016/0198-0149(87)90021-5

Dickson, A. G., C. L. Sabine, and J. R. Christian. 2007. Guide to best practices for ocean CO2 measurements., North Pacific Marine Science Organization.

DiMarco, S., J. Strauss, N. May, R. L. Mullins-Perry, E. L. Grossman, and D. Shormann. 2012. Texas Coastal Hypoxia Linked to Brazos River Discharge as Revealed by Oxygen Isotopes. Aquat. Geochemistry **18**: 159–181. doi:10.1007/s10498-011-9156-x

DiMarco, S., and H. M. Zimmerle. 2017. MCH Atlas: Oceanographic Observations of the Mechanism Controlling Hypoxia Project., Texas Sea Grant TAMU-SG-17-601.

Dodge, R. E., and J. C. Lang. 1983. Environmental correlates of hermatypic coral (Montastrea annularis) growth on the East Flower Gardens Bank, northwest Gulf of Mexico. Limnol. Oceanogr. **28**: 228–240. doi:10.4319/lo.1983.28.2.0228

Doney, S. C., V. J. Fabry, R. A. Feely, and J. A. Kleypas. 2009. Ocean Acidification: the Other CO2 problem. Annu. Rev. 212–251. doi:10.1146/annurev.marine.010908.163834.

Dore, J. E., R. Lukas, D. W. Sadler, M. J. Church, and D. M. Karl. 2009. Physical and biogeochemical modulation of ocean acidification in the central North Pacific. Proc. Natl. Acad. Sci. **106**: 12235–12240. doi:10.1073/pnas.0906044106

Dore, J. E., R. Lukas, D. W. Sadler, and D. M. Karl. 2003. Climate-driven changes to the atmospheric CO2 sink in the subtropical North Pacific Ocean. Nature **424**: 754–757. doi:10.1038/nature01841.1.

Doyle, S. M., E. A. Whitaker, V. De Pascuale, T. L. Wade, A. H. Knap, P. H. Santschi, A. Quigg, and J. B. Sylvan. 2018. Rapid formation of microbe-oil aggregates and changes in community composition in coastal surface water following exposure to oil and the dispersant corexit. Front. Microbiol. **9**: 1–16. doi:10.3389/fmicb.2018.00689

Drenkard, E. J., A. L. Cohen, D. C. McCorkle, S. J. de Putron, V. R. Starczak, and A. E. Zicht. 2013. Calcification by juvenile corals under heterotrophy and elevated CO2. Coral Reefs **32**: 727–735. doi:10.1007/s00338-013-1021-5

Edmunds, P. J. 2011. Zooplanktivory ameliorates the effects of ocean acidification on the reef coral Porites spp. Limnol. Oceanogr. **56**: 2402–2410. doi:10.4319/lo.2011.56.6.2402

Edwards, G. 1971. Geology of the West Flower Garden Bank.

Enochs, I. C., D. P. Manzello, G. Kolodziej, S. H. C. Noonan, L. Valentino, and K. E.

Fabricius. 2016. Enhanced macroboring and depressed calcification drive net dissolution at high-CO2coral reefs. Proc. R. Soc. B Biol. Sci. **283**: 0–7. doi:10.1098/rspb.2016.1742

Eyre, B. D., T. Cyronak, P. Drupp, E. H. De Carlo, J. P. Sachs, and A. J. Andersson. 2018. Coral reefs will transition to net dissolving before end of century. Science (80-.). **911**: 908–911. doi:10.1126/science.aao1118

Fabricius, K. E., A. Genin, and Y. Benayahu. 1995. Flow-dependent herbivory and growth in zoxanthellae-free soft corals. Limnol. Oceanogr. **40**: 1290–1301.

Falter, J. L., R. J. Lowe, M. J. Atkinson, and P. Cuet. 2012. Seasonal coupling and de-coupling of net calcification rates from coral reef metabolism and carbonate chemistry at Ningaloo Reef, Western Australia. J. Geophys. Res. Ocean. **117**: C05003. doi:10.1029/2011JC007268

Feely, R. A., S. C. Doney, and S. R. Cooley. 2009. Present Conditions and Future Changes in a High CO2 World. Oceanography **22**: 36–47. doi:10.5670/oceanog.2009.95

Feely, R. a, C. L. Sabine, K. Lee, W. Berelson, J. Kleypas, V. J. Fabry, F. J. Millero, and Anonymous. 2004. Impact of anthropogenic CO2 on the CaCO3 system in the oceans. Science (80-.). **305**: 362–366. doi:10.1126/science.1097329

Ferrier-Pagès, C., J. Witting, E. Tambutté, and K. P. Sebens. 2003. Effect of natural zooplankton feeding on the tissue and skeletal growth of the scleractinian coral Stylophora pistillata. Coral Reefs **22**: 229–240. doi:10.1007/s00338-003-0312-7

Fox, M. D., G. J. Williams, M. D. Johnson, and others. 2018. Gradients in Primary

Production Predict Trophic Strategies of Mixotrophic Corals across Spatial Scales. Curr. Biol. 1–9. doi:10.1016/j.cub.2018.08.057

G.Fichot, C., S. E.Lohrenz, and R. Benner. 2014. Journal of Geophysical Research : Oceans. J. Geophys. Res. Ocean. **119**: 1176–1194. doi:10.1002/2013JC009424.Received

Gajdzik, L., and T. DeCarlo. 2017. The perfect calm: Reoccurring mass die-offs on a remote coral atoll. Matters. doi:10.19185/matters.201707000003

Gardner, T. A., I. M. Côté, J. A. Gill, A. Grant, and A. R. Watkinson. 2003. Long-Term Region-Wide Declines in Caribbean Corals. Science (80-.). **301**: 958–960. doi:10.1126/science.1086050

Gattuso, J.-P., M. Pichon, B. Delesalle, C. Canon, and M. Frankignoulle. 1996. Carbon fluxes in coral reefs. I. Lagrangian measurement of community metabolism and resulting air-sea CO 2 disequilibrium. Mar. Ecol. Prog. Ser. **145**: 109–121.

Georgian, S. E., D. Deleo, A. Durkin, C. E. Gomez, M. Kurman, J. J. Lunden, and E. E. Cordes. 2016. Oceanographic patterns and carbonate chemistry in the vicinity of cold-water coral reefs in the Gulf of Mexico: Implications for resilience in a changing ocean. Limnol. Oceanogr. **61**: 648–665. doi:10.1002/lno.10242

Gillies, L. E., J. C. Thrash, S. deRada, N. N. Rabalais, and O. U. Mason. 2015. Archaeal enrichment in the hypoxic zone in the northern Gulf of Mexico: Archaea in the hypoxic northern GOM water column. Environ. Microbiol. **17**: 3847–3856. doi:10.1111/1462-2920.12853

Gledhill, D. K., R. Wanninkhof, F. K. Millero, and M. Eakin. 2008. Ocean acidification

of the Greater Caribbean Region 1996-2006. J. Geophys. Res. Ocean. **113**: 1–11. doi:10.1029/2007JC004629

Gledhill, D., R. Wanninkhof, and C. M. Eakin. 2009. Observing Ocean Acidification from Space. Oceanography **22**: 48–59. doi:10.5670/oceanog.2009.96

Grottoli, A. G., L. J. Rodrigues, and J. E. Palardy. 2006. Heterotrophic plasticity and resilience in bleached corals. Nature **440**: 1186–1189. doi:10.1038/nature04565

Hagman, D. K., and S. R. Gittings. 1992. Coral bleaching on high latitude reefs at the Flower Garden Banks, NW Gulf of Mexico. Proceeding Seventh Int. Coral Reef Symp. **1**: 38–43.

Ho, D. T., C. S. Law, M. J. Smith, P. Schlosser, M. Harvey, and P. Hill. 2006. Measurements of air-sea gas exchange at high wind speeds in the Southern Ocean: Implications for global parameterizations. Geophys. Res. Lett. **33**: 1–6. doi:10.1029/2006GL026817

Hoegh-Guldberg, O., P. J. Mumby, A. J. Hooten, and others. 2007. Coral reefs under rapid climate change and ocean acidification. Science **318**: 1737–1742. doi:10.1126/science.1152509

Holmes, I., K. Harris, and C. Quince. 2012. Dirichlet multinomial mixtures: Generative models for microbial metagenomics. PLoS One **7**. doi:10.1371/journal.pone.0030126

Houlbrèque, F., and C. Ferrier-Pagès. 2009. Heterotrophy in tropical scleractinian corals. Biol. Rev. **84**: 1–17. doi:10.1111/j.1469-185X.2008.00058.x

Hu, X., M. F. Nuttall, H. Wang, and others. 2018. Seasonal variability of carbonate

chemistry and decadal changes in waters of a marine sanctuary in the Northwestern Gulf of Mexico. Mar. Chem. 0–1. doi:10.1016/j.marchem.2018.07.006

Huang, W.-J., W.-J. Cai, Y. Wang, S. E. Lohrenz, and M. C. Murrell. 2015a. The carbon dioxide system on the Mississippi River-dominated continental shelf in the northern Gulf of Mexico: 1. Distribution and air-sea CO2 flux. J. Geophys. Res. Ocean. 1–17. doi:10.1002/2014JC010498.Received

Huang, W. J., W. J. Cai, R. M. Castelao, Y. Wang, and S. E. Lohrenz. 2013. Effects of a wind-driven cross-shelf large river plume on biological production and CO2 uptake on the Gulf of Mexico during spring. Limnol. Oceanogr. **58**: 1727–1735. doi:10.4319/lo.2013.58.5.1727

Huang, W. J., W. J. Cai, Y. Wang, and others. 2015b. The response of inorganic carbon distributions and dynamics to upwelling-favorable winds on the northern Gulf of Mexico during summer. Cont. Shelf Res. **111**: 211–222. doi:10.1016/j.csr.2015.08.020

Hughes, T. P., J. T. Kerry, M. Álvarez-Noriega, and others. 2017. Global warming and recurrent mass bleaching of corals. Nature **543**: 373–377. doi:10.1038/nature21707

Johannes, R., J. Alberts, C. DElia, and others. 1972. The metabolism of some coral reef communities: a team study of nutrient and energy flux at Eniwetok. Bioscience **22**: 541–543. doi:10.1525/bio.2010.60.10.17

Johnson, Z. I., E. R. Zinser, A. Coe, N. P. McNulty, E. M. S. Woodward, and S. W. Chisholm. 2006. Niche Partitioning Among Prochlorococcus Ecotypes Along Ocean-Scale Environmental Gradients. Science (80-.). **311**: 1737–1740.

doi:10.1126/science.1118052

Johnston, M. 2018. 2016 Flower Garden Banks Localized Mortality Event Mini-Symposium Report.

Johnston, M. A., M. Nuttall, R. Eckert, J. Embesi, N. Slowey, E. Hickerson, and G. Schmahl. 2013a. Long-term Monitoring at the East and West Flower Garden Banks National Marine Sanctuary, 2009-2010, US Department of the Interior, Bureau of Ocean Energy Management, Gulf of Mexico OCS Region.

Johnston, M. A., M. F. Nuttall, R. J. Eckert, J. A. Embesi, N. C. Slowey, E. L. Hickerson, and G. P. Schmahl. 2013b. Long-Term Monitoring at the East and West Flower Garden Banks National Marine Sanctuary , 2009 – 2010 Volume 1 : Technical Report Long-Term Monitoring at the East and West Flower Garden Banks National Marine Sanctuary , 2009 – 2010 Volume 1 : Technical Re. **1**: 2009–2010.

Jokiel, P. L. 1991. Illustrated Scientific Guide To Kane'Ohe Bay, Oahu.

Jokiel, P. L. 2011. Ocean acidification and control of reef coral calcification by boundary layer limitation of proton flux. Bull. Mar. Sci. **87**: 639–657. doi:10.5343/bms.2010.1107

Karl, D. M., R. R. Bidigare, and R. M. Letelier. 2001. Long-term changes in plankton community structure and productivity in the North Pacific Subtropical Gyre: The domain shift hypothesis. Deep Sea Res. Part II Top. … **48**: 1449–1470. doi:10.1016/S0967-0645(00)00149-1

Keul, N., J. W. Morse, R. Wanninkhof, D. K. Gledhill, and T. S. Bianchi. 2010.

Carbonate chemistry dynamics of surface waters in the Northern Gulf of Mexico. Aquat. Geochemistry **16**: 337–351. doi:10.1007/s10498-010-9091-2

Kleypas, J. A., J. W. Mcmanus, and L. A. B. Menez. 1999. Environmental Limits to Coral Reef Development : Where Do We Draw the Line ? Am. Zool. **39**: 146–159.

Kohler, K. E., and S. M. Gill. 2006. Coral Point Count with Excel extensions (CPCe): A Visual Basic program for the determination of coral and substrate coverage using random point count methodology. Comput. Geosci. **32**: 1259–1269. doi:10.1016/j.cageo.2005.11.009

Kundu, P. K., and R. C. Beardsley. 1991. Evidence of a critical Richardson number in moored measurements during the upwelling season off northern California. J. Geophys. Res. **96**: 4855–4868.

de la Moriniere, E. C., I. Nagelkerken, G. van der Velde, B. J. a. Pollux, M. a. Hemminga, and a. H. L. Huiskes. 2003. Ontogenetic dietary changes of coral reef fishes in the mangrove-seagrass-reef continuum: stable isotopes and gut- content analysis. Mar. Ecol. Prog. Ser. **246**: 279–289. doi:10.3354/meps246279

Langdon, C., and M. J. Atkinson. 2005. Effect of elevated pCO2on photosynthesis and calcification of corals and interactions with seasonal change in temperature/ irradiance and nutrient enrichment. J. Geophys. Res. C Ocean. **110**: 1–16. doi:10.1029/2004JC002576

Langdon, C., T. Takahashi, C. Sweeney, D. Chipman, and J. Atkinson. 2000. Effect of calcium carbonate saturation state on the calcification rate of an experiemental coral reef. Global Biogeochem. Cycles **14**: 639–654.

Laurent, A., K. Fennel, W. J. Cai, W. J. Huang, L. Barbero, and R. Wanninkhof. 2017. Eutrophication-induced acidification of coastal waters in the northern Gulf of Mexico: Insights into origin and processes from a coupled physical-biogeochemical model. Geophys. Res. Lett. **44**: 946–956. doi:10.1002/2016GL071881

Leal, M. C., C. Ferrier-Pagès, R. Calado, M. E. Thompson, M. E. Frischer, and J. C. Nejstgaard. 2013. Coral feeding on microalgae assessed with molecular trophic markers. Mol. Ecol. **23**: 3870–3876. doi:10.1111/mec.12486

Leichter, J. J., G. Shellenbarger, S. J. Genovese, and S. R. Wing. 1998. Breaking internal waves on a Florida (USA) coral reef: A plankton pump at work? Mar. Ecol. Prog. Ser. **166**: 83–97. doi:10.3354/meps166083

Levitus, S., J. Antonov, T. Boyer, and C. Stephens. 2000. Warming of the world ocean. Science (80-.). **287**: 2225–2229. doi:10.1029/2004GL021592

Li, Y., W. Nowlin, and R. Reid. 1997. Mean hydrographic fields and their interannual variability over the Texas-Louisiana continental shelf in spring, summer, and fall. J. Geophys. Res. … **102**: 1027–1049. doi:10.1029/96JC03210

Lohrenz, S. E., and W.-J. Cai. 2006. Satellite ocean color assessment of air-sea fluxes of CO_2 in a river-dominated coastal margin. Geophys. Res. Lett. **33**: n/a-n/a. doi:10.1029/2005GL023942

Lohrenz, S. E., W. J. Cai, F. Chen, X. Chen, and M. Tuel. 2010. Seasonal variability in air-sea fluxes of CO2 in a river-influenced coastal margin. J. Geophys. Res. Ocean. **115**: 1–13. doi:10.1029/2009JC005608

Lohrenz, S. E., G. L. Fahnenstiel, D. G. Redalje, G. A. Lang, X. Chen, and M. J. Dagg.

1997. Variations in primary production of northern Gulf of Mexico continental shelf waters linked to nutrient inputs from the Mississippi River. Mar. Ecol. Prog. Ser. **155**: 45–54.

Lowe, R. J., J. L. Falter, S. G. Monismith, and M. J. Atkinson. 2009. A numerical study of circulation in a coastal reef-lagoon system. J. Geophys. Res. Ocean. **114**: 1–18. doi:10.1029/2008JC005081

Martens-Habbena, W., P. M. Berube, H. Urakawa, J. R. de la Torre, and D. A. Stahl. 2009. Ammonia oxidation kinetics determine niche separation of nitrifying Archaea and Bacteria. Nature **461**: 976–979. doi:10.1038/nature08465

Mehrbach, C., C. H. Culberson, J. E. Hawley, and R. M. Pytkowicx. 1973. Measurement of the apparent dissociation constants of carbonic acid in seawater at atmospheric pressure. Limnol. Oceanogr. **18**: 897–907. doi:10.4319/lo.1973.18.6.0897

Moberg, F., and C. Folke. 1999. Ecological goods and services of coral reef ecosystems. Ecol. Econ. **29**: 215–233. doi:10.1016/S0921-8009(99)00009-9

Monismith, S. G., K. A. Davis, G. G. Shellenbarger, and others. 2010. Flow effects on benthic grazing on phytoplankton by a Caribbean reef. Limnol. Oceanogr. **55**: 1881–1892. doi:10.4319/lo.2010.55.5.1881

Morrison, J. M., W. J. Merrell, R. M. Key, and T. C. Key. 1983. Property distributions and deep chemical measurements within the western Gulf of Mexico. J. Geophys. Res. Ocean. **88**: 2601–2608. doi:10.1029/JC088iC04p02601

Muscatine, L., L. R. McCloskey, and R. E. Marian. 1981. Estimating the daily constribution of carbon om zooxanthellae to coral animal respiration. Limnol.

Oceanogr. **26**: 601–611.

National Marine Fisheries Service. 2017. Fisheries Economics of the United States, 2015.

Nelson, H. R., and A. H. Altieri. 2019. Oxygen : the universal currency on coral reefs. Coral Reefs. doi:10.1007/s00338-019-01765-0

North, G. R., T. L. Bell, and R. F. Cahalan. 1982. Sampling Errors in the Estimation of Empirical Orthogonal Funtions. Mon. Weather Rev. **110**: 699–706. doi:10.1175/1520-0493(1982)110<0699:SEITEO>2.0.CO;2

Nowlin Jr, W., A. Jochens, R. O. Reid, and S. F. Dimarco. 1998. Texas-Louisiana shelf circulation and transport processes study: synthesis report, US Department of the Interior, Minerals Management Service, Gulf of Mexico OCS Region.

Nowlin, W. D., A. E. Jochens, S. F. Dimarco, R. O. Reid, and M. K. Howard. 2005. Low-frequency circulation over the Texas-Louisiana continental shelf, p. 219–240. *In* W. Sturges and A. Lugo-Fernandez [eds.], CIrculation of the Gulf of Mexico: Observations and Models. Geophysical Monograph Series.

Odum, H. T., and E. P. Odum. 1955. Trophic Structure and Productivity of a Windward Coral Reef Community on Eniwetok Atoll. Ecol. Monogr. **25**: 291–320. doi:10.2307/1943285

Pacanowski, R. C., and S. G. H. Philander. 1981. Parameterization of vertical mixing in numerical models of tropical oceans. J. Phys. Oceanogr. **11**: 1443–1451.

Pandolfi, J. M., R. H. Bradbury, E. Sala, and others. 2003. Global Trajectories of the Long-Term Decline of Coral Reef Ecosystems. Science (80-.). **301**: 955–958.

doi:10.1126/science.1085706

Parada, A. E., and J. A. Fuhrman. 2017. Marine archaeal dynamics and interactions with the microbial community over 5 years from surface to seafloor. ISME J. **11**: 2510–2525. doi:10.1038/ismej.2017.104

Partensky, F., J. Blanchot, and D. Vaulot. 1999. Differential distribution and ecology of Prochlorococcus and Synechococcus in oceanic waters: a review. Bull. Oceanogr. MONACO-NUMERO Spec. 457–476.

Patten, N. L., A. S. J. Wyatt, R. J. Lowe, and A. M. Waite. 2011. Uptake of picophytoplankton, bacterioplankton and virioplankton by a fringing coral reef community (Ningaloo Reef, Australia). Coral Reefs **30**: 555–567. doi:10.1007/s00338-011-0777-8

Pierrot, D., E. Lewis, and D. Wallace. 2006. MS Excel program developed for CO2 system calculations. ORNL/CDIAC-105a. Carbon Dioxide Inf. Anal. Center, Oak Ridge Natl. Lab. US Dep. Energy, Oak Ridge, Tennessee.

Pierrot, D., C. Neill, K. Sullivan, and others. 2009. Recommendations for autonomous underway pCO2 measuring systems and data-reduction routines. Deep. Res. Part II Top. Stud. Oceanogr. **56**: 512–522. doi:10.1016/j.dsr2.2008.12.005

Polovina, J. J., E. A. Howell, and M. Abecassis. 2008. Ocean's least productive waters are expanding. Geophys. Res. Lett. **35**. doi:10.1029/2007GL031745

Le Quéré, C., R. M. Andrew, P. Friedlingstein, and others. 2018. Global Carbon Budget 2017. Earth Syst. Sci. Data **10**: 405–448. doi:10.5194/essd-10-405-2018

Rabalais, N. N., R. E. Turner, B. K. Sen Gupta, D. F. Boesch, P. Chapman, and M. C.

Murrell. 2007. Hypoxia in the northern Gulf of Mexico: Does the science support the plan to reduce, mitigate, and control hypoxia? Estuaries and Coasts **30**: 753–772. doi:10.1007/BF02841332

Rabalais, N. N., R. E. Turner, and W. J. Wiseman. 2002. Gulf of Mexico Hypoxia, A.K.A. "The Dead Zone." Annu. Rev. Ecol. Syst. **33**: 235–263. doi:10.1146/annurev.ecolsys.33.010802.150513

Raymont, J., J. Burton, and D. KR. 1980. Plankton and productivity in the oceans, 2nd ed. Pergamon Press.

Reimer, J., H. Wang, R. Vargas, and W. Cai. 2017. Multidecadal fCO2 increase along the United States southeast coastal margin. J. Geophys. Res. **122**: 61–72. doi:10.1002/2017JC013170

Rezak, R., S. R. Gittings, and T. J. Bright. 1990. Biotic Assemblages and Ecological Controls on Reefs and Banks of the Northwest Gulf of Mexico. Integr. Comp. Biol. **30**: 23–35. doi:10.1093/icb/30.1.23

Ribes, M., R. Coma, M. J. Atkinson, and R. A. Kinzie. 2003. Particle removal by coral reef communities: picoplankton is a major source of nitrogen. Mar. Ecol. Ser. **257**: 13–23. doi:10.3354/meps257013

Riebesell, U., I. Zondervan, B. Rost, P. Tortell, R. Zeebe, and F. Morel. 2000. Reduced calcification of marine plankton in response to increased atmospheric CO 2. Nature **407**: 2–5. doi:10.1038/35030078

Robbins, L. L., K. L. Daly, L. Barbero, and others. 2018. Spatial and temporal variability of pCO2, carbon fluxes and saturation state on the West Florida Shelf. J. Geophys.

Res. Ocean. **123**. doi:10.1029/2018JC014195

Robbins, L., R. Wanninkhof, L. Barbero, and others. 2014. Chapter 4: Air-Sea Exchange, p. 17–23. *In* H. Benway and P. Coble [eds.], Report of the Gulf of Mexico Coastal Carbon Synthesis Workship. Ocean Carbon and Biogeochemistry Program and North American Carbon Program.

Roder, C., L. Fillinger, C. Jantzen, G. M. Schmidt, S. Khokiattiwong, and C. Richter. 2010. Trophic response of Corals to large amplitude internal waves. Mar. Ecol. Prog. Ser. **412**: 113–128. doi:10.3354/meps08707

Rodrigues, L. J., and A. G. Grottoli. 2006. Calcification rate and the stable carbon, oxygen, and nitrogen isotopes in the skeleton, host tissue, and zooxanthellae of bleached and recovering Hawaiian corals. Geochim. Cosmochim. Acta **70**: 2781–2789. doi:10.1016/j.gca.2006.02.014

Sargent, M., and T. Austin. 1949. Organic productivity of an Atoll. EOS, Trans. Am. Geophys. Union **30**: 245–249.

Sarmiento, J. L., and N. Gruber. 2006. Ocean biogeochemical dynamics, Princeton University Press.

Sarmiento, J. L., N. Gruber, A. Brzezinski, and J. P. Dunne. 2004. High latitude controls of thermohaline nutrients and low latitude biological productivity. Nature **427**: 56–60. doi:10.1038/nature02204.1.

Scavia, D., J. C. Field, D. F. Boesch, and others. 2002. Climate change impacts on US coastal and marine ecosystems [Review]. Estuaries **25**: 149–164. doi:10.1007/BF02691304

Sebens, K. P., S. P. Grace, B. Helmuth, E. J. Maney, and J. S. Miles. 1998. Water fow and prey capture by three scleractinian corals, Madracis mirabilis, Montastrea cavernosa and Porites porites, in a field enclosure. Mar. Biol. 347–360.

Sebens, K. P., and A. S. Johnson. 1991. Effects of water movement on prey capture and distribution of reef corals *. Hydrobiologia **226**: 91–101. doi:10.1007/BF00006810

Shamberger, K. E. F., R. A. Feely, C. L. Sabine, M. J. Atkinson, E. H. DeCarlo, F. T. Mackenzie, P. S. Drupp, and D. A. Butterfield. 2011. Calcification and organic production on a Hawaiian coral reef. Mar. Chem. **127**: 64–75. doi:10.1016/j.marchem.2011.08.003

Shamberger, K. E. F., S. J. Lentz, and A. L. Cohen. 2018. Low and variable ecosystem calcification in a coral reef lagoon under natural acidification. Limnol. Oceanogr. **63**: 714–730. doi:10.1002/lno.10662

Shaw, E. C., S. R. Phinn, B. Tilbrook, and A. Steven. 2015. Natural in situ relationships suggest coral reef calcium carbonate production will decline with ocean acidification. Limnol. Oceanogr. **60**: 777–788. doi:10.1002/lno.10048

Silverman, J., B. Lazar, L. Cao, K. Caldeira, and J. Erez. 2009. Coral reefs may start dissolving when atmospheric CO2 doubles. Geophys. Res. Lett. **36**: 1–5. doi:10.1029/2008GL036282

Smith, S. V., and J. A. Marsh. 1973. Organic production on the windward reef flat of Eniwetok Atoll. Limnol. Oceanogr. **18**: 953–961. doi:10.4319/lo.1973.18.6.0953

Spalding, M. D., and A. M. Grenfell. 1997. New estimates of global and regional coral reef areas. Coral Reefs **16**: 225–230. doi:10.1007/s003380050078

Stewart, F. J., O. Ulloa, and E. F. DeLong. 2012. Microbial metatranscriptomics in a permanent marine oxygen minimum zone: OMZ community gene expression. Environ. Microbiol. **14**: 23–40. doi:10.1111/j.1462-2920.2010.02400.x

Takahashi, T., J. G. Goddard, and D. W. Chipman. 1993. Seasonal Variation of CO2 and Nutrients in the High-Latitude Surface Oceans: A Comparative Study. New York **7**: 843–878.

Takahashi, T., S. C. Sutherland, C. Sweeney, and others. 2002. Global sea-air CO_2 flux based on climatological surface ocean pCO_2, and seasonal biological and temperature effects. Deep. Res. Part II Top. Stud. Oceanogr. **49**: 1601–1622. doi:10.1016/S0967-0645(02)00003-6

Takahashi, T., S. C. Sutherland, R. Wanninkhof, and others. 2009. Climatological mean and decadal change in surface ocean pCO2, and net sea-air CO2flux over the global oceans. Deep. Res. Part II Top. Stud. Oceanogr. **56**: 554–577. doi:10.1016/j.dsr2.2008.12.009

Teague, W. J., H. W. Wijesekera, E. Jarosz, D. B. Fribance, A. Lugo-Fernández, and Z. R. Hallock. 2013. Current and hydrographic conditions at the East Flower Garden Bank in 2011. Cont. Shelf Res. **63**: 43–58. doi:10.1016/j.csr.2013.04.039

Thomson, R., and W. Emery. 2014. Data Analysis Methods in Physical Oceangraphy, 3rd Editio. Elsevier Science.

Thyng, K., C. Greene, R. Hetland, H. Zimmerle, and S. DiMarco. 2016. True Colors of Oceanography: Guidelines for Effective and Accurate Colormap Selection. Oceanography **29**: 9–13. doi:10.5670/oceanog.2016.66

Tolar, B. B., G. M. King, and J. T. Hollibaugh. 2013. An Analysis of Thaumarchaeota Populations from the Northern Gulf of Mexico. Front. Microbiol. **4**. doi:10.3389/fmicb.2013.00072

Wang, Z. A., R. Wanninkhof, W.-J. Cai, R. H. Byrne, X. Hu, T.-H. Peng, and W.-J. Huang. 2013a. The marine inorganic carbon system along the Gulf of Mexico and Atlantic coasts of the United States: Insights from a transregional coastal carbon study. Limnol. Oceanogr. **58**: 325–342. doi:10.4319/lo.2013.58.1.0325

Wang, Z. A., R. Wanninkhof, W. J. Cai, R. H. Byrne, X. Hu, T. H. Peng, and W. J. Huang. 2013b. The marine inorganic carbon system along the Gulf of Mexico and Atlantic coasts of the United States: Insights from a transregional coastal carbon study. Limnol. Oceanogr. **58**: 325–342. doi:10.4319/lo.2013.58.1.0325

Wanninkhof, R. 1992. Relationship between wind speed and gas exchange over the ocean. J. Geophys. Res. **97**: 7373–7382.

Wanninkhof, R., L. Barbero, R. Byrne, W. J. Cai, W. J. Huang, J. Z. Zhang, M. Baringer, and C. Langdon. 2015. Ocean acidification along the Gulf Coast and East Coast of the USA. Cont. Shelf Res. **98**: 54–71. doi:10.1016/j.csr.2015.02.008

Weiss, R. F. 1974. Carbon dioxide in water and seawater: the solubility of a non-ideal gas. Mar. Chem. **2**: 203–215.

Weiss, R. F., and B. A. Price. 1980. Nitrous Oxide Solubility in Water and Seawater. Mar. Chem. **8**: 347–359.

WHP. 1994. WHP 91-1: World Ocean Circulation Experiment Operations Manual.

Wyatt, A. S. J., R. J. Lowe, S. Humphries, and A. M. Waite. 2010. Particulate nutrient

fluxes over a fringing coral reef: Relevant scales of phytoplankton Production and mechanisms of supply. Mar. Ecol. Prog. Ser. **405**: 113–130. doi:10.3354/meps08508

Wyatt, A. S. J., R. J. Lowe, S. Humphries, and A. M. Waite. 2013. Particulate nutrient fluxes over a fringing coral reef: Source-sink dynamics inferred from carbon to nitrogen ratios and stable isotopes. Limnol. Oceanogr. **58**: 409–427. doi:10.4319/lo.2013.58.1.0409

Xue, Z., R. He, K. Fennel, W.-J. Cai, S. Lohrenz, W.-J. Huang, and H. Tian. 2016. Modeling pCO2 variability in the Gulf of Mexico. Biogeosciences Discuss. **11**: 12673–12695. doi:10.5194/bgd-11-12673-2014

Xue, Z., R. He, K. Fennel, W. J. Cai, S. Lohrenz, and C. Hopkinson. 2013. Modeling ocean circulation and biogeochemical variability in the Gulf of Mexico. Biogeosciences **10**: 7219–7234. doi:10.5194/bg-10-7219-2013

Yahel, G., A. Post, K. Fabricius, D. Marie, D. Vaulot, and A. Genin. 1998. Phytoplankton distribution and grazing near coral reefs. Limnol. Oceanogr. 551–563. doi:10.4319/lo.1998.43.4.0551

Yates, K., and R. Halley. 2006. CO32- concentration and pCO2 thresholds for calcification and dissolution on the Molokai reef flat, Hawaii. Biogeosciences Discuss. 123–154.

Yeakel, K. L., A. J. Andersson, N. R. Bates, T. J. Noyes, A. Collins, and R. Garley. 2015. Shifts in coral reef biogeochemistry and resulting acidification linked to offshore productivity. Proc. Natl. Acad. Sci. **112**: 14512–14517.

doi:10.1073/pnas.1507021112

Zhang, W., R. Hetland, S. DiMarco, and K. Fennel. 2015. Processes controlling mid-water column oxygen minima over the Texas-Louisiana shelf. J. Geophys. Res. Ocean. **120**: 28002812. doi:10.1002/2015JC010769.Received

Zhang, X., R. D. Hetland, M. Marta-Almeida, and S. F. Dimarco. 2012a. A numerical investigation of the Mississippi and Atchafalaya freshwater transport, filling and flushing times on the Texas-Louisiana Shelf. J. Geophys. Res. Ocean. **117**: 1–21. doi:10.1029/2012JC008108

Zhang, X., M. Marta-Almeida, and R. D. Hetland. 2012b. A high-resolution pre-operational forecast model of circulation on the Texas-Louisiana continental shelf and slope. J. Oper. Oceanogr. **5**: 19–34. doi:10.1080/1755876X.2012.11020129

Zhang, Z., and R. Hetland. 2012. A numerical study on convergence of alongshore flows over the Texas-Louisiana shelf. J. Geophys. Res. Ocean. **117**: 1–18. doi:10.1029/2012JC008145

Zwirglmaier, K., L. Jardillier, M. Ostrowski, and others. 2008. Global phylogeography of marine Synechococcus and Prochlorococcus reveals a distinct partitioning of lineages among oceanic biomes. Environ. Microbiol. **10**: 147–161. doi:10.1111/j.1462-2920.2007.01440.x

APPENDIX A

SUPPLEMENTARY FIGURES

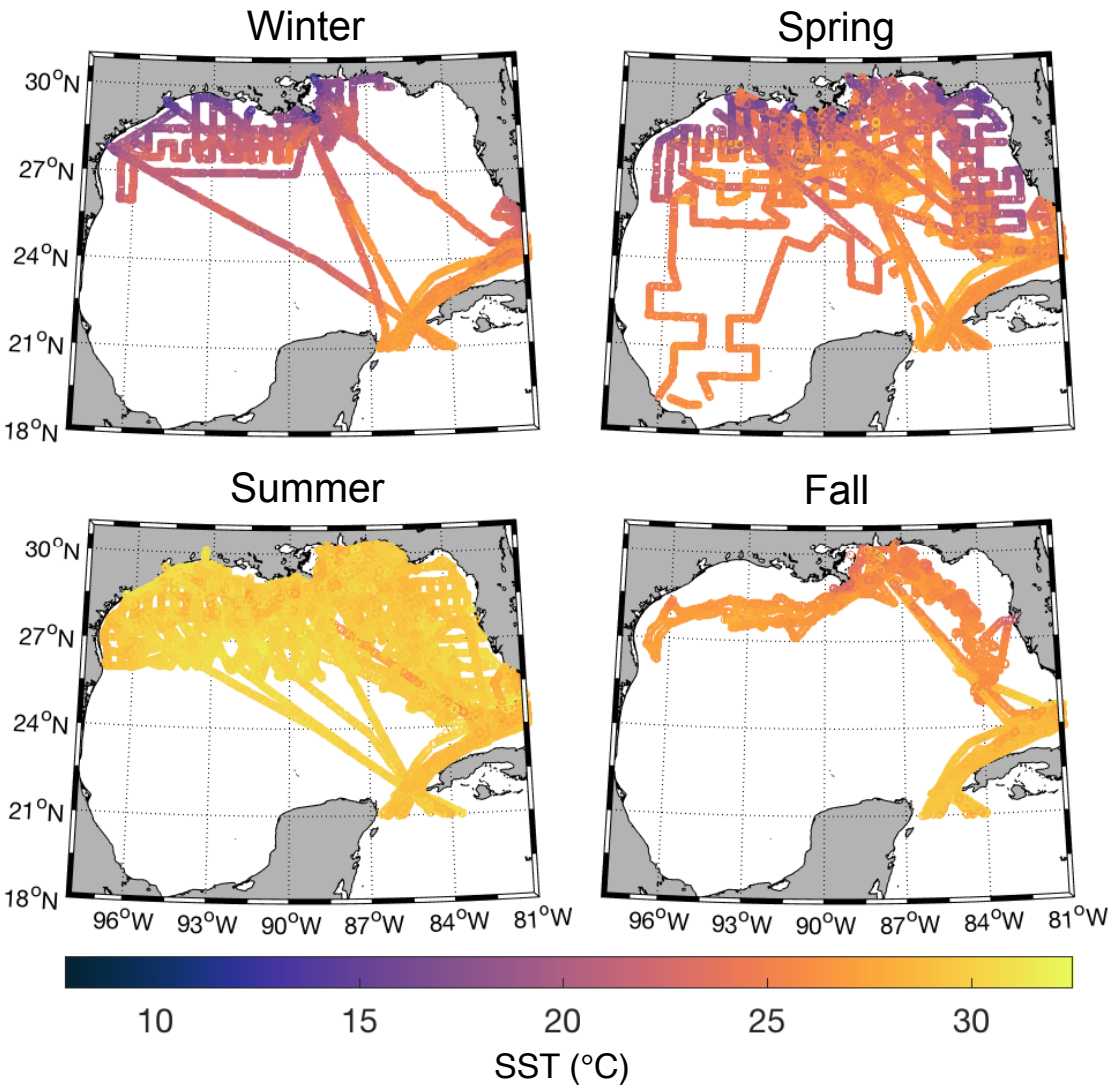

FIG A-1: Seasonal surface seawater temperatures (°C).

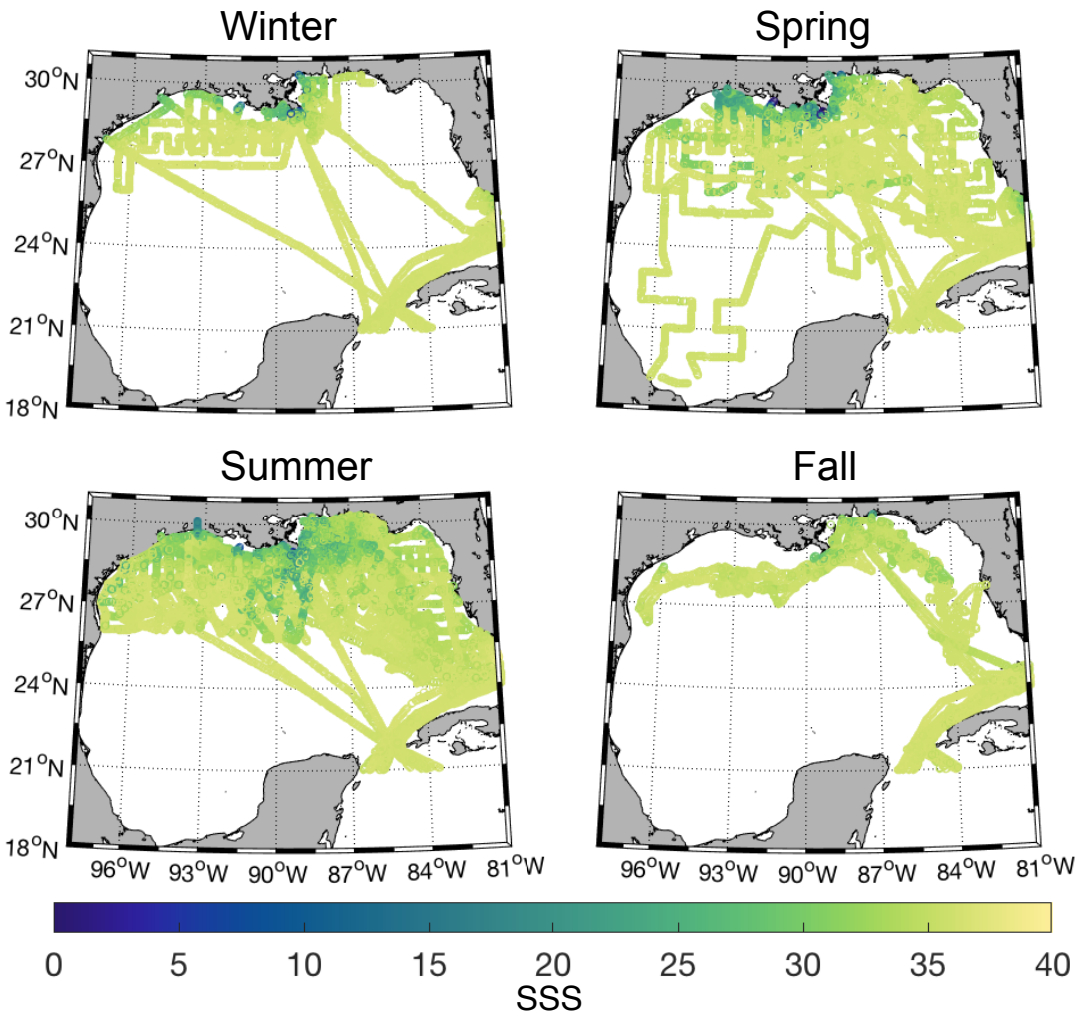

FIG A-2: Seasonal sea surface salinity (SSS).

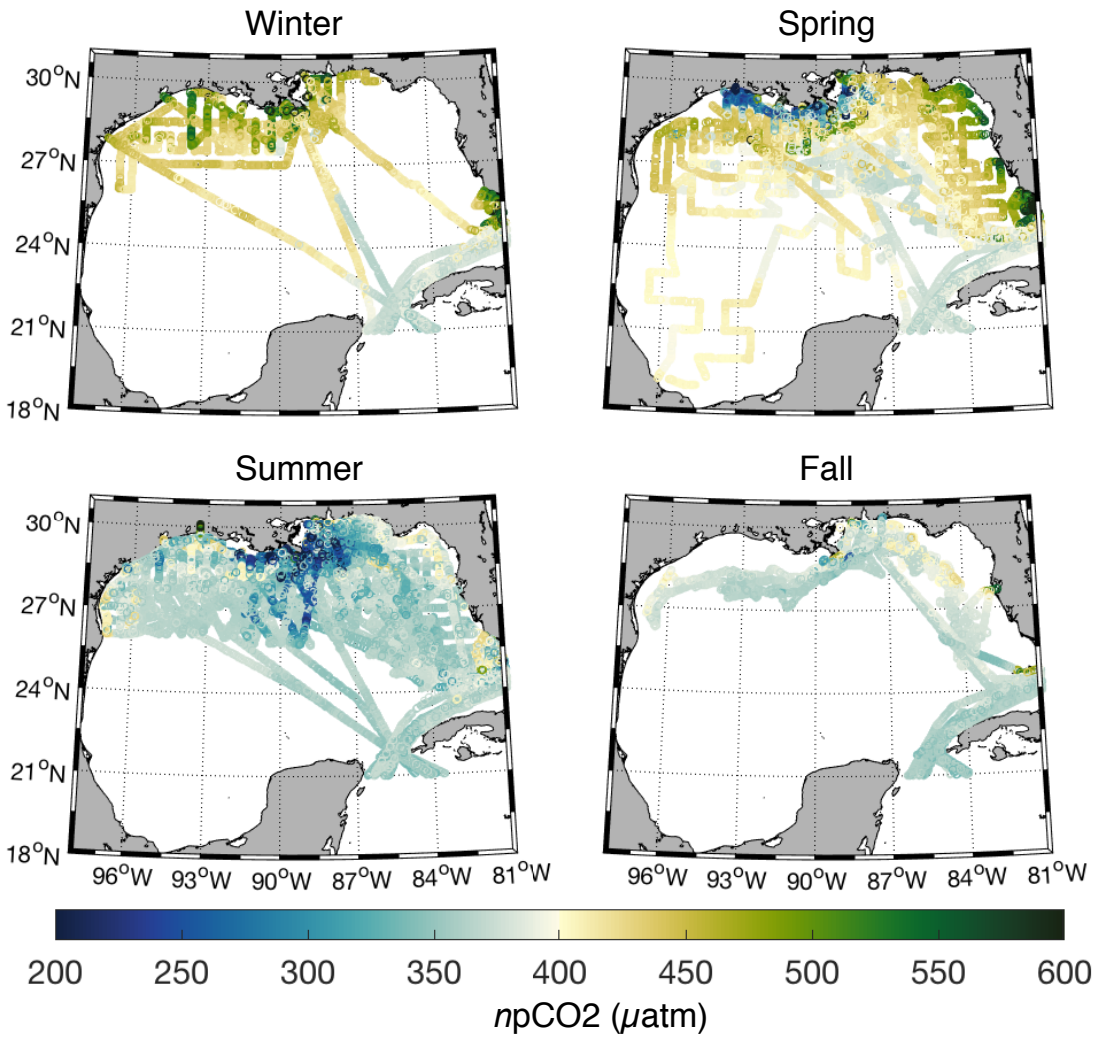

FIG A-3: Temperature-normalized surface seawater CO_2 (µatm) during winter, spring, summer and fall. Note that the actual minimum and maximum values are 64 and 2989 µatm, respectively.

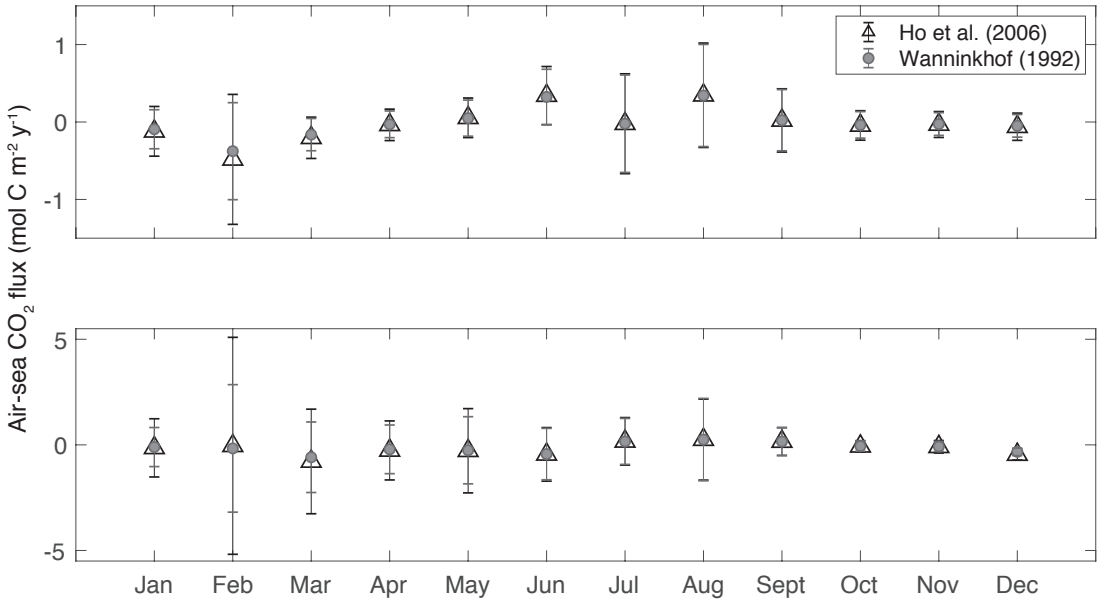

FIG A-4: Monthly average (± std) air-sea CO_2 fluxes in the open (top panel) and coastal (bottom panel) ocean for the wind speed parameterization of Ho et al. (2006) (triangles) and Wanninkhof et al. (1992) (circles).

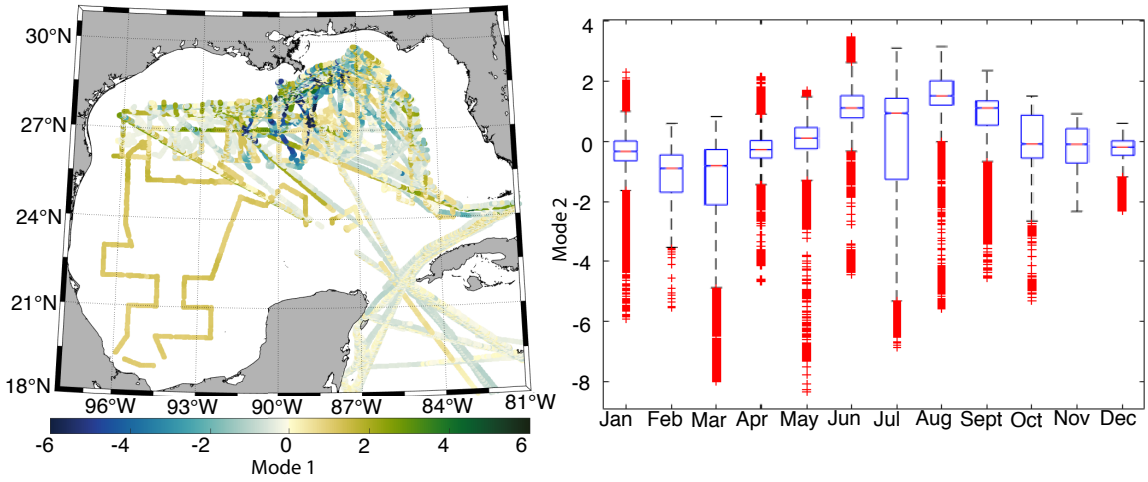

FIG A-5: Open ocean spatial pattern showing scores of Mode 1 (left) and open ocean seasonal pattern showing scores of Mode 2 (right). In the box plot, the central red line is the median and the outer edges of the box represent the 25th and 75th percentiles. Whiskers extend to the most extreme points that are not considered outliers, and the outliers are plotted in red (+).

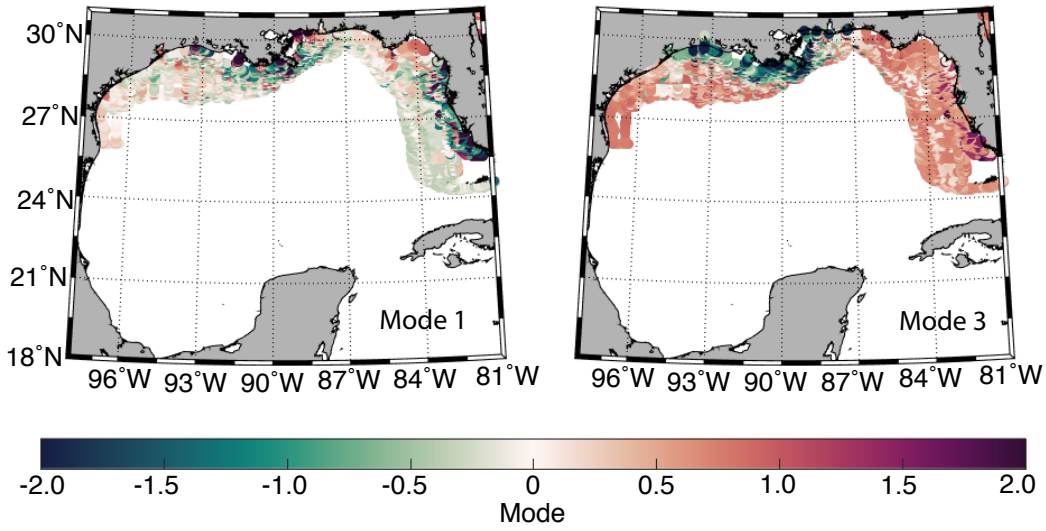

FIG A-6: Coastal ocean spatial patterns in Mode 1 (left panel) and Mode 3 (right panel). The color bar represents the scores of the EOF.

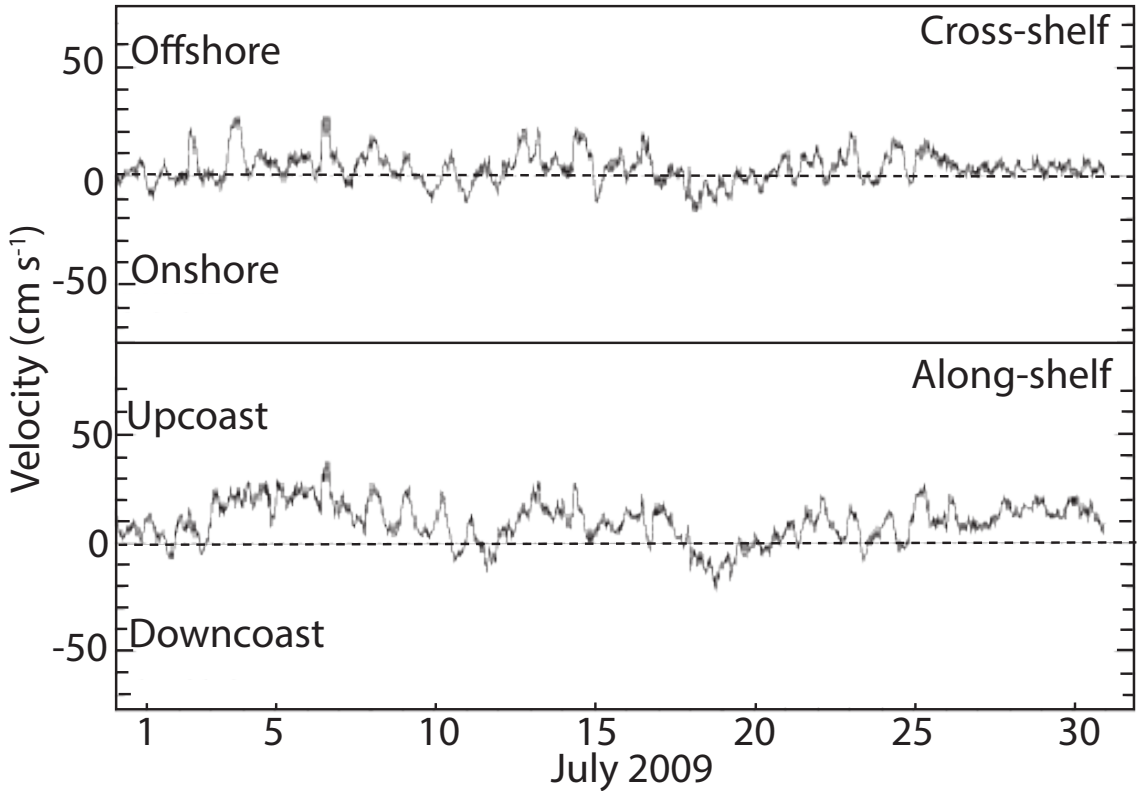

FIG A-7: Cross-shelf (top panel) and along-shelf (bottom panel) currents collected at Texas Automated Buoy System (TABS) Buoy R located in the northern GoM (29° 38.100 N, 93° 38.502 W) during July 2009. Upcoast is eastward and downcoast is westward.

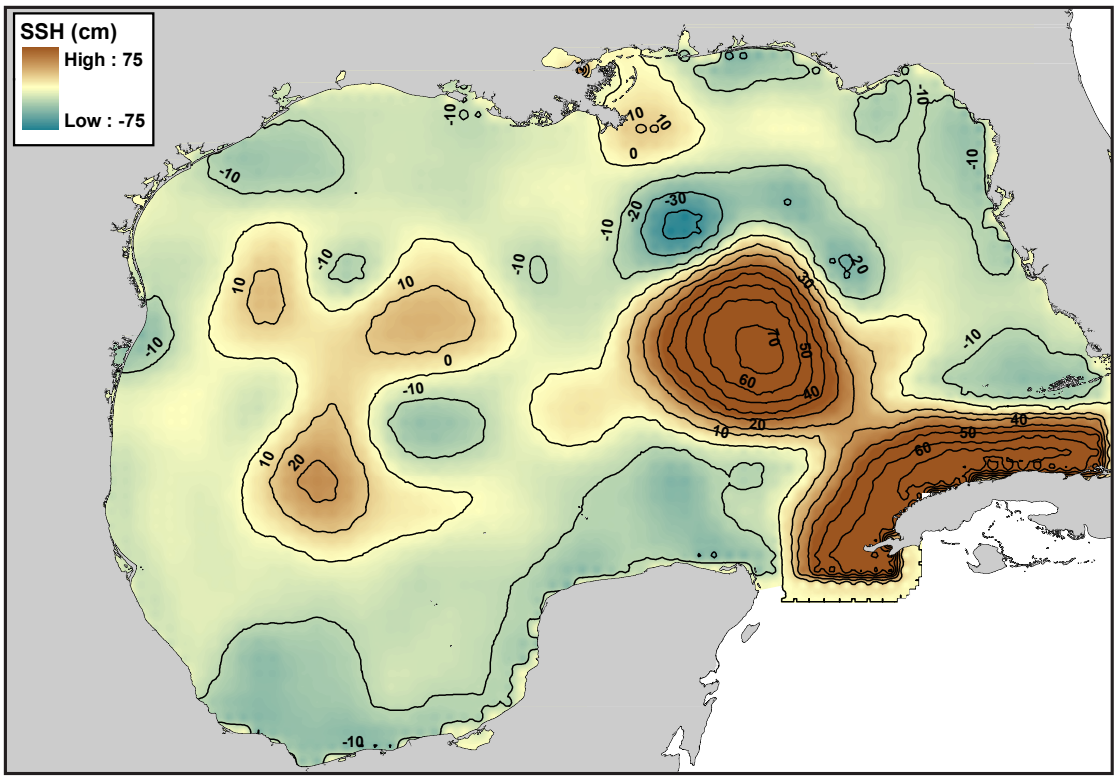

FIG A-8: Sea surface height anomalies (cm) in the Gulf of Mexico on 07/20/2009. These data were obtained from the Colorado Center for Astrodynamics Research (CCAR). Note there are no data for Caribbean waters.

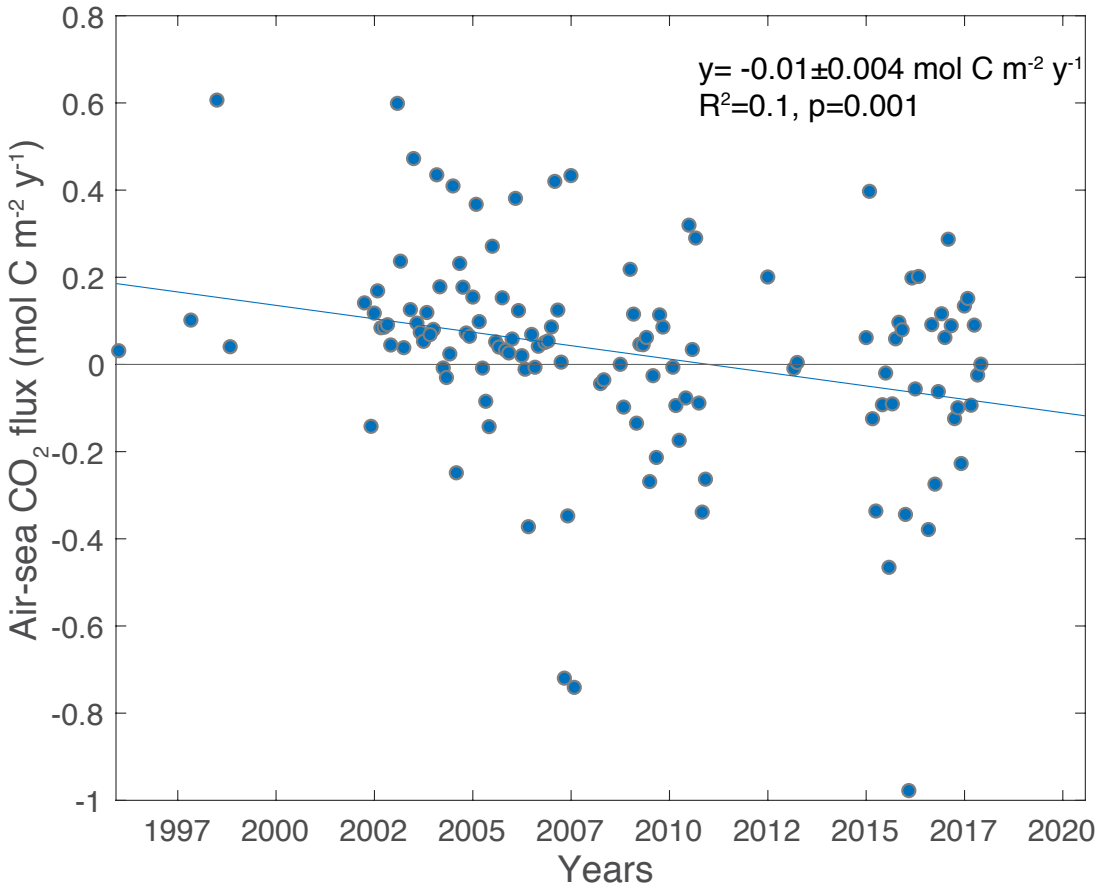

FIG A-9: Deseasonalized monthly open ocean air-sea CO_2 flux (mol C m^{-2} y^{-1}) in the GoM (1996-2017). Statistics are shown for the blue line, which represents the air-sea CO_2 flux trend. The black line is a refence for air-sea CO_2 flux equal to 0.

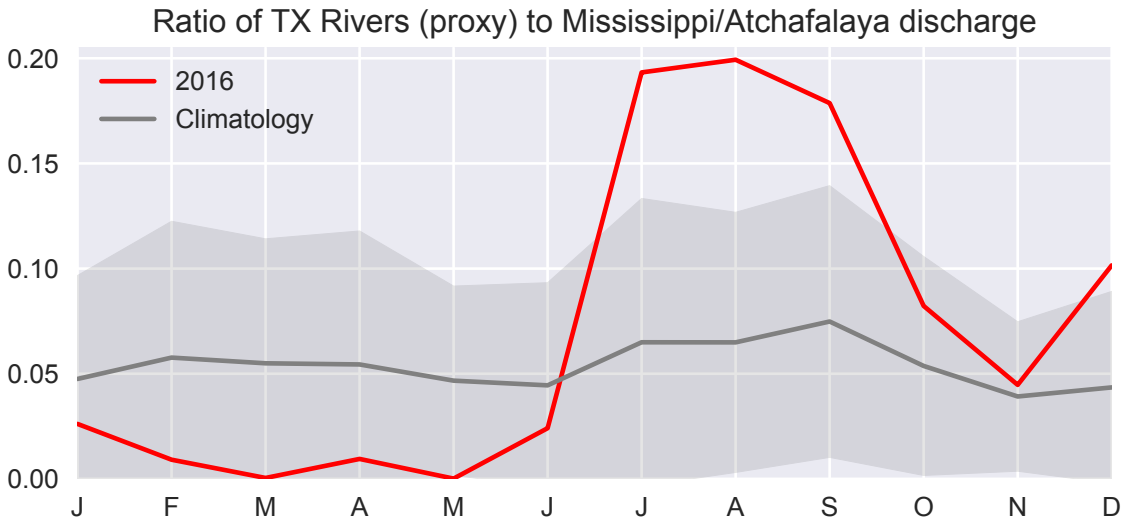

FIG A-10: A timeseries of the monthly mean ratio of Mississippi/Atchafalaya river water to Texas river water is plotted for 2016 (red) and a climatology based on the entire record for each river gauge (grey with standard deviation shaded). Higher values indicate relatively more Texas river water, as compared to Mississippi/Atchafalaya river water, reached the FGB National Marine Sanctuary.

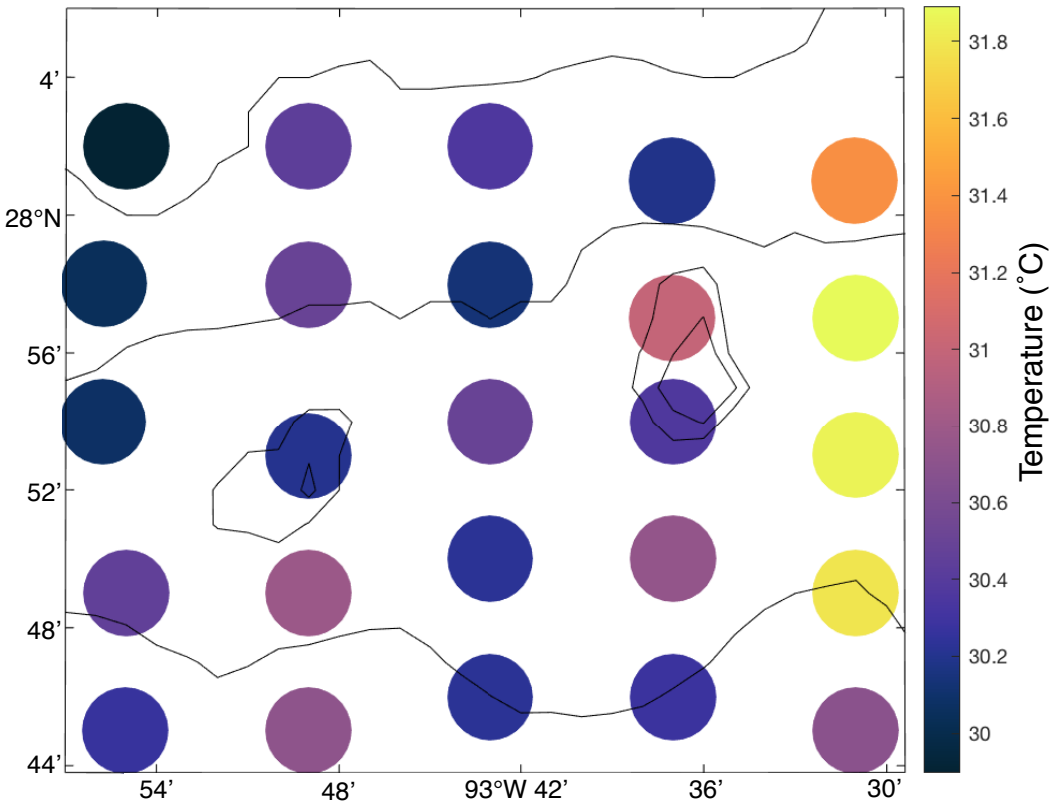

FIG A-11: Sea surface temperature (°C) at each station during the Flower Garden Banks Rapid Response cruise.

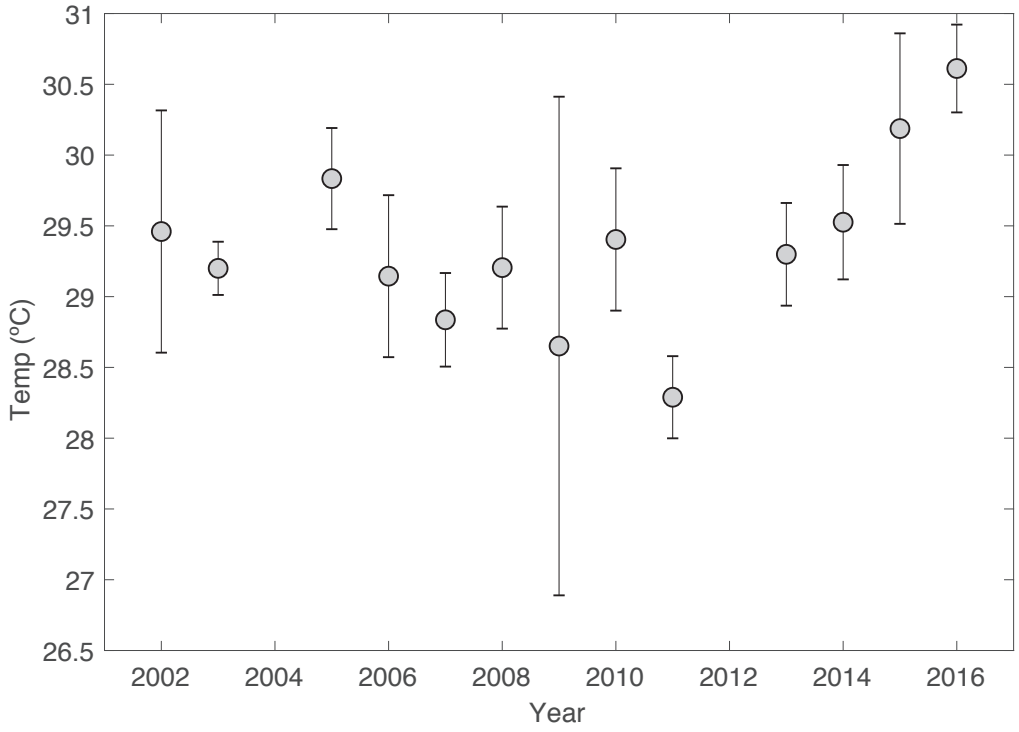

FIG A-12: Average July sea surface temperatures (±1 std dev) at Buoy V for the years 2002-2016.

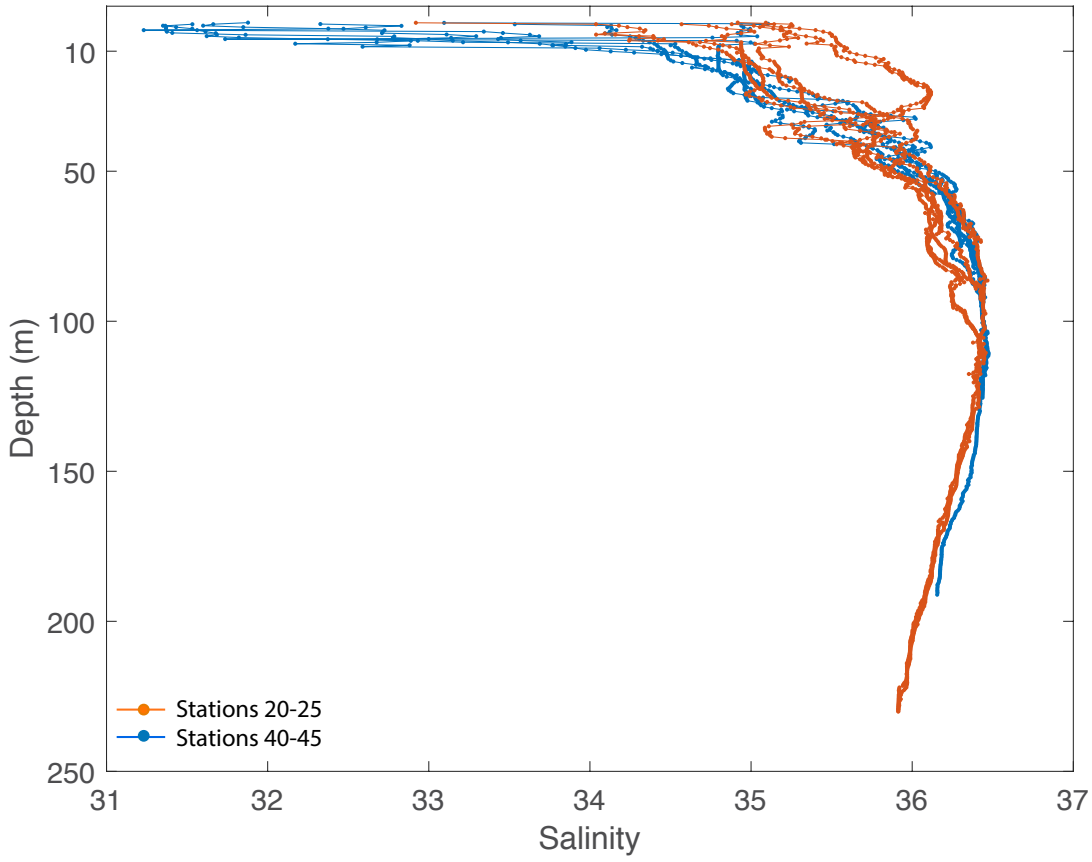

FIG A-13: CTD salinity over the WB transect (stations 20-25) and EB transect (stations 40-45).

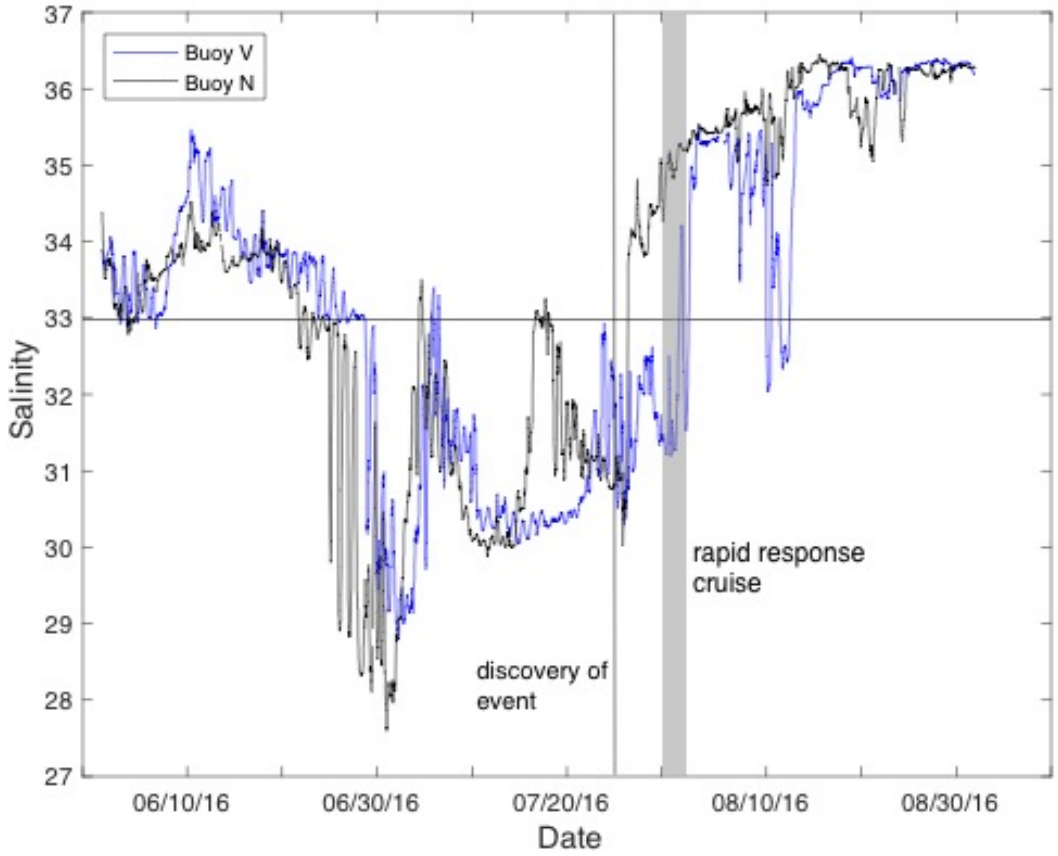

FIG A-14: Sea surface salinity at Buoy V (blue line) located near the EB and Buoy N (black line) located near the WB. Salinity lower than 33 indicates river-influenced water.

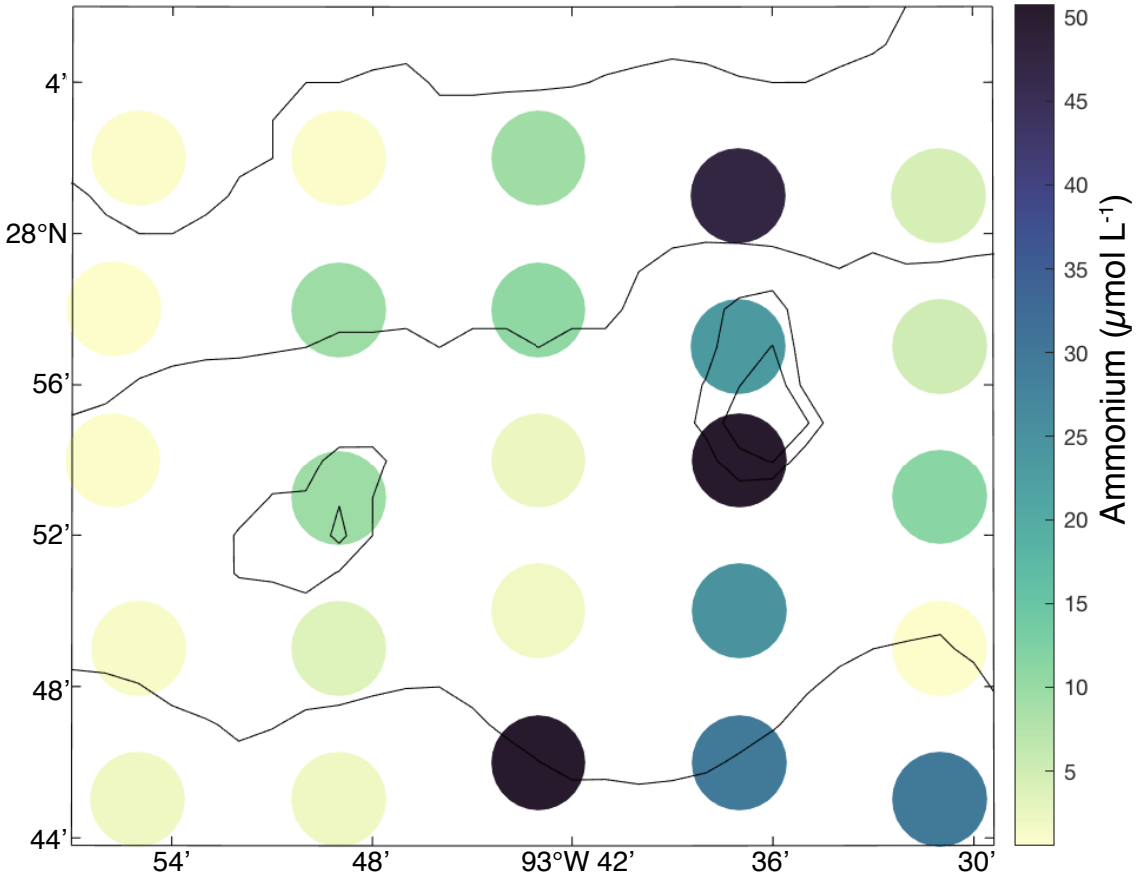

FIG A-15: Surface seawater ammonium concentrations (μmol L^{-1}) at each station during the Flower Garden Banks Rapid Response cruise.

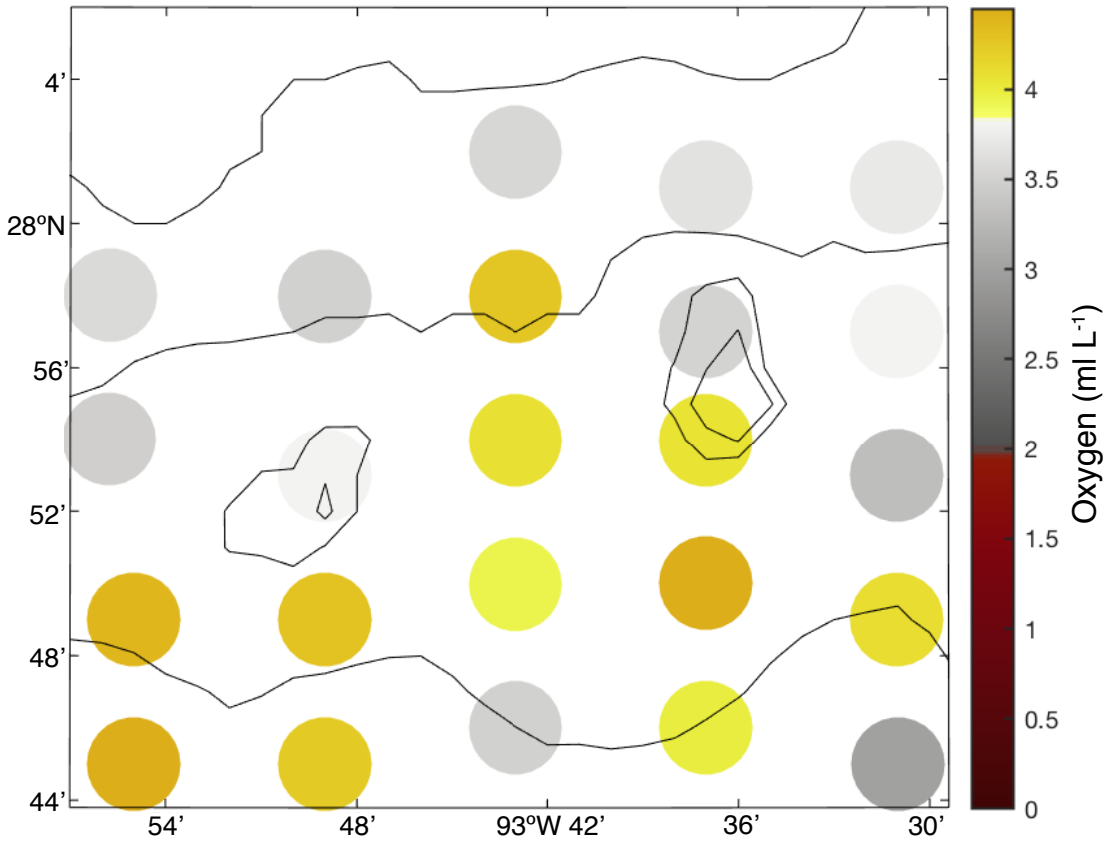

FIG A-16: Oxygen concentrations (ml L^{-1}) at 75 m depth during the Flower Garden Banks Rapid Response cruise.

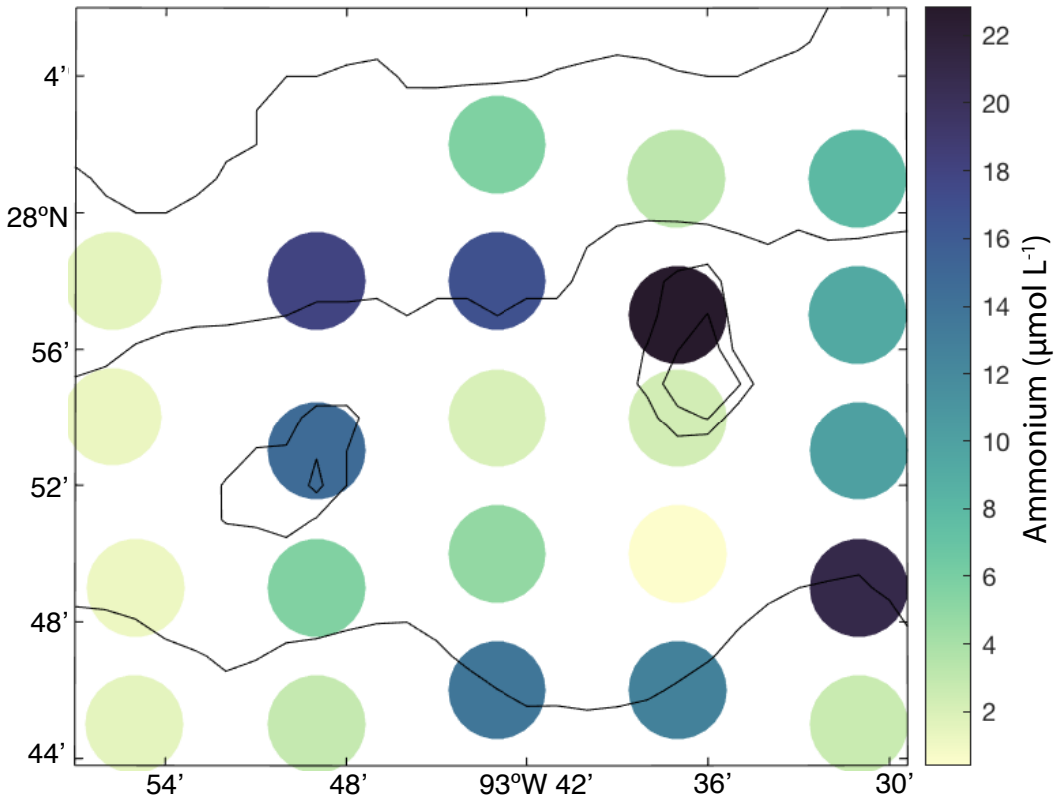

FIG A-17: Ammonium concentrations (µmol L^{-1}) at 75 m depth during the Flower Garden Banks Rapid Response cruise.

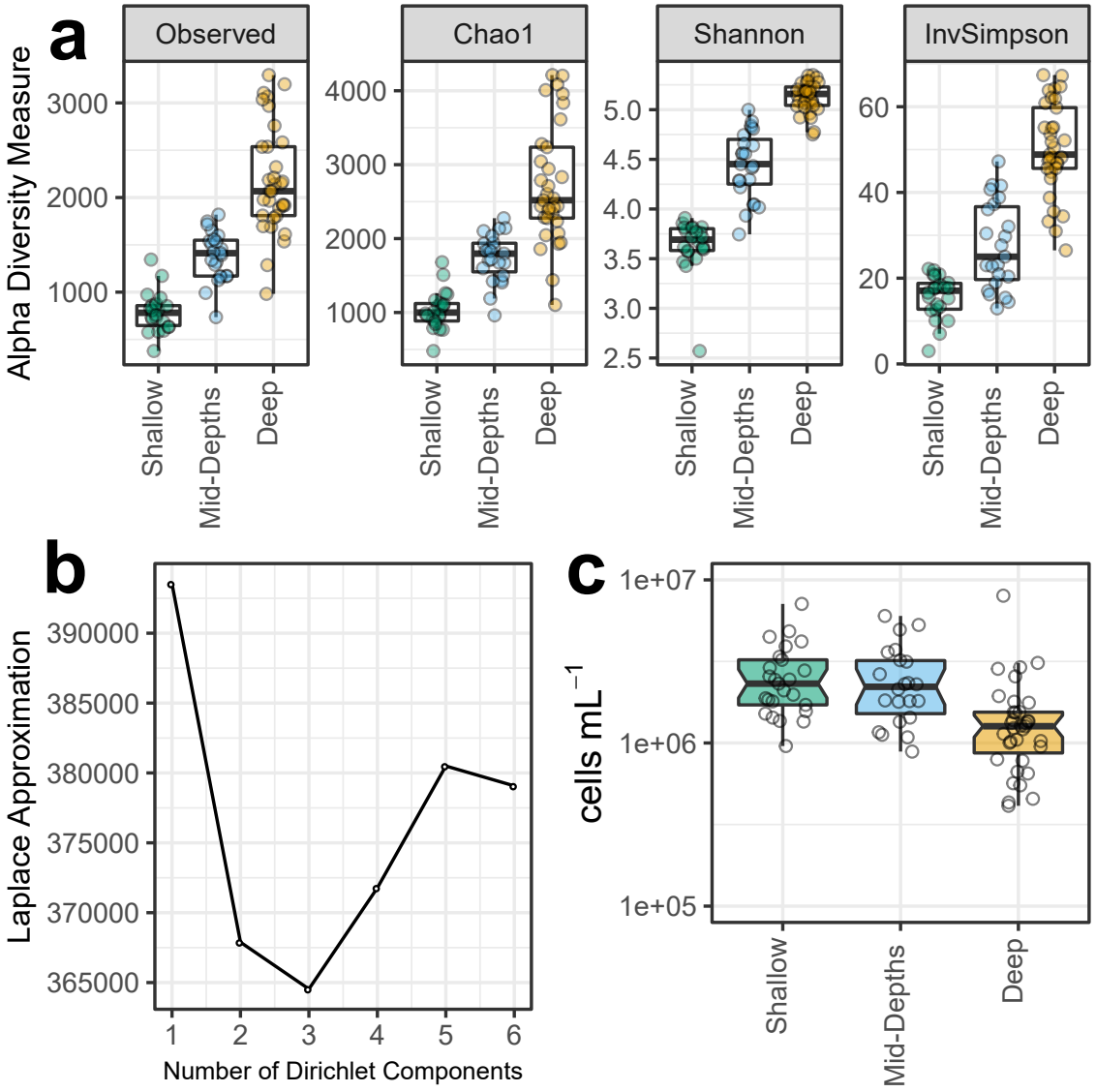

FIG A-18: (a) Boxplots of sample alpha diversity indices within each metacommunity: Number of observed OTUs (Observed), Chao1 richness index (Chao1), Shannon diversity index (Shannon), Inverse-Simpson diversity index (InvSimpson). (b) The Laplace approximation during DMM-modelling was lowest when the 16S rRNA libraries were clustered into three metacommunities. (c) Boxplot of total cell concentrations within each metacommunity.

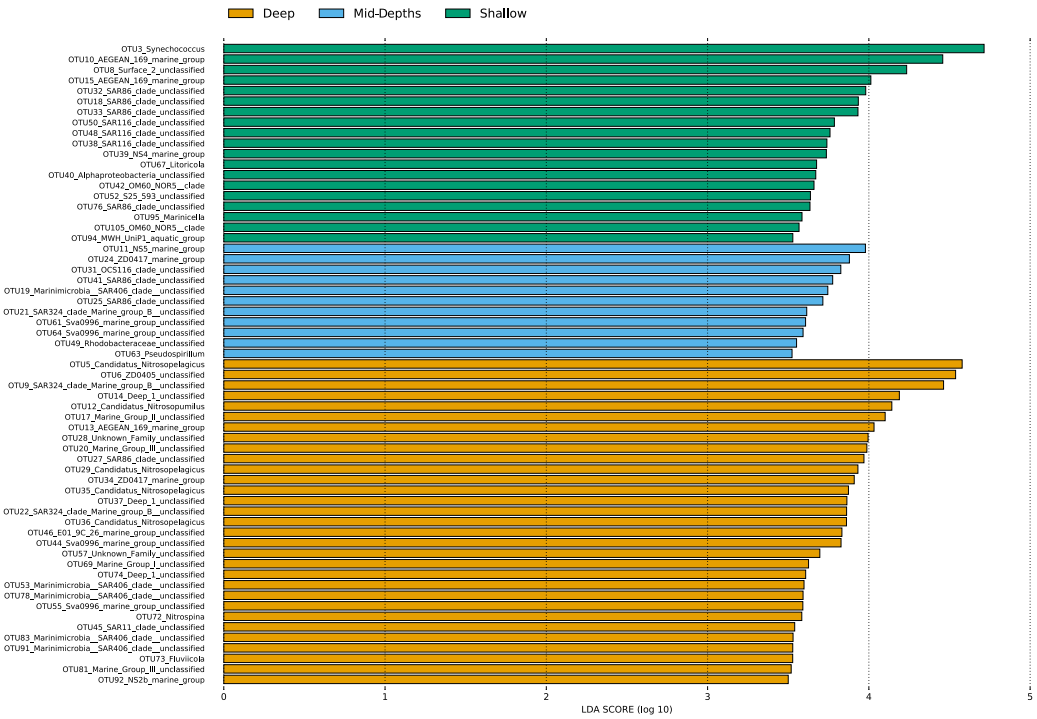

FIG A-19: Indicator taxa (OTUs) for each metacommunity as identified with a LEfSe analysis using a $\log_{10}$ LDA score threshold of 3.5. Bars represent the $\log_{10}$ transformed LDA score (effect size). Indicator OTUs have significantly enriched relative abundances in the respective metacommunities.

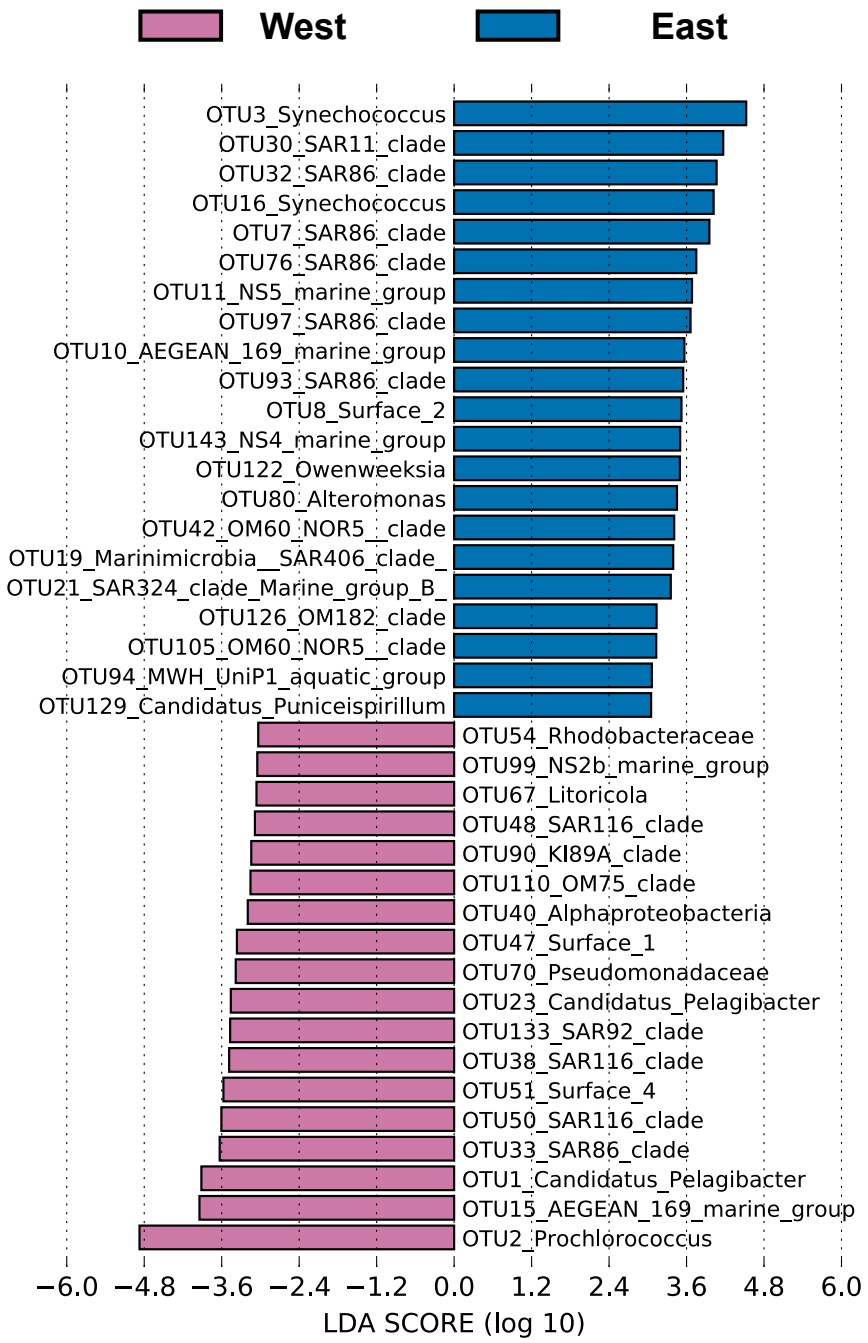

FIG A-20: Indicator taxa (OTUs) found within surface waters over the WB and EB as identified with a LEfSe analysis using a $\log_{10}$ LDA score threshold of 3.0. Bars represent the $\log_{10}$ transformed LDA score (effect size). Indicator OTUs have significantly enriched relative abundances in the respective WB or EB surface waters.

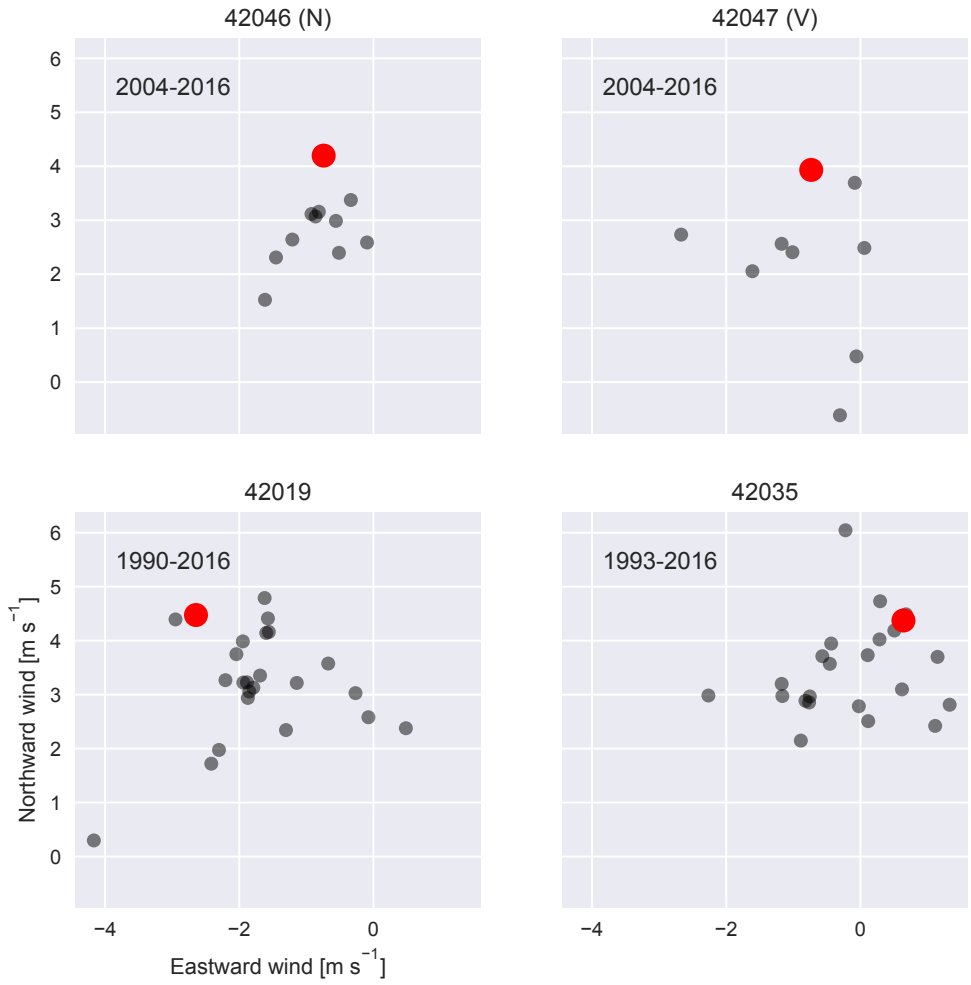

FIG A-21: Monthly mean winds in July are calculated over the historical records for four regional buoys. The data are plotted such that positive winds are blowing toward the east and north. The top two panels show wind records in the to the west (NOAA buoy 42046, also known as TABS buoy N) and east (42047, TABS V) of the FGB. The other two are along the Texas coast offshore of Matagorda Bay (42019) and Galveston Bay (42035). In each panel, 2016 is marked with a red dot, other years are black. The data show that, while there is no strong anomaly in the east-west wind, winds were more northward than typically observed, and were the strongest northward July winds in the shorter N and V records.

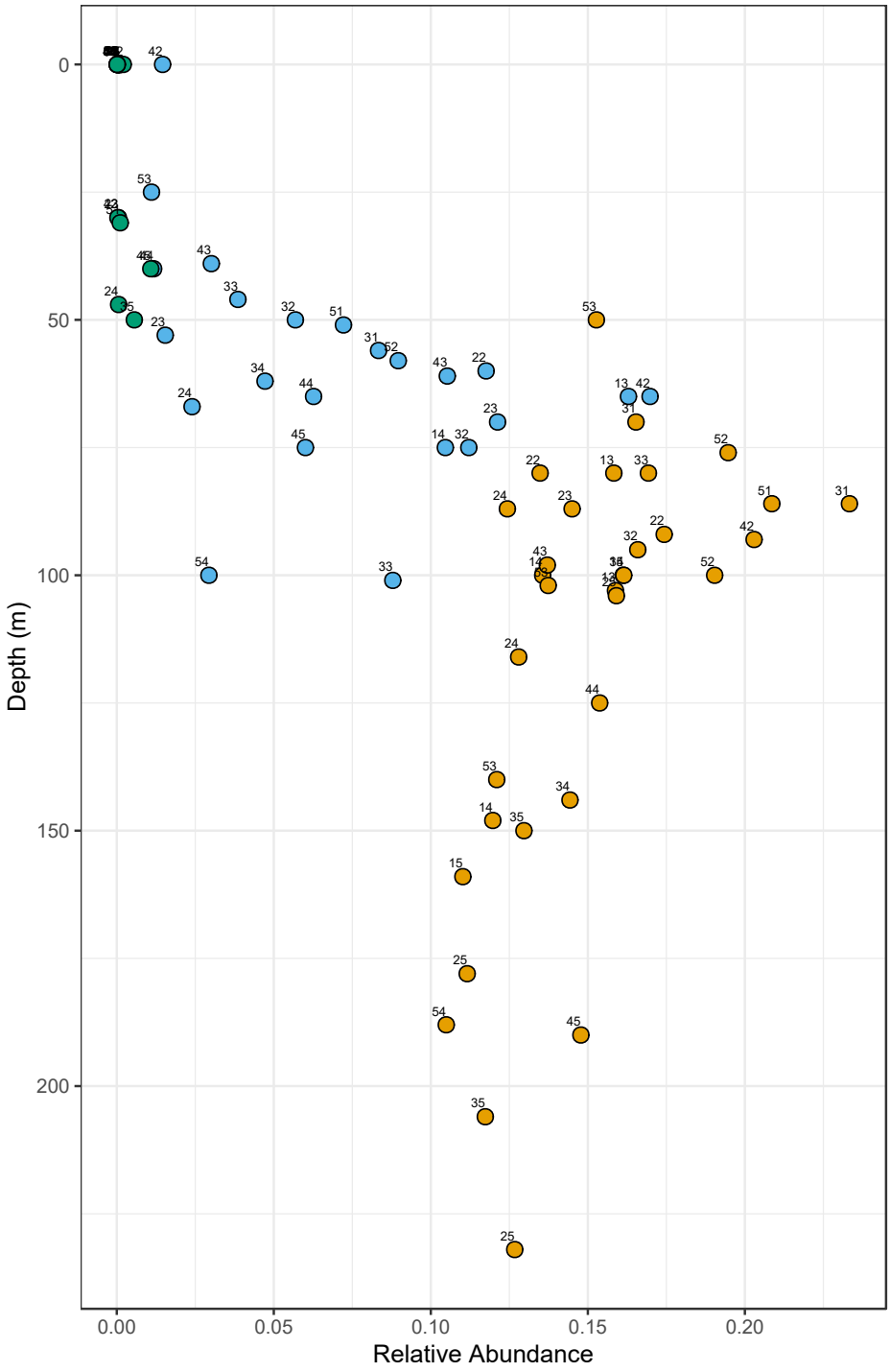

FIG A-22: The combined relative abundances of OTU5 (Nitrosopelagicus), OTU6 (uncultured marine bacterium ZD0405), and OTU9 (SAR324 clade) versus depth across all samples.

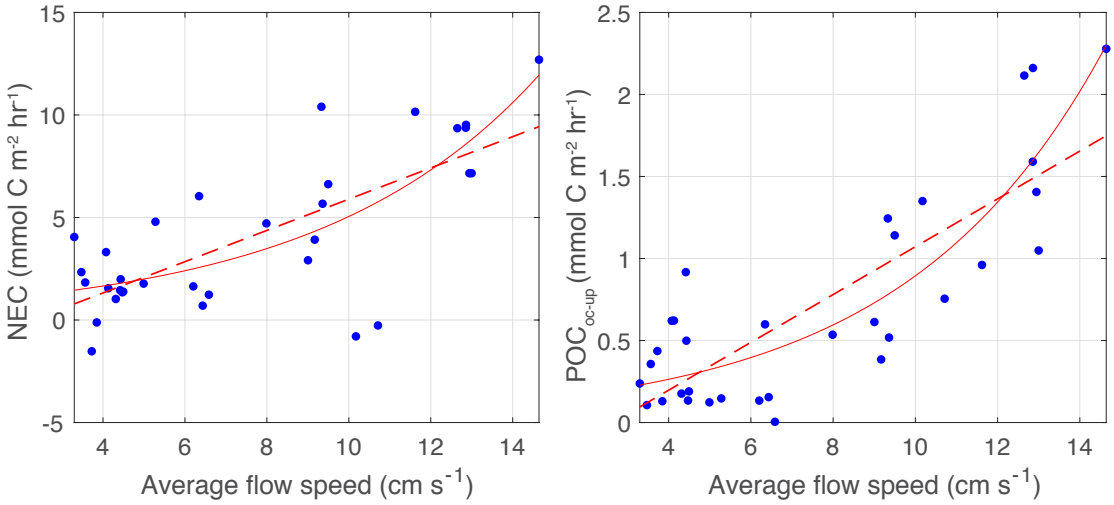

FIG A-23: The left panel shows NEC (mmol C m^{-2} hr^{-1}) and average flow speed (cm s^{-1}) with both linear (dotted red line, R^2=0.54) and exponential fits (solid red line, R^2=0.56). The right panel shows $POC_{oc\text{-}up}$ (mmol C m^{-2} hr^{-1}) and average flow speed with both linear (R^2=0.67) and exponential (R^2=0.72) fits.

APPENDIX B

SUPPLEMENTARY TABLES

Table B-1. Effects of depth, turbidity, oxygen, and salinity on microbial communities across all samples. The table shows the PERMANOVA analysis of the final stepwise CCA model generated by ordistep.

Variable	***F*(1,56)**	**R^2**	***p***	**q**
Depth	45.784	0.395	0.001	0.002
Turbidity	3.646	0.031	0.016	0.021
Oxygen	7.704	0.066	0.001	0.002
Salinity	2.871	0.025	0.032	0.032

Table B-2: Uncertainties associated with residence time (*t*, %), depth (z, m), TA (µmol kg^{-1}), DIC (µmol kg^{-1}), air-sea CO_2 flux (F, mmol C m^{-2} h^{-1}), density (ρ, kg m^{-3}), mass carbon (%), $\delta^{13}C_{op,}$ $\delta^{13}C_{2(3)}$ and $\delta^{13}C_{rf,}$ which was calculated using the standard deviation between the average (-15.87‰), assuming 100% macroalgae (-17.5‰), and 100% zooxanthellae (-14.7‰).

Deployment 1	***t***	**z**	**TAout**	**TAin**	**DICout**	**DICin**	**F**	***ρ***
NEC/NCP	±20	±0.15	±2	±2	±2.6	±2.6	±0.12	±0.29
Deployment 2								
NEC/NCP	±20	±0.15	±2	4.85	±2.6	±6.7	±0.18	±0.13
Deployment 1	***t***	**z**	**Mass C**	**$\delta^{13}C_{op}$**	**$\delta^{13}C_{2(3)}$**	**$\delta^{13}C_{rf}$**		
$POC_{oc\text{-}up}$	±20	±0.15	±0.2	±0.2	±0.2	±1.4		
Deployment 2								
$POC_{oc\text{-}up}$	±20	±0.15	±0.2	±1.64	±0.2	±1.4		

Table B-3: Average and standard deviation of NEC (mmol C m^{-2} h^{-1}) and $POC_{oc\text{-}up}$ (mmol C m^{-2} h^{-1}) at each site and during each deployment.

	Site 2 ave	**Site 3 ave**	**Total ave**	**Total range**
NEC				
Deployment 1	1.34±0.70	1.93±2.14	1.85±1.54	-1.52 to 4.05
Deployment 2	6.43±4.90	4.87±2.61	5.46±3.59	-0.80 to 12.69
$POC_{oc\text{-}up}$				
Deployment 1	0.30±0.30	0.43±0.14	0.35±0.25	0.11 to 0.92
Deployment 2	1.22±0.66	0.70±0.67	0.96±0.70	0.00 to 2.28

APPENDIX C

SUPPLEMENTARY METHODS

16S rRNA gene library curation and processing

Sequence read curation and processing were carried out using mothur v.1.39.5 (Schloss et al. 2009) following a modified version of the protocol described in Kozich et al. (2013). Paired reads were combined into contigs and quality filtered to exclude sequences containing ambiguous base calls or homopolymers runs longer than 8 bp. The merged contigs were then aligned with the SILVA non-redundant 16S rRNA reference dataset (v.123). To help mitigate the generation of spurious sequences, the aligned sequences were 'pre-clustered', allowing 1-bp difference per 100 bp of sequence (Huse et al. 2010). Chimeric sequences were identified with the VSEARCH algorithm (Rognes et al. 2016) and removed from further processing and analysis. Sequences were then clustered into Operational Taxonomic Units (OTUs) at 3% or less dissimilarity using the opticlust algorithm (Schloss and Westcott 2011). Singleton reads were not removed from the dataset. Instead, for statistical analyses requiring an OTU table, one was created by subsampling the library to the smallest sample size (20,101 sequences). Rarefied estimates of Bray-Curtis distances were calculated after 10,000 iterations. A consensus taxonomy for each OTU was assigned using a naïve Bayesian classifier (Wang et al. 2007) trained on the SILVA reference database (Quast et al. 2013) with a confidence threshold of 80%.

A total of 8,671,511 contigs distributed across 78 barcoded samples were constructed with an average read length of 253 bp. After screening of sequences with ambiguous bases or long homopolymers, 725,545 unique sequences were used to generate an alignment. Further quality control measures (i.e. pre-clustering, alignment curation, and removal of chimeric, mitochondria, chloroplast, or unclassifiable reads) reduced the total dataset to 170,256 unique contigs which clustered into 20,832 OTUs. The number of sequences in each sample ranged from 20,101 to 115,689 reads, with an average of 80,055 ± 17,101 sequences (Table S3). Rarefaction curves for all samples approached saturation, and together with high Good's Coverage values (>99%, Table S3) indicated that any undetected community members were of very low abundance.

Constrained correspondence analysis

Before the analysis, the size of the environmental dataset was reduced by using a Spearman correlation analysis to identify highly correlated ($r>|0.9|$) variables of which only one of the correlated variables was retained. Second, redundant variables, identified by having variance inflation factors >10, were removed from the analysis. Finally, environmental variables were then selected using the *ordistep* function in the "vegan" R package. The significance of the final model and fitted variables was then tested using the *anova.cca* function with 1000 permutations. For this analysis, OTU abundances were log transformed ($\ln(x+1)$) to reduce the effect of outliers and environmental parameters were log-transformed and normalized (z-scores) to reduce the effect of both outliers and differences in units. Samples with missing or incomplete environmental data were excluded from the analyses.

Huse SM, Welch DM, Morrison HG, Sogin ML (2010) Ironing out the wrinkles in the rare biosphere through improved OTU clustering. Environmental Microbiology 12:1889–1898

Kozich JJ, Westcott SL, Baxter NT, Highlander SK, Schloss PD (2013) Development of a Dual-Index Sequencing Strategy and Curation Pipeline for Analyzing Amplicon Sequence Data on the MiSeq Illumina Sequencing Platform. Appl Environ Microbiol 79:5112–5120

Quast C, Pruesse E, Yilmaz P, Gerken J, Schweer T, Yarza P, Peplies J, Glockner FO (2013) The SILVA ribosomal RNA gene database project: improved data processing and web-based tools. Nucleic Acids Research 41:D590–D596

Rognes T, Flouri T, Nichols B, Quince C, Mahé F (2016) VSEARCH: a versatile open source tool for metagenomics. PeerJ 4:e2584

Schloss PD, Westcott SL (2011) Assessing and Improving Methods Used in Operational Taxonomic Unit-Based Approaches for 16S rRNA Gene Sequence Analysis. Appl Environ Microbiol 77:3219–3226

Schloss PD, Westcott SL, Ryabin T, Hall JR, Hartmann M, Hollister EB, Lesniewski RA, Oakley BB, Parks DH, Robinson CJ, Sahl JW, Stres B, Thallinger GG, Horn DJV, Weber CF (2009) Introducing mothur: Open-Source, Platform-Independent, Community-Supported Software for Describing and Comparing Microbial Communities. Appl Environ Microbiol 75:7537–7541

Wang Q, Garrity GM, Tiedje JM, Cole JR (2007) Naïve Bayesian Classifier for Rapid Assignment of rRNA Sequences into the New Bacterial Taxonomy. Appl Environ Microbiol 73:5261–5267